



Report SPR-P1(15) M027

Final Report
26-1121-4025-001

Performance Assessment of Deteriorated and Retrofitted Steel HP Piles

Joshua Steelman, Ph.D.

Assistant Professor
Department of Civil Engineering
University of Nebraska-Lincoln

Steven Stauffer

Graduate Research Assistant
Department of Civil Engineering
University of Nebraska-Lincoln

2016

Nebraska Transportation Center
262 WHIT
2200 Vine Street
Lincoln, NE 68583-0851
(402) 472-1975

"This report was funded in part through grant[s] from the Federal Highway Administration [and Federal Transit Administration], U.S. Department of Transportation. The views and opinions of the authors [or agency] expressed herein do not necessarily state or reflect those of the U.S. Department of Transportation."

Performance Assessment of Deteriorated and Retrofitted Steel HP Piles

Joshua Steelman, Ph.D.
Assistant Professor
Department of Civil Engineering
University of Nebraska-Lincoln

Steven Stauffer
Graduate Research Assistant
Department of Civil Engineering
University of Nebraska-Lincoln

A Report on Research Sponsored by

Mid-American Transportation Center

University of Nebraska-Lincoln

June 2016

Technical Report Documentation Page

1. Report No SPR-P1 (15) M027	2. Government Accession No.	3. Recipient's Catalog No.	
4. Title and Subtitle Performance Assessment of Deteriorated and Retrofitted Steel HP Piles		5. Report Date June 2016	
		6. Performing Organization Code 26-1121-4025-001	
7. Authors Joshua Steelman, Steven Stauffer		8. Performing Organization Report No.	
9. Performing Organization Name and Address University of Nebraska-Lincoln Nebraska Transportation Center 2200 Vine St. 262 Whittier Research Center PO Box 830851 Lincoln, NE 68583-0851		10. Work Unit No. (TRAIS)	
		11. Contract or Grant No.	
12. Sponsoring Organization Name and Address Nebraska Department of Roads 1500 Hwy. 2 Lincoln, NE 68502		13. Type of Report and Period Covered July 2014-December 2015	
		14. Sponsoring Agency Code MATC TRB RiP No. 36240	
15. Supplementary Notes			
16. Abstract Steel piles are known to deteriorate at high rates in Nebraska, partially as a result of exposure to weathering, and partially due to corrosive soils. The Nebraska Department of Roads employs a reinforced concrete jacket to slow the progression of corrosion and also to restore capacity to deteriorated piles. The intent of this study was to assess the effectiveness of typical reinforced concrete encasement retrofits. The research included a literature review to collect information for current retrofit practices and research similar in nature to this study, followed by a series of experiments. The findings of the literature review showed that prescriptive concrete jackets were common, but fiber reinforced polymer wraps are gaining popularity. Analytical and experimental support for pile retrofits is limited, and recent research is focused on FRP applications, leaving a gap in knowledge for the expected performance of traditional concrete jackets. For the experiments described in this report, two pile scenarios were represented: abutments and pile bents. For each type there was a non-deteriorated, deteriorated, and retrofitted specimen. The capacity of each pile was assessed by applying axial and flexure-inducing shear loads. Deteriorated and retrofitted cases simulated corrosion loss by milling the flanges and cutting out portions of the web. The retrofitted case utilized a reinforced concrete encasement consistent with reference drawings provided by NDOR. The key findings of this study were that the standard retrofit is sufficient and likely more robust than necessary, concomitant with a greater than anticipated jacket-to-pile bond strength developed at the retrofitted section. Further investigation is recommended to determine the bond characteristics of steel fully encased by concrete, and whether simplifications to the typical detail can reliably provide capacity restoration.			
17. Key Words Steel pile, deterioration, retrofit, maintenance, structural testing		18. Distribution Statement	
19. Security Classification (of this report) Unclassified	20. Security Classification (of this page) Unclassified	21. No. Of Pages 88	22. Price

Form DOT F 1700.7 (8-72) Reproduction of form and completed page is authorized

Table of Contents

Disclaimer	viii
Abstract	ix
Chapter 1 Introduction	1
Chapter 2 Literature Review	3
2.1 DOT Retrofit Procedures	3
2.1.1 General Retrofit Procedures	3
2.1.2 Steel Channels	3
2.1.3 Steel Plates	4
2.1.4 Concrete Encasement	4
2.1.5 Fiberglass Jacket	5
2.2 Proprietary Products.....	7
2.2.1 Fabric Jacket	7
2.2.2 Custom Steel and Concrete Retrofit.....	8
2.3 Retrofit Practice Summary.....	9
2.4 Previous Research.....	9
2.4.1 Rehabilitation of Steel Bridge Columns with FRP Composite Materials.....	9
2.4.2 FRP Composites for Rehabilitation of Hydraulic Structures.....	12
2.4.3 Numerical Investigation of H-Shaped Short Steel Piles with Localized Severe Corrosion.....	13
2.5 Literature Review Summary	14
Chapter 3 Experimental Design	15
3.1 Test Specimens	15
3.1.1 Non-Deteriorated Case.....	16
3.1.2 Deteriorated Case.....	17
3.1.3 Retrofitted Case.....	20
3.2 Loading Protocol.....	21
3.2.1 Interaction Diagrams.....	22
3.2.2 Retrofit Capacity	27
3.3 Potential Retrofit Failure Cases	31
3.4 Setup	33
3.5 Data Acquisition	35
3.6 Procedure	40
Chapter 4 Data Processing	42
Chapter 5 Experimental Results.....	47
5.1 Material Testing.....	47
5.2 Abutment Case: Non-Deteriorated	50
5.3 Abutment Case: Deteriorated.....	55
5.4 Abutment Case: Retrofitted	59
5.5 Abutment Case: Overview	64
5.6 Pile Bent Case: Non-Deteriorated.....	65
5.7 Pile Bent Case: Deteriorated.....	70
5.8 Pile Bent Case: Retrofitted.....	75
5.9 Pile Bent Case: Overview	79
Chapter 6 Discussion and Conclusion	81

References.....	83
Appendix A.....	85

List of Figures

Figure 2.1 Steel channel retrofit details (GDOT, 2012)	4
Figure 2.2 Repair before and after pictures (GDOT, 2012).....	5
Figure 2.3 Formed fiberglass jacket (Wan, 2013)	6
Figure 2.4 Wrapped fiberglass jacket (QuakeWrap Australia, 2016).....	7
Figure 2.5 Hydro-Brace installation process	8
Figure 2.6 Test specimen configurations (Liu, 2003).....	10
Figure 2.7 Stiffness distribution and deflection shape (Liu, 2003).....	11
Figure 2.8 Deterioration on bridge substructure (Vijay et al. 2014).....	12
Figure 2.9 Before and after indicating load rating change (Vijay et al. 2014)	13
Figure 3.1 Simplified bridge elevation view.....	16
Figure 3.2 Non-deteriorated test cases.....	17
Figure 3.3 Deteriorated section milling detail	19
Figure 3.4 Deteriorated test cases	20
Figure 3.5 Elevation view of retrofitted test case milling.....	21
Figure 3.6 Retrofitted test cases.....	21
Figure 3.7 Abutment interaction diagram.....	25
Figure 3.8 Pile bent interaction diagram.....	26
Figure 3.9 Ultimate pile loading stress distribution.....	27
Figure 3.10 Failure case 1	32
Figure 3.11 Failure case 2.....	33
Figure 3.12 Failure case 3.....	33
Figure 3.13 AutoCAD drawing of test setup	35
Figure 3.14 Elevation view of strain gage locations.....	36
Figure 3.15 Cross section view of strain gage locations.....	36
Figure 3.16 Pressure cell locations	40
Figure 4.1 Partitioned cross-section for fiber analysis.....	44
Figure 4.2 Strain to stress conversion with yielding.....	44
Figure 4.3 Components of fiber forces: stress and area at each fiber	45
Figure 4.4 Deteriorated section elements for analysis	46
Figure 4.5 Moment arm distances for deteriorated section elements	46
Figure 5.1 56 ksi stress vs. strain	48
Figure 5.2 55 ksi stress vs. strain	49
Figure 5.3 Concrete strength vs. days.....	50
Figure 5.4 Non-deteriorated abutment test	51
Figure 5.5 Buckling of base section top flange.....	51
Figure 5.6 Non-deteriorated abutment case axial vs. moment.....	52
Figure 5.7 Non-deteriorated abutment shear vs. displacement.....	52
Figure 5.8 Non-deteriorated abutment base section strain vs. sample.....	54
Figure 5.9 Non-deteriorated abutment deteriorated section strain vs. sample.....	54
Figure 5.10 Deteriorated abutment test.....	55
Figure 5.11 Deteriorated abutment test: deteriorated section before and after.....	56
Figure 5.12 Deteriorated abutment shear failure at the deteriorated section	56
Figure 5.13 Deteriorated abutment deteriorated section strain vs. sample.....	57
Figure 5.14 Deteriorated abutment axial vs. moment.....	58

Figure 5.15 Deteriorated abutment shear vs. displacement	58
Figure 5.16 Deteriorated abutment base section strain vs. sample	59
Figure 5.17 Retrofitted abutment test	60
Figure 5.18 Retrofitted abutment base section failure	60
Figure 5.19 Retrofitted abutment axial vs. moment	61
Figure 5.20 Retrofitted abutment deteriorated section strain vs sample.....	62
Figure 5.21 Retrofitted abutment shear vs. displacement.....	63
Figure 5.22 Retrofitted abutment base section strain vs. sample.....	63
Figure 5.23 Abutment case base section axial vs. moment	64
Figure 5.24 Abutment case deteriorated section axial vs. moment	65
Figure 5.25 Non-deteriorated pile bent test	66
Figure 5.26 Non-deteriorated pile bent local buckling of base section	66
Figure 5.27 Non-deteriorated pile bent LTB failure	67
Figure 5.28 Non-deteriorated pile bent deteriorated section strain vs. sample.....	67
Figure 5.29 Non-deteriorated pile bent base section strain vs. sample.....	68
Figure 5.30 Non-deteriorated pile bent axial vs. moment	69
Figure 5.31 Non-deteriorated pile bent shear vs. displacement.....	70
Figure 5.32 Deteriorated pile bent test.....	71
Figure 5.33 Deteriorated pile bent deteriorated section global section failure	71
Figure 5.34 Deteriorated pile bent shear vs. displacement	72
Figure 5.35 Deteriorated pile bent base section strain vs. sample	73
Figure 5.36 Deteriorated pile bent axial vs. moment.....	73
Figure 5.37 Deteriorated pile bent deteriorated section strain vs. sample	74
Figure 5.38 Deteriorated pile bent deteriorated section strain vs. sample zoomed in	74
Figure 5.39 Retrofitted pile bent test	75
Figure 5.40 Retrofitted pile bent failure	76
Figure 5.41 Retrofitted pile bent axial vs. moment	77
Figure 5.42 Retrofitted pile bent deteriorated section strain vs. sample.....	77
Figure 5.43 Retrofitted pile bent shear vs. displacement.....	78
Figure 5.44 Retrofitted pile bent base section strain vs. sample.....	78
Figure 5.45 Pile bent case base section axial vs. moment	80
Figure 5.46 Pile bent case deteriorated section axial vs. moment	80
Figure A.1 Potential loading scenarios and ultimate combined load targets	87

List of Tables

Table 3.1 Deterioration analysis results.....	19
Table 3.2 Strain gage locations.....	37
Table 3.3 Additional strain gage locations	37
Table 3.4 Strain gage monikers	38
Table 3.5 String pot locations	39
Table 5.1 Steel yield strength results	48
Table 5.2 Concrete strength results.....	49
Table A.1 Nebraska bridge data summary (NBI, 2013).....	86

Disclaimer

The contents of this report reflect the views of the authors, who are responsible for the facts and the accuracy of the information presented herein. This document is disseminated under the sponsorship of the U.S. Department of Transportation's University Transportation Centers Program, in the interest of information exchange. The U.S. Government assumes no liability for the contents or use thereof.

Abstract

Steel piles are known to deteriorate at high rates in Nebraska, partially as a result of exposure to weathering and partially due to corrosive soils. The Nebraska Department of Roads (NDOR) employs a reinforced concrete jacket to slow the progression of corrosion and restore capacity to deteriorated piles. The intent of this study was to assess the effectiveness of typical reinforced concrete encasement retrofits. The research included a literature review to collect information about current retrofit practices and research similar in nature to this study, followed by a series of experiments. The findings of the literature review show that prescriptive concrete jackets are common, but fiber reinforced polymer wraps are gaining popularity. Analytical and experimental support for pile retrofits is limited and recent research is focused on FRP applications, leaving a gap in knowledge regarding the expected performance of traditional concrete jackets. Two pile scenarios are represented in the experiments described in this report: abutments and pile bents. For each type there was a non-deteriorated, deteriorated, and retrofitted specimen. The capacity of each pile was assessed by applying axial and flexure-inducing shear loads. The deteriorated and retrofitted cases simulated corrosion loss by milling the flanges and cutting out portions of the web. The retrofitted case utilized a reinforced concrete encasement consistent with reference drawings provided by NDOR. The key findings of this study are that the standard retrofit is sufficient and likely more robust than necessary, concomitant with a greater than anticipated jacket-to-pile bond strength developed at the retrofitted section. Further investigation is recommended to determine the bond characteristics of steel fully encased by concrete, and whether simplifications to the typical detail can reliably provide capacity restoration.

Chapter 1 Introduction

Hydric and saline soils in Nebraska contribute to corrosive deterioration of steel HP pile bridge foundations even when buried. At abutments, the piles are ostensibly protected from exposure by earth fill. However, standard details used in the past have permitted water and de-icing salt intrusion behind abutment backwalls, commonly resulting in a washout of soils surrounding steel piles near the bottom of abutment pile caps. The exposure of initially buried steel surfaces results in accelerated steel pile deterioration. Pile bents are constantly exposed, but typically painted to limit exposure and protect the steel from deterioration. As with the abutment soil, the paint on pile bents wears away over time, leaving the steel exposed to deleterious environmental influences.

When piles experience section loss, the bridge must either be evaluated and possibly posted to limit the permissible load allowed to pass over the bridge, or the piles must be retrofitted to slow the corrosion and/or to restore the capacity of the piles. Research to restore the capacity of piles often addressed post-seismic repairs rather than long-term corrosive deterioration, but the methods share similar objectives. The goal of this research project is to validate a commonly-employed method in Nebraska, with reference to other Department of Transportations' (DOTs') practices, if applicable.

Nebraska Department of Roads' current policy for repairing corroded steel HP piles is as follows:

1. Clean the corroded area by sandblasting the pile.
2. Place temporary forms and reinforcing steel.
3. With formwork and reinforcing steel in place, encase the pile in concrete from above the water line to below the mud line.

Extending the encasement above the water line and below the mud line further helps reduce corrosion. The concrete is reinforced with rebar to provide confinement and nominally develop some measure of composite action. A rebar cage is built to reinforce the boundary of the concrete, in addition to rebar doweled through the pile web. The rebar cage provides the benefits of confinement for axial load transfer in addition to acting as flexural reinforcement.

Chapter 2 Literature Review

This section provides an overview of the state-of-practice for repair techniques currently in use by DOTs, proprietary repair methods with developing technologies, and previous research related to steel pile retrofits. The merits of these repairs are considered with respect to their structural capacity restoration, ease of installation, and durability.

2.1 DOT Retrofit Procedures

The state Department of Transportation (DOT) repair procedures that will be addressed in the following sections were identified from DOT maintenance manuals and research. Repair procedures documented by Delaware Department of Transportation (DELDOT), Georgia Department of Transportation (GDOT), and Florida Department of Transportation (FDOT) will be described in addition to research funded by Iowa Department of Transportation (IADOT) and Wisconsin Department of Transportation (WisDOT). Many of the repair procedures follow a similar process, so in order to reduce redundancies, all details will be discussed in a comprehensive section for each repair type.

2.1.1 General Retrofit Procedures

All repair types require similar cleaning and preparation. Almost all procedures indicated that the pile must be sand blasted to near white steel. For both concrete encasement and FRP jackets, cover below the mud line and well above the high water line are required to reduce corrosion rates. Various specific forms of repairs are described in the following sections.

2.1.2 Steel Channels

IADOT (Wipf, 2003), GDOT (2012), and WisDOT (Wan, 2013) all describe a retrofit involving steel channels bolted to the exterior of the flange across the damaged area of the pile, as shown in figure 2.1 This retrofit's installation would require minimal effort and the design

capacity could be determined using current steel design techniques. Although installation of this retrofit is simple, the retrofit itself is expected to degrade similarly to the original structure.

GDOT also permits a welded alternative to the bolted channels.

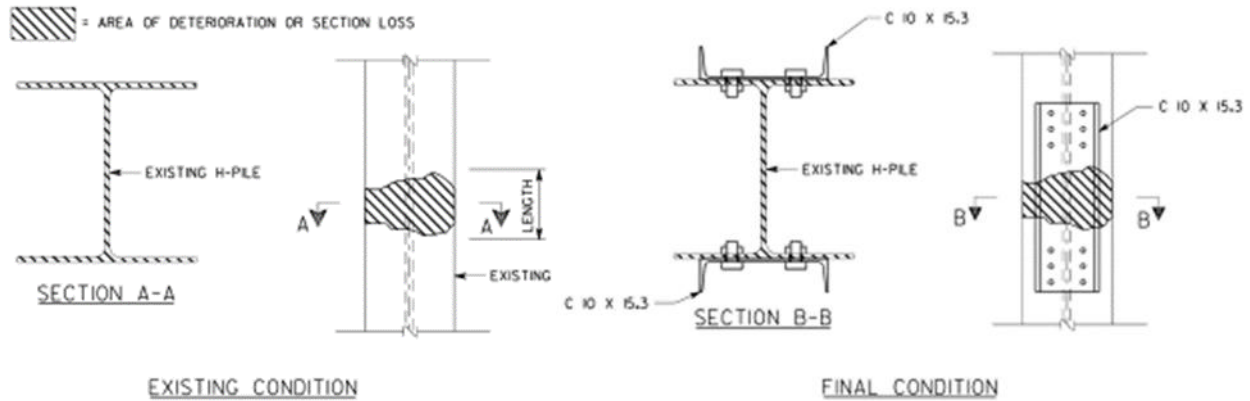


Figure 2.1 Steel channel retrofit details (GDOT, 2012)

2.1.3 Steel Plates

The use of welded steel plates is a method that was only found in the United States Department of the Army (1991) repair procedure manual. This repair type is similar to the channel repair method and would have similar benefits and disadvantages. Without the buckling resistance of the channels' flanges, as in the previous retrofit, the stability of the entire cross section at the deteriorated location may be compromised if the web is too significantly deteriorated to provide buckling restraint to the flanges and plates.

2.1.4 Concrete Encasement

DELDOT (2012), FDOT (2011), GDOT (2012), and WisDOT (Wan, 2013) each prescribe a type of concrete encasement procedure. Each procedure requires reinforcement in the concrete, although the requirement is nominal and prescriptive. The reinforcing provides

confinement to the concrete, as well as flexural strength. Georgia describes both a circular (see fig. 2.2) and square concrete encasement case. Florida does not prescribe a shape. Research performed for Wisconsin (Wan, 2013) used a square encasement detail similar to that used by Ohio DOT. The use of concrete provides the benefit of continuous bracing along the deteriorated section. Unfortunately, the concrete also prevents observation of the steel after the repair is made. FDOT discourages the use of jackets because it is difficult or impossible to monitor the condition of the steel after the jacket is installed.



Figure 2.2 Repair before and after pictures (GDOT, 2012)

2.1.5 Fiberglass Jacket

The newest type of steel pile repair documented in the literature employs fiber-reinforced polymer (FRP). A fiberglass jacket replaces the reinforcing steel used in the concrete encasement repair to provide confinement in compression and tension resistance in flexure. The FRP acts as both a stay-in-place form for the concrete and reinforcement after the concrete has cured. Three DOTs, DELDOT (2012), FDOT (2011), and WisDOT (Wan, 2013), mention this method in their

manuals, but offer little guidance because the material is relatively novel for civil engineering applications. This technique is similar to those previously mentioned in terms of preparation and placement. Figure 2.3 and figure 2.4 show the two common types of FRP wraps available: formed and wrapped.

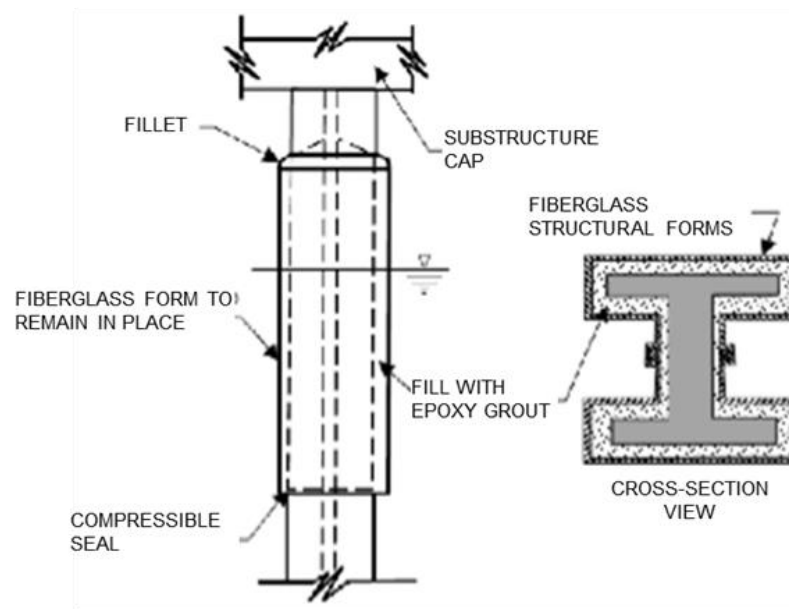


Figure 2.3 Formed fiberglass jacket (Wan, 2013)



Figure 2.4 Wrapped fiberglass jacket (QuakeWrap Australia, 2016)

2.2 Proprietary Products

In addition to current DOT procedures, proprietary methods are also available. Similar to the previously described DOT methods, these remediation approaches are similar in nature and can be categorized.

2.2.1 Fabric Jacket

An alternative jacketing method uses a fabric wrap to enclose the concrete at the deteriorated location. An example of this type of retrofit was observed by the authors during a site visit organized by NDOR to observe a demonstration of an FRP wrap. It was unclear whether the jacket incorporated steel reinforcing, but images available on a manufacturer's website (Construction Techniques, Inc., 2014) suggest that internal steel reinforcing may have been installed. Little information is available for the use and effectiveness of this method in

Nebraska. If reinforcements are not installed in the concrete then the product must rely heavily on the zipper and zipper/fabric connection, which would introduce an unconventional limit state for consideration and potentially result in premature failure. It is unlikely that a fabric enclosure is the most efficient and reliable method available to remedy pile deterioration.

2.2.2 Custom Steel and Concrete Retrofit

Custom retrofits are available to fit with tight dimensional tolerances against deteriorated sections when complications such as secondary member connections make other methods excessively complex or costly. The Hydro-Brace (Castle Group, 2014), for example, is configured into a C shape and fabricated to fit against the web of an I-shape in the space between the flanges. Fabrication costs will be higher for this method compared to simpler methods, such as typical concrete jackets, except for situations like those shown in figure 2.5, which would require forms to accommodate diagonal lateral bracing members.



Figure 2.5 Hydro-Brace installation process

2.3 Retrofit Practice Summary

Common retrofit methods identified in the literature primarily appear to have been developed in-house and designed for the convenience of state repair crews. The materials are commonly available and typically incorporated into bridge designs. This provides DOTs with an easy means of performing repairs, but practice appears to be strongly prescriptive rather than analytical. Consequently, installed retrofits are generally unverified and carry unknown capacities and limitations.

2.4 Previous Research

This section describes the sparse research focused on the corrosion and repair of steel piles available at this time.

2.4.1 Rehabilitation of Steel Bridge Columns with FRP Composite Materials

Liu (2003) researched the benefit of FRP (Fiber Reinforced Polymer) wraps on piles with simulated corrosion. Axial testing was performed at the University of Missouri-Rolla to determine the capacity of the piles with varying wrap lengths and concrete fills. Sketches of the test specimens are shown in figure 2.6. Axial loading tests demonstrated that increasing wrap lengths correlated to increased benefits to strength. Even when the wrap covered only the deteriorated region without lapping sound material, the capacity was almost fully restored. The type of concrete used also played a role in the pile strength. The test results indicated that retrofitted pile strength increased with wrap length and the strength increase was compounded using expansive concrete.

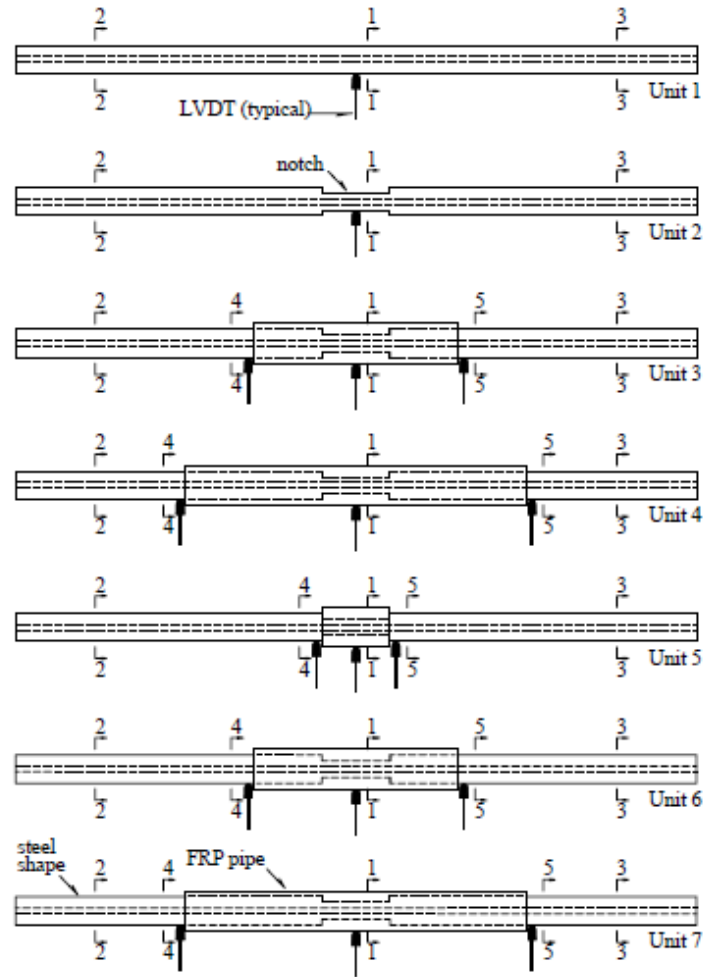


Figure 2.6 Test specimen configurations (Liu, 2003)

Strength increases correlate with longer wrapped lengths because the wrapped cross section provides improved buckling resistance with the greater effective moment of inertia affording greater stability. The expansive concrete provides improved effectiveness of transformed section properties with improved composite action between the FRP, concrete, and steel. The findings of this research substantiate the practice of extending the retrofit repairs from above the waterline to below the mud line to provide improved stability near the deteriorated section.

An analytical model was developed using the energy method in order to calculate the pile strength. By setting the strain energy equal to the work done, the researchers were able to develop the buckling load equation representing the column strength of a compression element, as shown in figure 2.7.

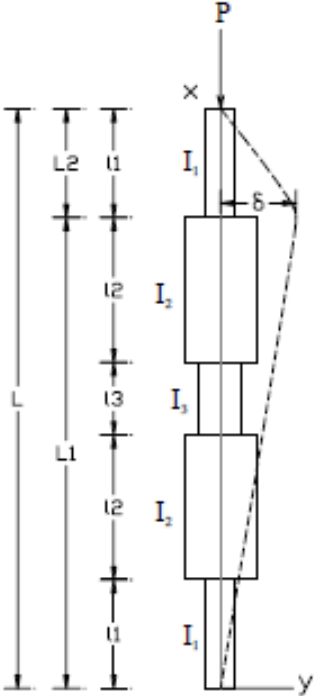


Figure 2.7 Stiffness distribution and deflection shape (Liu, 2003)

2.4.2 FRP Composites for Rehabilitation of Hydraulic Structures

In an effort to reduce the cost of repairs, the United States Army Corps of Engineers requested research on the use of FRP material for various hydraulic structures (Vijay, Clarkson, GangaRao, Soti, & Lampo, 2014). One of these applications was a bridge with a steel substructure. The structure included a pile bent with all piles located in a waterway. The piles experienced significant section loss up to 6 feet high (see fig. 2.8). The piles were wrapped with a full height FRP shell and filled first with epoxy grout for a depth of 9 inches, then with self-consolidating concrete for the remainder of the wrap height. The FRP shell was also wrapped with two layers of GFRP (glass FRP) prior to filling. The research project is ongoing, but thus far the repairs have shown a cost savings of 35% and a favorably short construction time. Prior to repairs the bridge had been reduced to a single lane, 6 ton limit, but after repairs the bridge was opened to two lanes and a 15 ton limit (see fig 2.9).



Figure 2.8 Deterioration on bridge substructure (Vijay et al. 2014)



Figure 2.9 Before and after indicating load rating change (Vijay et al. 2014)

2.4.3 Numerical Investigation of H-Shaped Short Steel Piles with Localized Severe Corrosion

TXDOT and the University of Houston partnered to conduct research investigating corrosion effects on HP pile axial capacity (Shi, 2014). The research was an analytical parametric study with the baseline model validated against experiments on reduced scale specimens (W4x13 x 32 in. long). The experimental and analytical work focused on piles subjected to pure axial load. The analytical study varied the location, configuration, and severity of deterioration to evaluate sensitivities of axial capacity to the various parameters. The researchers identified damage regions, from minor to moderate to severe. The minor damage region is bounded by the limit at which the yield strength of the remaining pile has fallen to the original design load of the pile. Within this range, the pile only requires stiffening sufficient to

prevent local and global buckling in order for a remediation measure to be successful. Load sharing with the retrofit is not required in the minor damage region.

In addition to the damage classifications, it was determined that flange deterioration was the single factor that most significantly affected the remaining axial capacity of the pile. It was also established that the location of the deterioration along the pile did not have a significant effect on the axial capacity.

2.5 Literature Review Summary

Numerous repair procedures and proprietary products are available to aid in the rehabilitation of deteriorated steel piles. However, common procedures are prescriptive, and little experimental or analytical data is available to characterize restored capacities of deteriorated steel piles. The information gathered by the University of Houston provides useful insights for deteriorated pile rehabilitation, but research is lacking to demonstrate the effectiveness of these repair options at full scale.

Chapter 3 Experimental Design

The experimental testing for this project evaluated reinforced concrete encasement, which is the prevalent repair method employed by the Nebraska Department of Roads for deteriorated steel HP piles. The experiments demonstrated capacities for piles in three conditions: as-built (non-deteriorated), deteriorated without retrofit, and deteriorated with retrofit. Additionally, two pile locations were considered: abutment and pile bent. The experimental investigation was intended to not only validate the restoring capacity of the concrete encasement retrofit employed by NDOR, but to also provide additional information pertaining to failure mechanisms. The repair is applied with the purpose of protecting the remaining portions of the pile, slowing the rate of corrosion, and restoring some or all of the pile's capacity. The following subsections will discuss the theoretical capacities of each component of the retrofit and the loading rate that was used for the experimental investigation, followed by the design and layout of the experiments and the procedure used during the tests.

3.1 Test Specimens

For this project, HP 10x42 (AISC, 2010) steel piles were obtained with a minimum yield strength of 50 ksi. The HP 10x42 is a historically common pile size utilized by NDOR for steel piling. The piles of interest to this project are likely to have been in service for some time, and are more likely to be 36 ksi steel rather than the 50 ksi steel more commonly used and produced at present. Initial designs assumed 36 ksi steel, but the specimens procured for use in experiments were 50 ksi due to availability. The experimental investigation comprised six total piles: three abutment simulations and three pier simulations. Figure 3.1 shows a schematic of a bridge indicating scenarios where each simulation case applies.

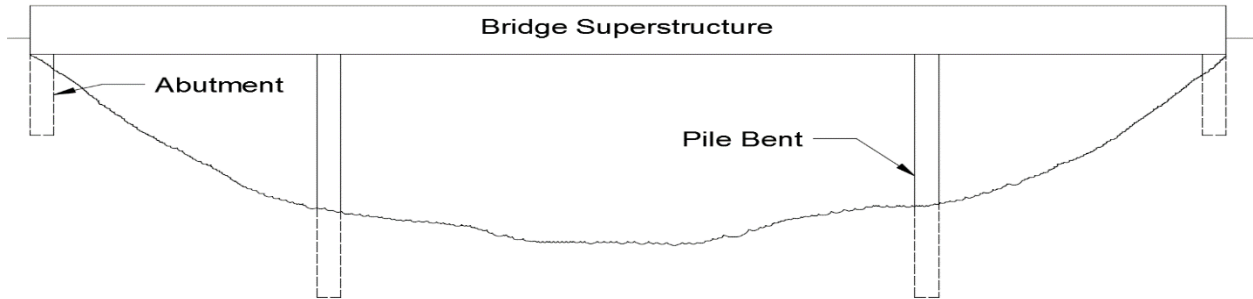


Figure 3.1 Simplified bridge elevation view

Simulated pile lengths and an assumed depth of fixity of 5 feet were established based on expert opinions supplied by the Technical Advisory Committee for the project at NDOR. The ground elevation was assumed to be at the bottom of the pile cap for the abutment case, and a 9 feet 6 inches clear height was assumed between the pile cap and ground for the pier case. Additional plate steel was added to each specimen to distribute end loads and to stiffen and stabilize the cross-section where concentrated transverse loads were applied. Additional modifications specific to individual tests are described in the following sections.

3.1.1 Non-Deteriorated Case

Non-deteriorated tests established a baseline for the ultimate load that an undamaged specimen could resist and provided a reference for a comparison of capacity, failure mechanisms, and instrumentation readings after deteriorated and retrofitted cases. No special modification were required for non-deteriorated cases other than those previously indicated. Schematic representations for the two cases are presented in figure 3.2

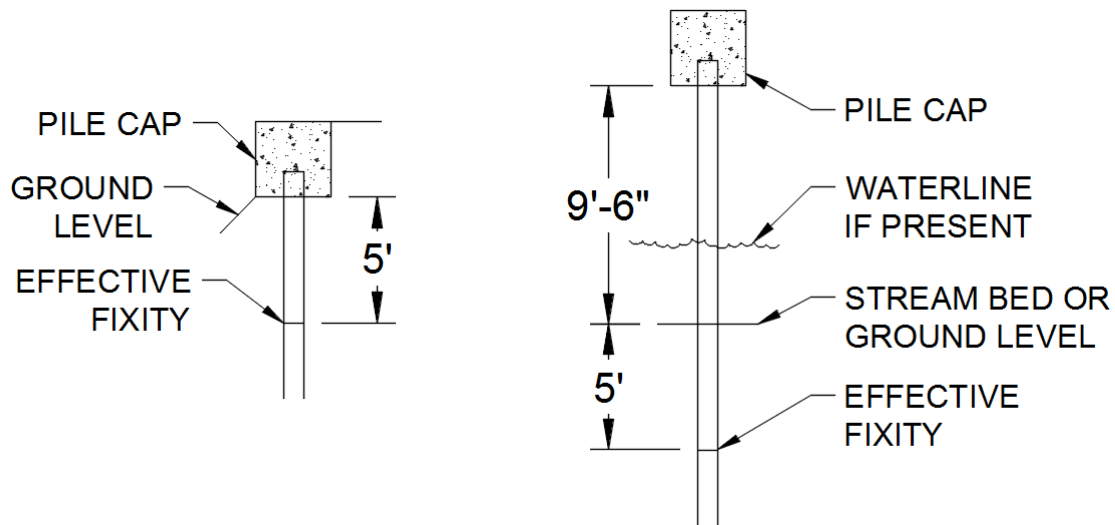


Figure 3.2 Non-deteriorated test cases

3.1.2 Deteriorated Case

The deterioration level (thickness reduction of flanges and web) selected for the experimental program was 45%. At a 45% reduction of the steel cross-section, the nominal yield strength of the remaining section was slightly (approximately 10 kips) less than the safe capacity of the test setup (350 kips). Bond was ignored for this estimation because it is implied to be negligible both by AASHTO (2012) and AISC (2010). Additionally, the yield strength of the pile specimens was assumed to be 50 ksi, but steel tensile coupon tests showed that this assumption underestimated the actual steel strength. Delayed delivery of the testing coupons led to this discovery after the milling had been completed and the concrete placed.

Corrosive section loss was simulated by milling flanges to reduce thickness. Although a uniform reduction in thickness would have been preferable, a compromise was designed such that holes cut through the web provided a reduced cross-section with a similar capacity to a uniform thickness loss. The theoretical strength of a uniformly deteriorated cross-section was calculated as a target capacity. Two separate analyses were conducted to determine and verify

the hole locations that would provide the target capacity by using cut-outs instead of uniform thickness reduction at the web. The demands for the analyses were based on the intersection of the axial-to-moment loading ratio and the combined axial-moment capacity interaction diagram of a cross section reduced by 45%. First, the reduced cross-section was evaluated assuming that moment induced by shear would form a couple acting on the outer portions (flanges, similar to WTs with holes cut in the section). The axial force was partitioned to the WT flanges and the rectangular bar (the remaining web between the holes) proportionately based on area. After preliminary design (placement of holes), a second corroborating analysis was performed utilizing SAP2000 software. The initial approximate analysis neglected flexural stiffness and frame action of the WT and rectangular bar components. In SAP2000, the structure was modeled to capture frame action by using beam elements with appropriate axial and flexural stiffness at the deteriorated section. The portion outside of the deteriorated section was modeled with rigid elements connecting the ends of the deteriorated segments, and axial and shear loads were applied to simulate test conditions. The bar dimension indicates the interior portion of the web that would remain, and the WT dimension is the portion of the web under the flange that would remain. The demand values in table 3.1 correspond to loading that would theoretically cause failure for a uniformly deteriorated section. From the two separate analyses, the remaining web portion should be approximately 2.65 inches and the stem of the flange should be 0.875 inches. The resulting cross section is shown in figure 3.3. As shown in figure 3.4, the deterioration was located based on field conditions inferred from previous repair scenarios. For the abutment case it was assumed that soil would erode, exposing the pile just below the pile cap, and that the most severe corrosion would occur 2 feet 3 inches below the bottom of the pile cap. A deteriorated location 3 feet 6 inches above ground level (or the stream bed) was assumed for the pile bent

experiments based on typical stream conditions in Nebraska and documentation for a previous repair project provided by NDOR. After the milling was completed, the deteriorated pile specimens were provided with identical plate steel at ends and transverse loading locations similar to the non-deteriorated specimens.

Table 3.1 Deterioration analysis results

			Excel Calculations	SAP2000		
Wt (Stem Height) in.	Bar (Width) in.	Capacity (k)	Demand (k)	Remaining (k)	Demand (k)	Remaining (k)
0.875		87.89	87.49	0.41	86.68	1.21
	2.65	45.77	30.32	15.45	30.59	15.18
1.25		102.06	91.99	10.07	91.76	10.30
	1.9	32.82	21.74	11.08	21.93	10.89
1.5		107.23	95.03	12.20	94.73	12.50
	1.4	24.18	16.02	8.16	16.16	8.02

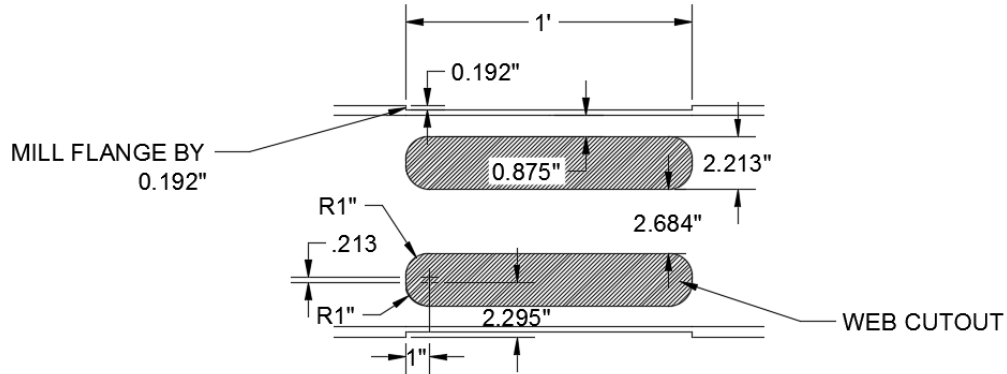


Figure 3.3 Deteriorated section milling detail

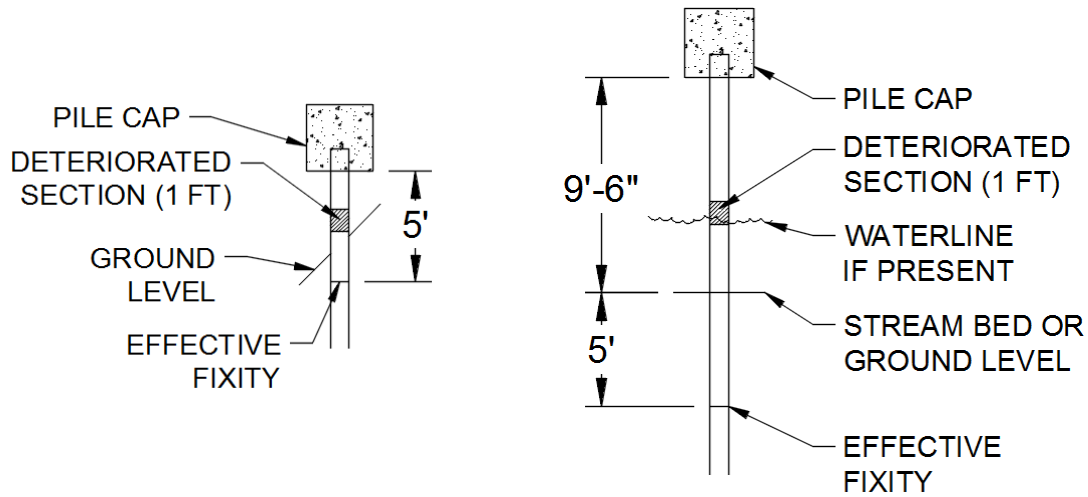


Figure 3.4 Deteriorated test cases

3.1.3 Retrofitted Case

Retrofitted specimens were milled and prepared with plate steel similarly to the deteriorated specimens prior to placing reinforced concrete consistent with NDOR's standard detail. Four 1 inch diameter holes (two on either side of the deteriorated section) were also cut through the web for doweled rebar, as shown in figure 3.5. The dowel holes were spaced at 12 inches on center, with the farthest dowels installed 18 inches from the boundary of the deteriorated section. Embedded instrumentation was installed with protective covering for both the strain gages and lead wires prior to placing concrete around the deteriorated steel section. Rebar was placed within the form to provide a cage, as illustrated in repair plans supplied by NDOR. Lastly, the concrete was placed and vibrated to consolidation, creating a test specimen that represented the two scenarios shown in figure 3.6 Instrumentation outside the concrete was similar to the previously described non-deteriorated and deteriorated cases, and installation was deferred until after the concrete had been placed while waiting for the concrete to cure.

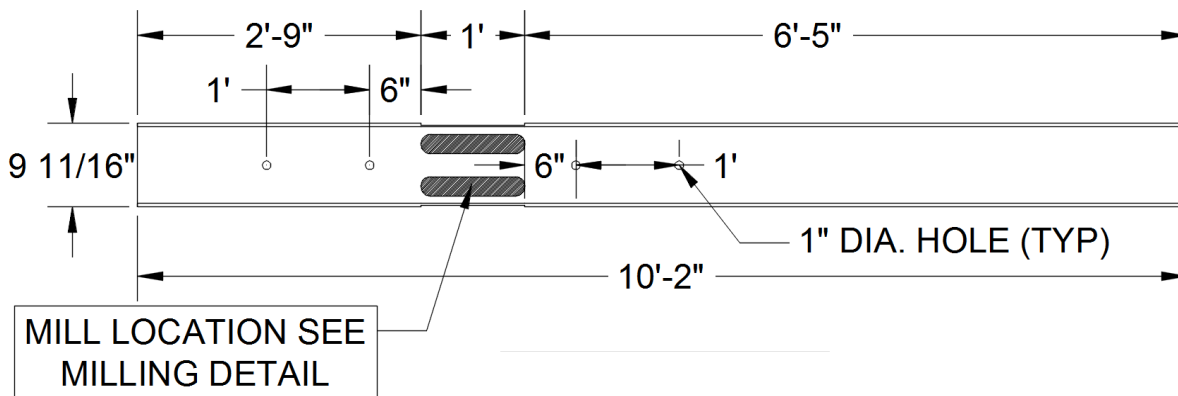


Figure 3.5 Elevation view of retrofitted test case milling

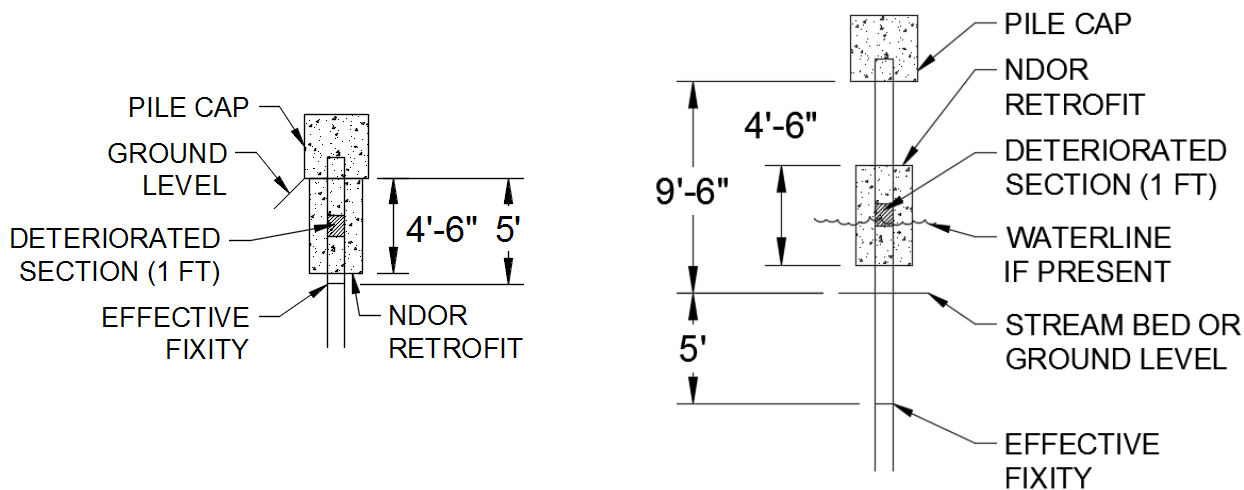


Figure 3.6 Retrofitted test cases

3.2 Loading Protocol

Prototype bridges and loading scenarios, considering sequences and combinations of vertical dead and live loads together with horizontal braking and thermal effects, were considered and presented to the Technical Advisory Committee. The Committee ultimately recommended an internal loading combination comprised of 80% axial and 20% moment. The authors interpreted this 80/20 loading ratio to correspond to a plastic condition, for which 80% of

the area resists axial load, and 10% at the outer edge of each flange resists flexure. Moment was induced for the experimental program by applying a shear load at the end of the specimens simulating braking or thermal effects from the pile cap. The following sections present and describe the equations used to calculate the capacity of steel structural elements subjected to combined axial and moment demand.

3.2.1 Interaction Diagrams

Equations from AISC (2010) and AASHTO (2012) were utilized to develop interaction diagram envelopes for combined loading capacity. A number of the equations were only available in AISC. The AASHTO (2012) equations were located by first consulting section 6.15 for piles and following references to the appropriate sections in 6.9 and 6.10. AASHTO equations (6.9.2.2-1) and (6.9.2.2-2) and AISC (H1-1a) and (H1-1b) are the typical approximate envelopes used by default, based on plastic capacity and validated by stub-column tests. AISC (H1-2) provides an alternative equation that is allowed to be used for out-of-plane buckling limit states, in conjunction with (H1-1) for in-plane buckling. AISC (C-H1-3a) and (C-H1-3b) provide analytical formulations for plastic combined loading capacity similar to, but more exact than, (H1-1).

Ch. H1.1(a)	$\frac{P_r}{P_c} + \frac{8}{9} \left(\frac{M_r}{M_c} \right) \leq 1.0$	(H1-1a) (AISC)
6.9.2.2		(6.9.2.2-2) (AASHTO)

Ch. H1.1(b)	$\frac{P_r}{2P_c} + \left(\frac{M_r}{M_c} \right) \leq 1.0$	(H1-1b)
6.9.2.2		(6.9.2.2-1)

Ch. H1.3	$\frac{P_r}{P_{cy}} \left(1.5 - .5 \frac{P_r}{P_{cy}} \right) + \left(\frac{M_{rx}}{C_b M_{cx}} \right)^2 \leq 1.0$	(H1-2)
No equivalent		

Comm. H1.1
$$\frac{M_{pc}}{M_p} = 1 - \frac{A^2 \left(\frac{P}{F_y}\right)^2}{4t_w Z_x} \quad (\text{C-H1-3a})$$

 No equivalent

Comm. H1.1
$$\frac{M_{pc}}{M_p} = \frac{A \left(1 - \frac{P}{F_y}\right)}{2Z_x} \left[d - \frac{A \left(1 - \frac{P}{F_y}\right)}{2b_f} \right] \quad (\text{C-H1-3b})$$

 No equivalent

Deteriorated sections were assumed to undergo uniform thickness loss at flanges and webs. The flange width was held constant. Corresponding P_c and M_c values were determined using the radius of gyration for a non-deteriorated section when evaluating Euler buckling stress, F_e , but reducing axial capacity with Q factors to address local instability associated with reduced flange and web thickness, according to the following equations.

Ch. E3, E7
 6.9.2.1
$$P_n = F_{cr} A_g \quad (\text{E3-1}), (\text{E7-1})$$

 (6.9.2.1-1)

Ch. E3(a)
 6.9.4.1.1
$$F_{cr} = \left[0.658 \frac{F_y}{F_e} \right] F_y \quad (\text{E3-2})$$

 (6.9.4.1.1-1)

Ch. E7(a)
 6.9.4.1.1
$$F_{cr} = Q \left[0.658 \frac{Q F_y}{F_e} \right] F_y \quad (\text{E7-2})^*$$

 (6.9.4.1.1-1)

*Where Q is a function of Q_a and Q_s .

Ch. E3(b), E7(b)
 6.9.4.1.1
$$F_{cr} = 0.877 F_e \quad (\text{E3-3}), (\text{E7-3})$$

 (6.9.4.1.1-2)

Sections F2 and F3 of AISC (2010) were used to determine pile flexural capacity. The AISC equations are functionally identical to AASHTO (2012) Chapter 6 when accounting for the web plastification factor, R_{pc} , which scales elastic to plastic capacity in Appendix A. The

presentation is significantly more simplified in AISC, which focuses on steel I-sections with compact webs and compact or noncompact flanges, such as the experimental test specimens, and characterizes bending capacity in terms of moment rather than stress.

$$\text{Ch. F2.1} \quad M_n = M_p = F_y Z_x \quad (\text{F2-1})$$

$$\text{Ch. F2.2(b)} \quad M_n = C_b \left[M_p - (M_p - 0.7F_y S_x) \left(\frac{L_b - L_p}{L_r - L_p} \right) \right] \leq M_p \quad (\text{F2-2})$$

$$\text{Ch. F3.2(a)} \quad M_n = M_p - (M_p - 0.7F_y S_x) \left(\frac{\lambda - \lambda_{pf}}{\lambda_{rf} - \lambda_{pf}} \right) \quad (\text{F3-1})$$

$$\text{Ch. F3.2(b)} \quad M_n = \frac{0.9E k_c S_x}{\lambda^2} \quad (\text{F3-1})$$

Figure 3.7 and figure 3.8 show the interaction diagrams for both pile types. The limits of the pile capacities were calculated based on equation H1-1 for strong and weak axis column buckling, as well as equation H1-2. For the deteriorated pile, equation H1-1 was utilized to predict the capacity against strong axis column buckling. The line labeled “Plastic: 80% P, 20% M” represents the loading ratio at the critical section (the depth of fixity) for the non-deteriorated pile. The line labeled “Loading at Deteriorated Section” accounts for the reduced moment arm to the deteriorated section relative to the depth of fixity, and the corresponding reduction in moment relative to axial load. The non-deteriorated loading ratio is based on the calculations preceding figure 3.9. The rectangular retrofit envelope is described in a subsequent section.

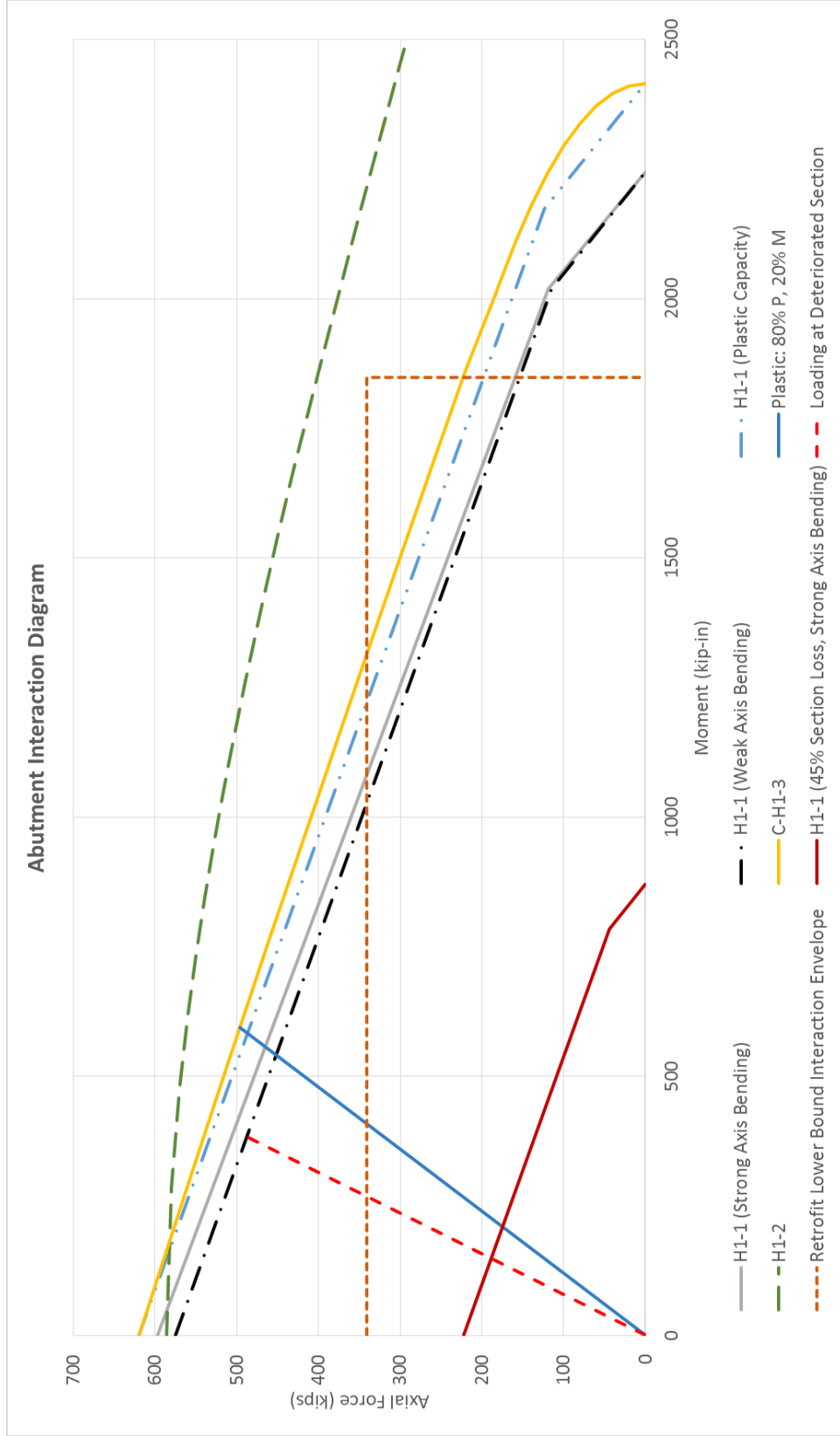


Figure 3.7 Abutment interaction diagram

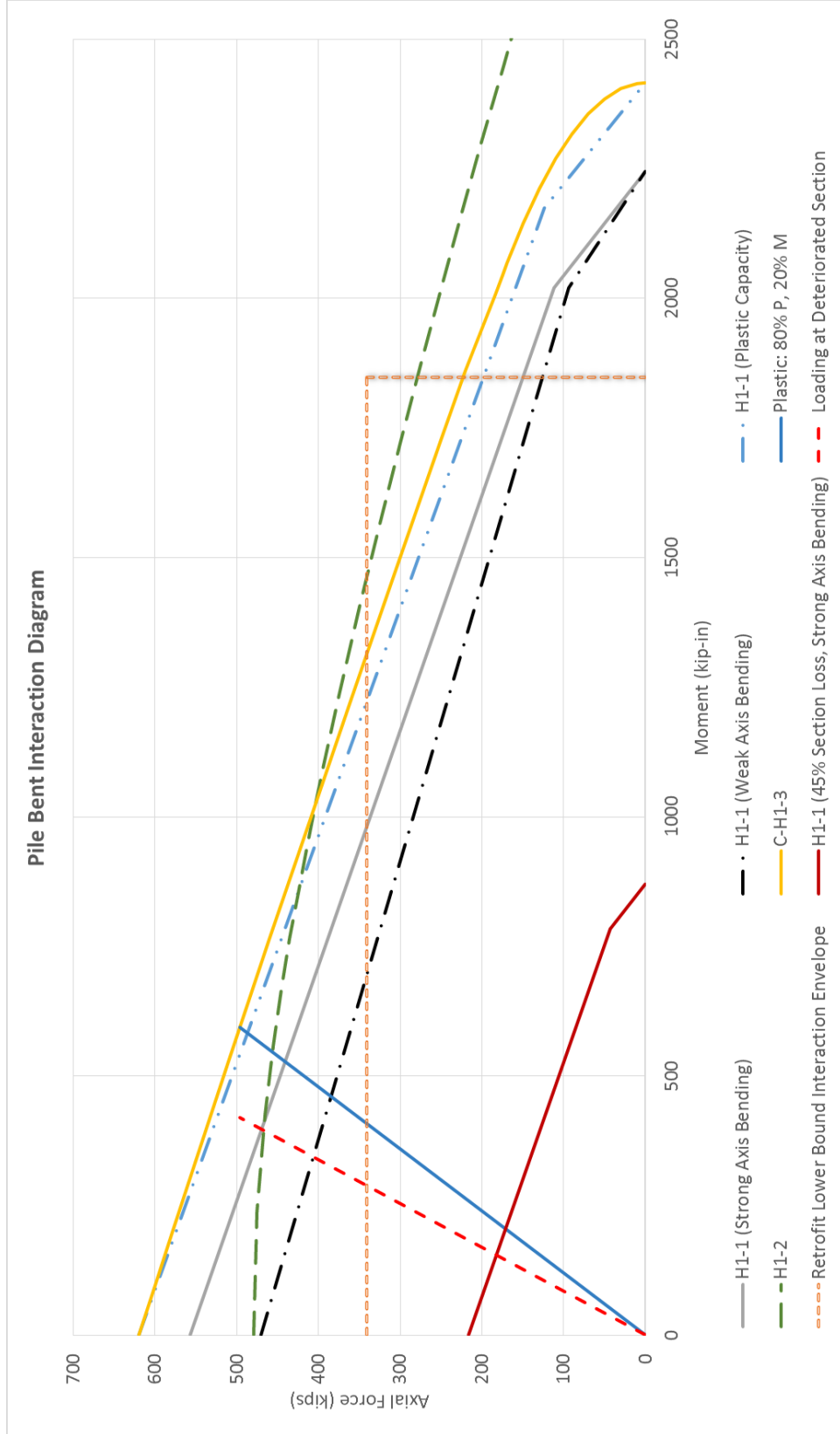


Figure 3.8 Pile bent interaction diagram

The slope of the loading ratio line in the preceding figures conforms to the 80/20 axial-moment ratio previously mentioned, as recommended by the project TAC. Reference values at the plastic capacity envelope were determined as follows:

$$\text{Depth of flange utilized for moment} = A_g * 20\% = 2.48 \text{ in}^2 \rightarrow \frac{2.48}{10.1 * 2} = .1228 \text{ in} = w$$

$$x = \text{Moment arm} = D - w = 9.7 - .1228 = 9.5772 \text{ in}$$

$$M = x * F_y * A_{\text{flange utilized for moment}} = 9.5772 * 50 * (.1228 * 10.1) = 593.9 \text{ k} - \text{in}$$

$$P = (A_g - A_{\text{flange utilized for moment}} * 2) * F_y = (12.4 - (.1228 * 10.1 * 2)) * 50 = 496 \text{ k}$$

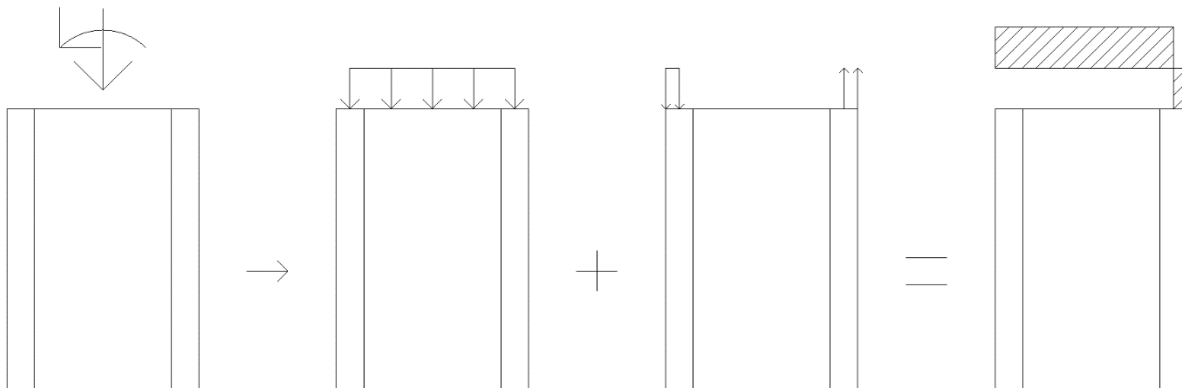


Figure 3.9 Ultimate pile loading stress distribution

3.2.2 Retrofit Capacity

The retrofit interaction envelope represents a conservative assessment that neglects composite action (i.e., assuming complete bond failure), with axial compression and bending moment capacities each limited solely by the separate capacities of the steel and the concrete jacket, respectively. Assuming negligible bond, the deteriorated section is expected to experience compression failure under combined axial and flexure demands. The jacket will restrain the

excessive rotation that would otherwise occur in its absence, resulting from the local compression failure at the deteriorated section. Even without bond, an embedded element can develop flexural restraint, similar to utility poles and signs. This assumption is implicit in typical pile cap designs. The Multidisciplinary Center for Earthquake Engineering Research (MCEER, 2011) tested embedment depth for pile-to-cap connections and developed an equation to calculate the embedment depth needed to fully transfer the shear and moment from the steel to the concrete. The application of this equation initially resulted in an embedment depth of 30.4 inches, which is just over half the length of the retrofit jacket in these experiments.

$$l_{emb} = 3.4 * d_p * \sqrt{\left(\frac{f_y}{0.85 * f'_c}\right) \left(\frac{t_f}{d_p}\right)} = 3.4 * 9.7 * \sqrt{\left(\frac{50}{0.85 * 3}\right) \left(\frac{0.42}{9.7}\right)} = 30.4 \text{ in.}$$

With the increase in provided material strength of both the steel and concrete, the depth was reduced to 21.8 inches. These calculations indicate that the standard detail can be reasonably expected to develop the full moment capacity of the pile. The steel axial capacity was taken as the maximum axial capacity of the deteriorated section with a 45% section loss. It was also assumed that the concrete jacket would provide sufficient confinement to eliminate local buckling, enabling the deteriorated section to reach its plastic limit in pure compression. Based on these assumptions, the minimum axial compression capacity for the retrofitted section was determined to be:

$$P_n = f_y * A_s = 50 \text{ ksi} * 0.55 * 12.4 \text{ in}^2 = 341 \text{ kips}$$

The ultimate moment capacity of the concrete jacket was determined assuming four #5 bars on the tension side of the cage provide tension reinforcing at the ultimate strength state. The nominal reinforced flexural strength of the jacket exceeds the cracking strength by 4 k-ft.

Moment Capacity (ignoring compression steel)

$$a = \frac{A_s f_y}{0.85 f'_c b} = \frac{0.31 \text{ in}^2 * 4 \text{ bars} * 60 \text{ ksi}}{0.85 * 3 \text{ ksi} * 30 \text{ in}} = 0.97 \text{ in}$$

$$c = \frac{a}{\beta_1} = \frac{0.97 \text{ in}}{0.85} = 1.14 \text{ in}$$

$$\varepsilon_s = \frac{d - c}{c} * 0.003 = \frac{26 \text{ in} - 1.14 \text{ in}}{1.14 \text{ in}} * 0.003 = 0.065 > 0.00207 \text{ (Tension Controlled)}$$

$$\begin{aligned} M_n &= A_s f_y \left(d - \frac{a}{2} \right) = 0.31 \text{ in} * 4 \text{ bars} * 60 \text{ ksi} * \left(26 \text{ in} - \frac{0.97 \text{ in}}{2} \right) \\ &= 1898.3 \text{ k} - \text{in} = 158.2 \text{ k} - \text{ft} \end{aligned}$$

Cracking Moment

$$\begin{aligned} M_{cr} &= \frac{f_r I_g}{y_t} = \frac{7.5 * \sqrt{f'_c} * \frac{b^4}{12}}{y_t} = \frac{7.5 * \sqrt{3000} \text{ psi} * \frac{30^4}{12} \text{ in}^4}{15 \text{ in}} = 1848563.63 \text{ lb} - \text{in} \\ &= 1848.7 \text{ k} - \text{in} = 154 \text{ k} - \text{ft} \end{aligned}$$

In addition to the concrete jacket that is applied in the retrofit, rebar is doweled through the web of the pile to provide improved composite action. Based on the standard retrofit, there are five 30-inch long pieces of rebar that are doweled through the pile's web and spaced evenly along the length. Neglecting bond, excess compression demand beyond the plastic strength of the deteriorated steel pile section would need to transfer through the two bars above the

deterioration, travel through the concrete, then return to the steel pile below the deteriorated section through the two bars below the deterioration. Estimating the dowel transfer capacity from the shear strength of the rebar:

Shear Capacity

$$P_n = 0.6F_y A_w C_v = 0.6 * 60 \text{ ksi} * \left(\frac{\left(\frac{6}{8}\right)^2}{4} * \pi \right) \text{ in}^2 * 1 = 15.9 \text{ k}$$

$$\text{For 2 bars } P_{n\text{total}} = 63.6 \text{ k}$$

This force would result in local crushing of the concrete bearing against the rebar. Alternatively, the shear transfer capability based on the plastic flexural strength of the bar and a uniform steel-on-concrete bearing stress distribution along the length of the bar is:

Plastic Limit

$$M_p = F_y Z_x \quad Z = \frac{d^3}{6} = \frac{\left(\frac{6}{8}\right)^3}{6} = 0.0703 \text{ in}^3$$

$$M_p = 60 \text{ ksi} * 0.0703 \text{ in}^3 = 4.22 \text{ k-in} = 0.35 \text{ k-ft}$$

$$\text{Distributed load} = \frac{4.22 \text{ k-in}}{15 \text{ in} * \frac{15}{2} \text{ in}} = 0.038 \frac{\text{k}}{\text{in}}$$

$$\text{Rebar bearing stress} = \frac{0.038 \frac{\text{k}}{\text{in}}}{\frac{6}{8} \text{ in}} = 0.51 \text{ ksi}$$

$$\text{For 2 bars } P_{n\text{total}} = 2.3 \text{ k}$$

The experiment was calibrated so that axial capacity for the retrofitted specimens would fall below the test setup limit of 350 kips unless the rebar contributed more than about 10 kips of shear transfer to the concrete. The presumption of negligible bond strength followed reviews of AASHTO (2012) and AISC (2010) design guidelines. AASHTO (2012) only discusses composite column capacity assuming the presence of mechanical connectors. The commentary for AASHTO section 6.12.2.3.1 states that “no test data are available for the loss of bond in composite beam columns.” AISC (2010) indicates that, for filled members, the direct bond interaction can be taken as 0.06 ksi with a reduction factor of 0.45. The experimental specimens are encased, not filled, so AISC would not permit any consideration of bond for the specimens according to their specification. However, as a point of reference, a perimeter of 56.25 in² and a length of 1 foot 9 inches per side of the deteriorated section would have an estimated bond transfer capacity of approximately 71 kips (32 kips after the reduction by the ϕ factor).

Values calculated for the concrete flexural strength and the steel compressive strength are based on the specified strengths of the material. Variation of the actual from the specified material strengths is addressed in the discussion of experimental results.

3.3 Potential Retrofit Failure Cases

Three possible failure cases were anticipated for the retrofitted pile. The first two possible failure cases are the failure of the pile in the jacket due to either the axial load or the shear-induced moment. The third possible failure case occurs in the pile adjacent to but outside the jacket.

For the first considered failure case the governing mechanism is local buckling of the reduced section, which would cause the pile to settle due to the axial load. Localized crushing of the confining concrete within the jacket would be required for this failure to occur. This

mechanism implicitly presumes low bond between the steel and concrete. Figure 3.10 illustrates failure case 1. The second considered failure case arises from local buckling due to the shear-induced moment at the deteriorated section, as shown in figure 3.11. This mechanism corresponds to poor moment transfer between the steel and concrete. The final failure case considered, shown in figure 3.12, occurs when the jacket acts compositely with the pile preventing local buckling of the steel within the jacket and carrying the excess flexure demand, leading to local buckling and plastification of the non-deteriorated, noncomposite section outside of the jacket.

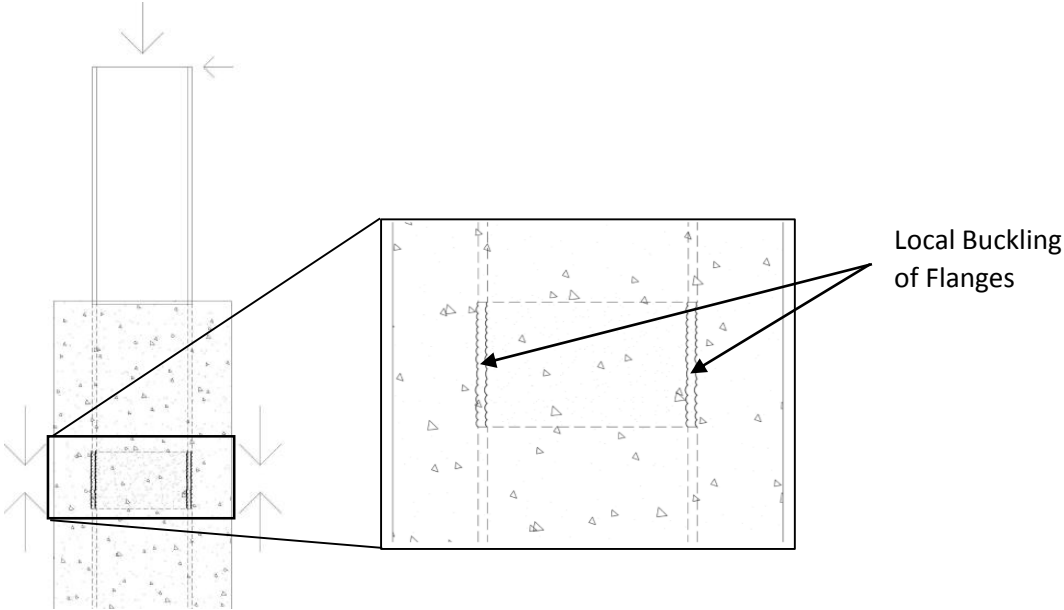


Figure 3.10 Failure case 1

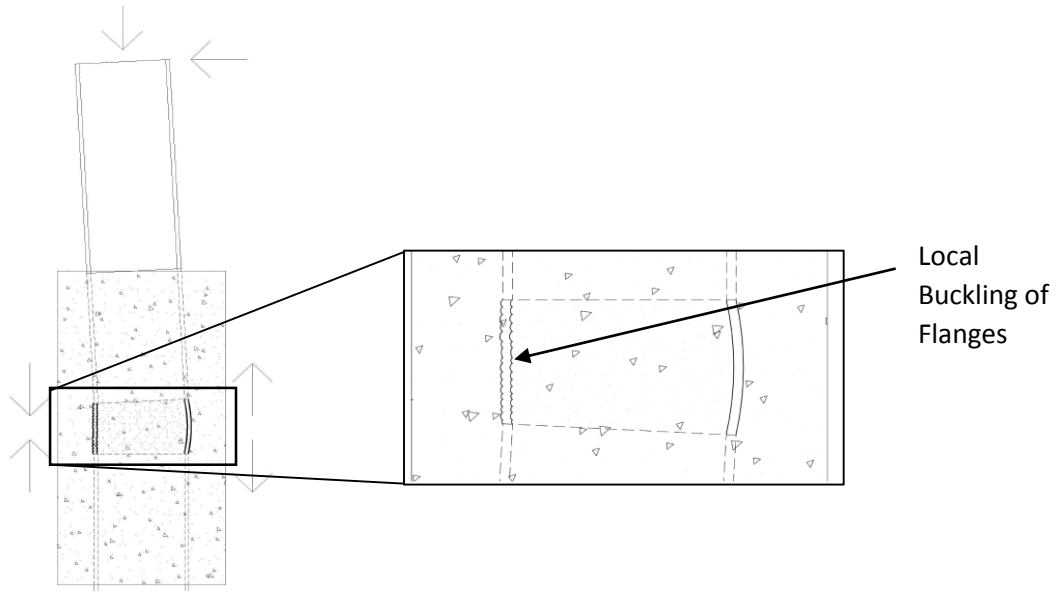


Figure 3.11 Failure case 2

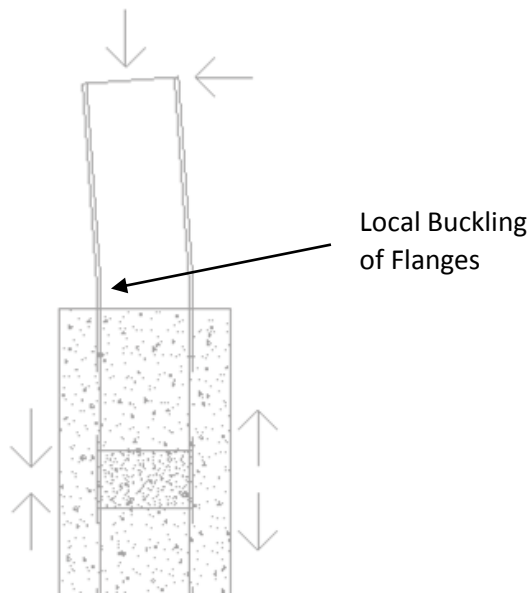


Figure 3.12 Failure case 3

3.4 Setup

The test setup was configured to apply both an axial and shear loads to induce combined axial and moment in the test specimens, simulating field loading conditions as indicated by the TAC. The axial and shear loads considered were both dead and live loads applied under

AASHTO (2012) design. The specific shear loads considered were the braking force and thermal effects transferred from the bridge deck down into the piles. Ultimately, the previously mentioned 80/20 loading ratio determined the applied loads, but this information was validated using data from the National Bridge Inventory (NBI, 2013). Span lengths and bridge width were determined via the Nebraska section of the NBI (2013) and used to estimate the maximum gravity-induced vertical loading for a typical pile. The loading ratio applied for the experiments is consistent with a loading condition for which this vertical compression load is coupled with the displacement caused by thermal expansion determined, as outlined in the NDOR Bridge Office Policies and Procedures (BOPP, 2014) manual.

The pile was placed horizontally with the flange face parallel to the floor as shown in figure 3.13. The specimen was placed on spacers, which rested on a steel-encased concrete block (referred to as the base block) that supported the pile's base, and tensioned to the strong floor with built-up spreader beams and Dywidag rods. A self-reacting frame was utilized to apply the axial load, and a single ram applied the shear load by reacting against the strong floor. The self-reacting frame consisted of four RCH-1506 hollow core rams, each acting on a 1¾ inch, cold-rolled, Dywidag all thread bar. The bar and ram reacted against custom built spreader beams, which consisted of two channels spaced and connected by 1-inch thick steel plates. The shear load was opposed by the two smaller spreader beams that were used to tension down the pile to form a couple and induce moment in the specimen.

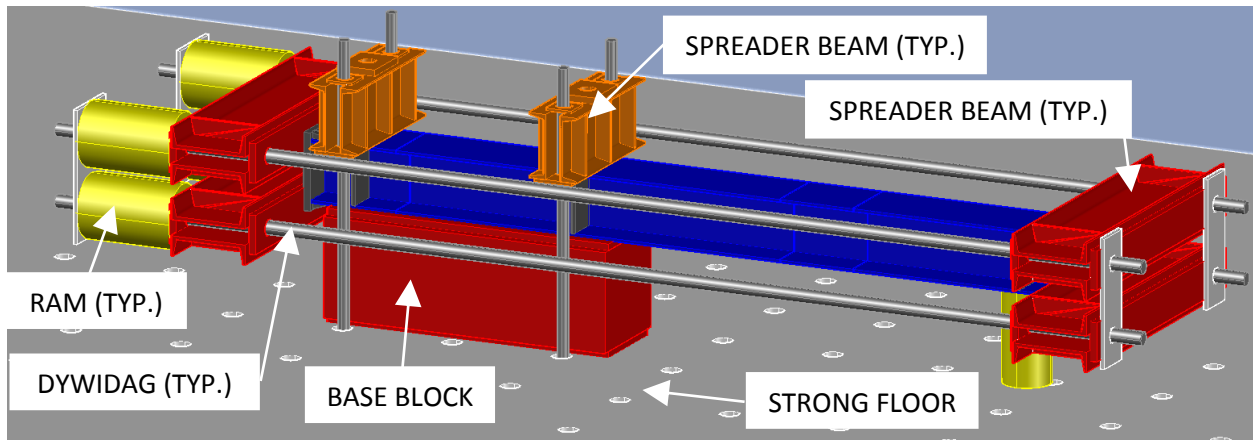


Figure 3.13 AutoCAD drawing of test setup

An analysis of the testing frame determined that the spreader beams were the limiting component of the setup. To ensure elasticity in the test frame, the axial force was limited to 350 kips. After following an 80/20 axial/moment ratio up to 350 kips of axial load, additional shear load was imposed to reach an ultimate limit.

3.5 Data Acquisition

During each test, data was collected for measured strains, displacements, and pressures. This data allowed for the axial and moment values to be calculated at key locations along the pile. The displacement data was collected through cable extension transducers (string pots) at four locations horizontally and vertically. Additionally, strain gages were located at the base and deteriorated sections, and additional gages were applied as needed for the retrofitted tests. Finally, pressure readings were taken from the hydraulic lines on the advance side of each ram.

For all of the tests strain gages were located at the base and deteriorated sections, as shown in figure 3.14. Both locations were instrumented with five gages, as illustrated in figure 3.15: one centered on the web and one centered in each half of the exterior flange face for both flanges.

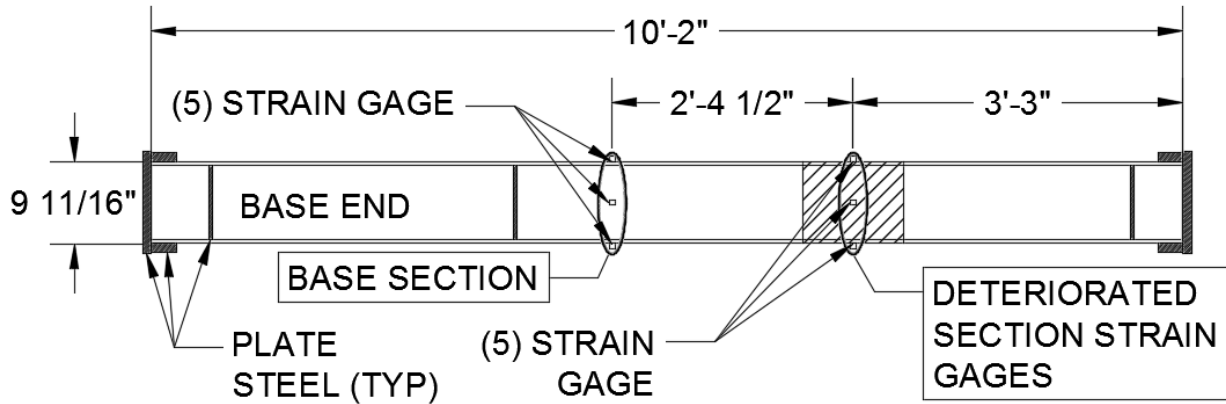


Figure 3.14 Elevation view of strain gage locations

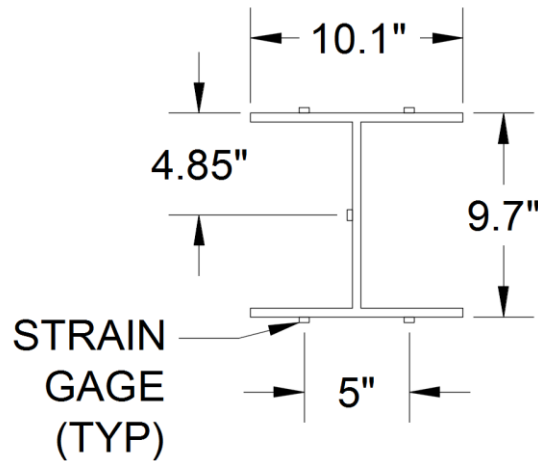


Figure 3.15 Cross section view of strain gage locations

All of the test specimens also included two gages located near the tie down location on the top flange that were installed similarly to the base and deteriorated section top flange strain gages. These two additional gages were used to indicate when the pile was beginning to yield. Additional strain gages were installed so the retrofitted cases could provide the piles' response in greater detail and allow for accurate load tracking and application. For the abutment case, additional gages were applied to the web at 1/4 and 3/4 of the section depth, d , to allow for

improved moment load monitoring during the test. Additional gages for the pile bent case were placed on either side of the retrofit (U and A locations, as defined in the following tables). This allowed for a comparison of the loading before and after the encasement.

The following tables provide the location of each strain gage. Table 3.2 shows the gage locations used in all of the tests, and table 3.3 shows the locations of the additional gages for the retrofitted tests. The location from the fixity point is given for the abutment case and pile bent case, respectively (only one number is given if it is the same for both cases). The calculations are based on the dimensions of the theoretical cross section and the placement of the gages was done with the precision of a tape measure.

Table 3.2 Strain gage locations

Gage Name	Location from Fixity Point	Distance from Center
BB-TF-L	4-3/8"	2.5"
BB-TF-R	4-3/8"	2.5"
B-TF-L	10-1/4"	2.5"
B-TF-R	10-1/4"	2.5"
B-W-R	10-1/4"	0"
B-BF-L	10-1/4"	2.5"
B-BF-R	10-1/4"	2.5"
D-TF-L	3' 2-3/4" / 8' 5-3/4"	2.5"
D-TF-R	3' 2-3/4" / 8' 5-3/4"	2.5"
D-W-R	3' 2-3/4" / 8' 5-3/4"	0"
D-BF-L	3' 2-3/4" / 8' 5-3/4"	2.5"
D-BF-R	3' 2-3/4" / 8' 5-3/4"	2.5"

Table 3.3 Additional strain gage locations

Gage Name	Location from Fixity Point	Distance from Center
B-W-R(A)	10-1/4" / N/A	1-7/8"
B-W-R(U)	10-1/4" / N/A	1-7/8"
U-TF-L	N/A / 5' 11-1/4"	2.5"
U-TF-R	N/A / 5' 11-1/4"	2.5"
U-W-R	N/A / 5' 11-1/4"	0"
U-BF-L	N/A / 5' 11-1/4"	2.5"
U-BF-R	N/A / 5' 11-1/4"	2.5"
A-TF-L	N/A / 11' 1/4"	2.5"
A-TF-R	N/A / 11' 1/4"	2.5"
A-W-R	N/A / 11' 1/4"	0"
A-BF-L	N/A / 11' 1/4"	2.5"
A-BF-R	N/A / 11' 1/4"	2.5"

The gages were given monikers to help with quick identification during and after the test. The format employed for the monikers was {location along the length} – {vertical placement} – {horizontal placement}. Table 3.4 presents the abbreviation, labels, and descriptions for the three

parts of the moniker. References to “before” and “after” the retrofit are based on a progression from the embedded end to the pile cap.

Table 3.4 Strain gage monikers

Location along the length		
BB	Base Block	Location closest to the fixity point
B	Base	Non-deteriorated section expected failure location
U	Under	Location before the retrofit (when applicable)
D	Deteriorated	Deteriorated section location
A	Above	Location after the retrofit (when applicable)
T	Top	Location of the pile top
Vertical Placement		
TF	Top Flange	Exterior face of the top flange
W	Web	Either face of the web
BF	Bottom Flange	Exterior face of the bottom flange
Horizontal Placement		
L	Left	Left of center looking from the base towards the top
C	Center	Center of the section
R	Right	Right of center looking from the base towards the top

The displacements were measured at the same descriptive locations (e.g., deteriorated or top) for the abutment and pile bent cases. Vertical displacements were measured relative to the strong floor at the tie down point, base section, deteriorated section, and top of the pile.

Horizontal displacements were measured from the base section, deteriorated section, and two from the top. The first horizontal top displacement was measured for out of plane movement, and the second for shortening of the pile along its length. Table 3.5 summarizes the locations displacement measurements were taken.

Table 3.5 String pot locations

Gage Name	Location from Fixity Point	Measured
BB-BF-C	4-3/8"	Vertical
B-BF-C	10-1/4"	Vertical
D-BF-C	3' 2-3/4" / 8' 5-3/4"	Vertical
T-BF-C	6' 5-3/4" / 15' 5-3/4"	Vertical
B-W-L	10-1/4"	Horizontal
D-W-L	3' 2-3/4" / 8' 5-3/4"	Horizontal
T-W-L	6' 5-3/4" / 15' 5-3/4"	Horizontal
T-W-C	6' 5-3/4" / 15' 5-3/4"	Horizontal

In order to monitor the load from the hydraulic rams, four pressure cells were installed on the advanced side of each ram for the axial load application and one was installed for the shear load application, as shown in figure 3.16. One additional pressure cell was located just before the 4-way splitter for the axial load hydraulic lines as a reference point to crosscheck the other pressure readings. The load readings from the pressure cells served to validate the strain gage readings.

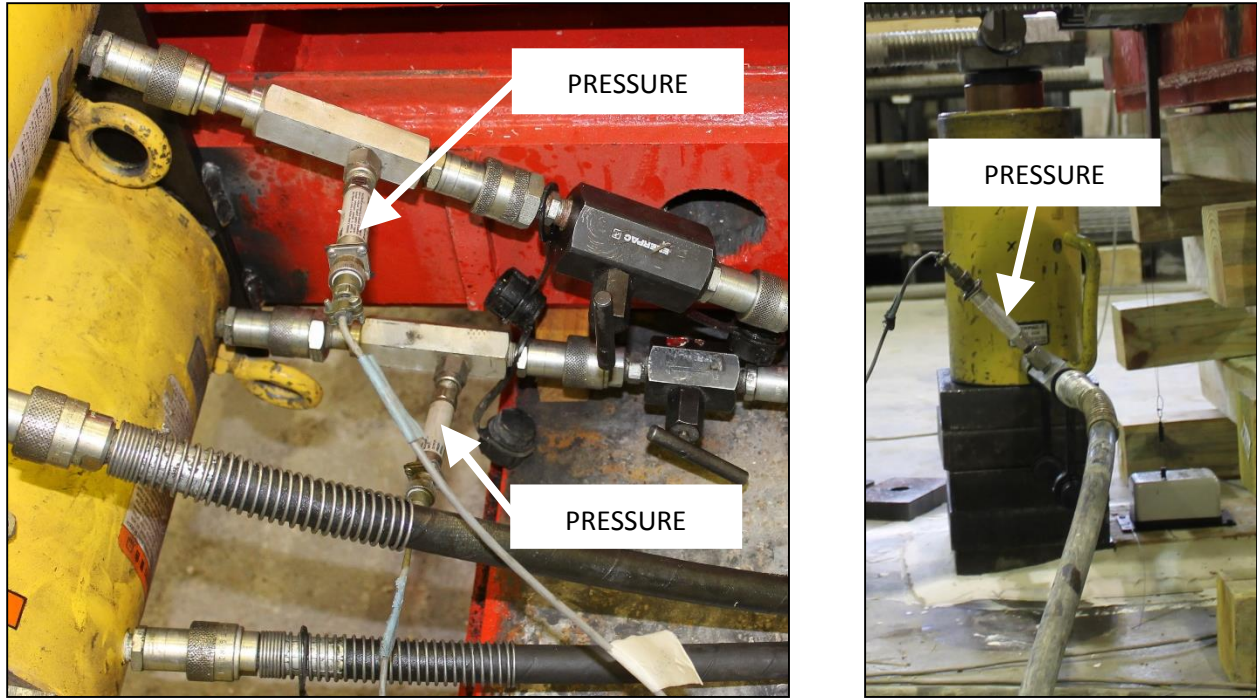


Figure 3.16 Pressure cell locations

3.6 Procedure

For each test, the instrumentation was powered and zeroed through a NI DAQ with a user interface developed by a third party. Once the instrumentation was ready, the axial and shear forces were alternately applied in a stepped fashion. The application of the axial force was controlled via a pendant that connected to the large stationary hydraulic pump, while the shear force application was controlled by a trigger on a portable hydraulic pump. This stepped approach allowed the loading to approximately follow the intended loading rate, although load application was not as precise as for a servohydraulic actuated system. After the max axial load of 350 kips was reached, the hydraulic lines to the stationary pump were held constant with a check valve, and the loading continued with the single ram applying the shear load. This load was applied at a rate of a trigger pull approximately every four seconds, which was consistent with ASTM E8.

Alterations to the loading protocol were required for the retrofit cases. The retrofitted pile bent was tested first. The retrofitted bent was subjected to a sequence of axial loads and shears consistent with the non-deteriorated bent case. The weight of the concrete at the retrofit location altered the moment distribution along the length of the specimen from the non-retrofitted cases, so the moment at the base was less for the retrofit case than the non-retrofitted cases when the axial target load was attained. This loading sequence did not affect the ultimate behavior of the specimen. Additional shear load was required to achieve the ultimate state, but the quantities of interest were the axial load and moment, which were monitored by strain gages. The retrofitted abutment case was subjected to a relatively large initial axial step (about 4 times a normal step), followed by application of shear until the retrofit concrete was raised from blocking and the moment at the base increased to arrive at the typical 80/20 target loading ratio. Axial and moment demands were then induced similarly to other tests to follow the 80/20 ratio and then increase moment to ultimate strength.

Although the axial load was nominally held constant by maintaining constant pressure to the axial loading rams after initially reaching 350 kips, the axial force was observed to decrease with increasing flexure. When the axial load fell below 330 kips, additional pressure was applied to the axial rams to restore the axial load to 350 kips. This process of shear loading and maintaining 350 kips axial load was continued until an appreciable amount of softening was observed. Softening indicated instability, and therefore established the failure state and end of a test.

Chapter 4 Data Processing

Axial force and moment were inferred from measured strains at both the base section and the deteriorated section. These calculations were performed both during the test and in post-processing, with maximum load and other key values determined in post-processing.

Loads applied during the test were governed by calculations performed by the data acquisition system (DAQ) in real-time to comply with the experiment protocol described previously. Calculations performed during the tests assumed linear elastic behavior under combined loading. The average compression stress on a cross-section was determined by finding a mean strain for the flange gages and applying Hooke's law to correlate strain to stress. Axial load was then obtained from average stress multiplied by the gross cross-section area. Axial load, and resolving the average stress into the axial force on the cross-section by multiplying stress times area. For example, at the base section:

$$Axial\ Load = \frac{(BTFL + BTFR + BBFL + BBFR)}{4} * E_s * A$$

The variables enclosed in the parentheses for the first term refer to strains at gage locations noted in table 3.2. E_s is the uniaxial Young's Modulus for steel, taken as 29,000 ksi, and A is the cross-sectional area of the test specimen. Moment was similarly evaluated by applying small deflection classical mechanics relating curvature to the ratio of moment to flexural rigidity, EI . Curvature was evaluated from the difference of the average flange strains, divided by the distance between measured strain locations, i.e., section depth, d . At the base section, using the same strain gages as in the axial load determination:

$$Moment = \frac{(BTFL + BTFR) - (BBFL + BBFR)}{2d} * E_s * I_x$$

The variables in the moment equation are identical to those in the axial load equation, except for the use of section depth, d , and strong axis moment of inertia, I_x . These elastic calculations were employed as feedback to control application of load throughout tests.

After the testing was complete, the data was exported and analyzed using Matlab. Using the steel yield strength gained from the material testing, the strain values recorded during the test were converted into axial forces and moments for the base and deteriorated cross sections. The same equations (above) were utilized for each case when the cross section being analyzed remained elastic. When a portion of the cross-section exceeded experienced strains exceeding the yield strain, a fiber analysis was employed to capture the effect of material nonlinearity. Residual stresses were not considered in the fiber analysis, or the condition for which fiber analysis would apply.

Local buckling influenced recorded strains at highly inelastic flanges, making the recorded strain data unreliable. To circumvent the local buckling influence on recorded data, effective average strains were extrapolated from the lower half of the test specimen using bottom flange and web mid-depth strain measurements as references. The fiber analysis was performed as follows:

1. Determine the approximate cross-section curvature as the linear variation of the strain between the bottom flange (average of two gages) and the mid-depth of the web.

$$Curvature = \frac{2(\varepsilon_{web} - \varepsilon_{bot})}{d}$$

- Determine strains at centroids of each fiber layer, ϵ_i , assuming plane sections remain plane. Referring to figure 4.1, for any layer i with a centroid a distance y_i from mid-depth of the specimen:

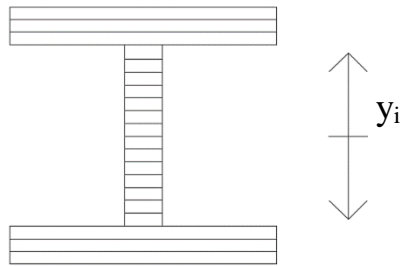


Figure 4.1 Partitioned cross-section for fiber analysis

$$\epsilon_i = \text{Curvature} * y_i + \epsilon_{web}$$

- Determine stress at each fiber, σ_i , by applying Hooke's Law for fibers in the elastic range. Limit the maximum stress on any fiber to the yield stress, as represented in figure 4.2.

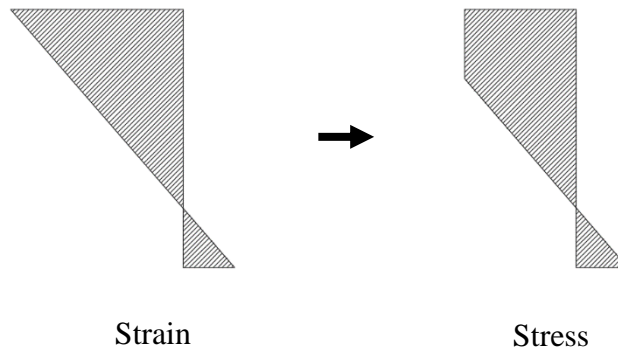


Figure 4.2 Strain to stress conversion with yielding

$$\sigma_i = \text{signum}(\varepsilon_i) * \min\{ |\varepsilon_i| * E_s, f_y \}$$

4. Resolve the stresses on each fiber into axial forces per fiber, P_i , by multiplying the stress at each fiber by the corresponding fiber area, as represented in figure 4.3. The total axial force on the cross-section is the sum of fiber forces.

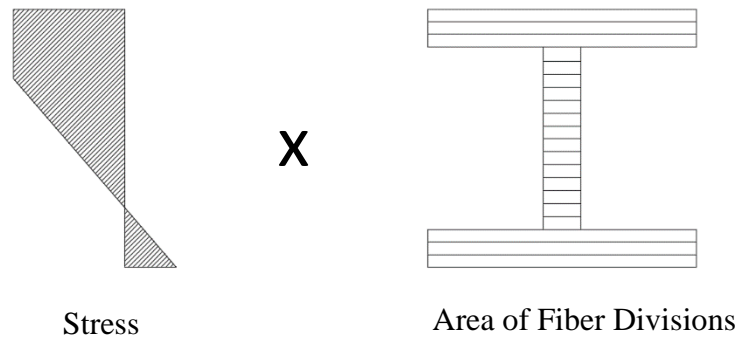


Figure 4.3 Components of fiber forces: stress and area at each fiber

$$P_i = \sigma_i * A_i$$

$$\text{Axial Force} = \sum P_i$$

5. Calculate the cross-section moment by finding the contribution from each fiber, M_i . Each fiber moment contribution is the force at the fiber times the distance y_i (centroid of section to centroid of fiber). The total moment on the cross-section is the sum of fiber contributions.

$$M_i = P_i * y_i$$

$$\text{Moment} = \sum M_i$$

Calculations for the deteriorated section were similar to the fiber analysis, although more coarse. The deteriorated section effectively consisted of three elements, as shown in figure 4.4. Each flange was effectively a WT, and the web was a rectangular bar. Strains were averaged at each flange, and considered representative for the WT element as a whole. Strains were converted to stresses, stresses to forces, and forces to resultant axial load and moment, as described previously for the fiber analysis. Moment calculations only required a single scalar value for y_i to represent the distance from the mid-depth of the section to the centroid of each WT element as shown in figure 4.5.

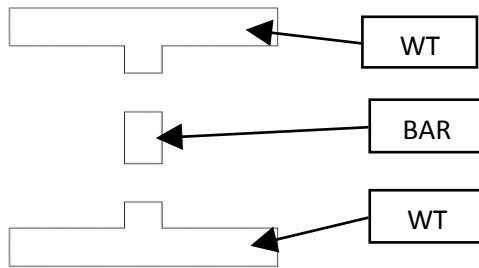


Figure 4.4 Deteriorated section elements for analysis

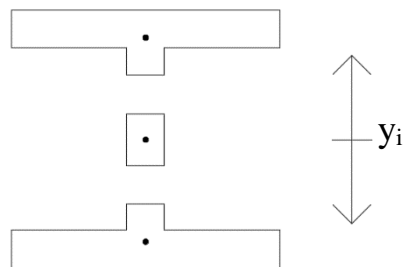


Figure 4.5 Moment arm distances for deteriorated section elements

Chapter 5 Experimental Results

Individual test results are presented in this section, together with comparisons of deteriorated and retrofitted behavior to non-deteriorated specimen results for each configuration (abutment and bent). Information is provided in graphical form for axial load and moment (P-M interaction plot), shear and displacement, and strain measurements at the base and deteriorated sections. Details of the actual material strengths are also presented. These material strengths were used to update the calculations from the experimental design section and used in calculations presented in the data processing section. First yield at any strain measurement location is noted in the data plots, as well as the end of the 80/20 loading, maximum shear, and web yield (if applicable).

5.1 Material Testing

Material tests were performed on steel and concrete specimens to characterize physical parameters (yield stress, peak compression stress, etc.) representative of the individual components of the test specimens. Two sets of steel samples were tested: one set for the abutment pile non-deteriorated case and one set for all other cases. Two steel sample sets were required because the non-deteriorated abutment pile was procured separately and was produced in a different heat than the other specimens. This was not the case for the concrete as both retrofit jackets were placed at the same time, so one set of samples was sufficient to represent the concrete for both retrofit specimens.

Actual steel yield strengths obtained from the tensile tests are provided in table 5.1. The measured yield strengths are 5 and 6 ksi above the nominal yield strength of the steel (50 ksi). Average stress/strain curves obtained from the steel coupon tests are shown in figure 5.1 and figure 5.2.

Table 5.1 Steel yield strength results

	Steel Yield Strength
Remaining Abutment Case and Pile Bent Case Piles	56 ksi
Abutment Case, Non-deteriorated Pile	55 ksi

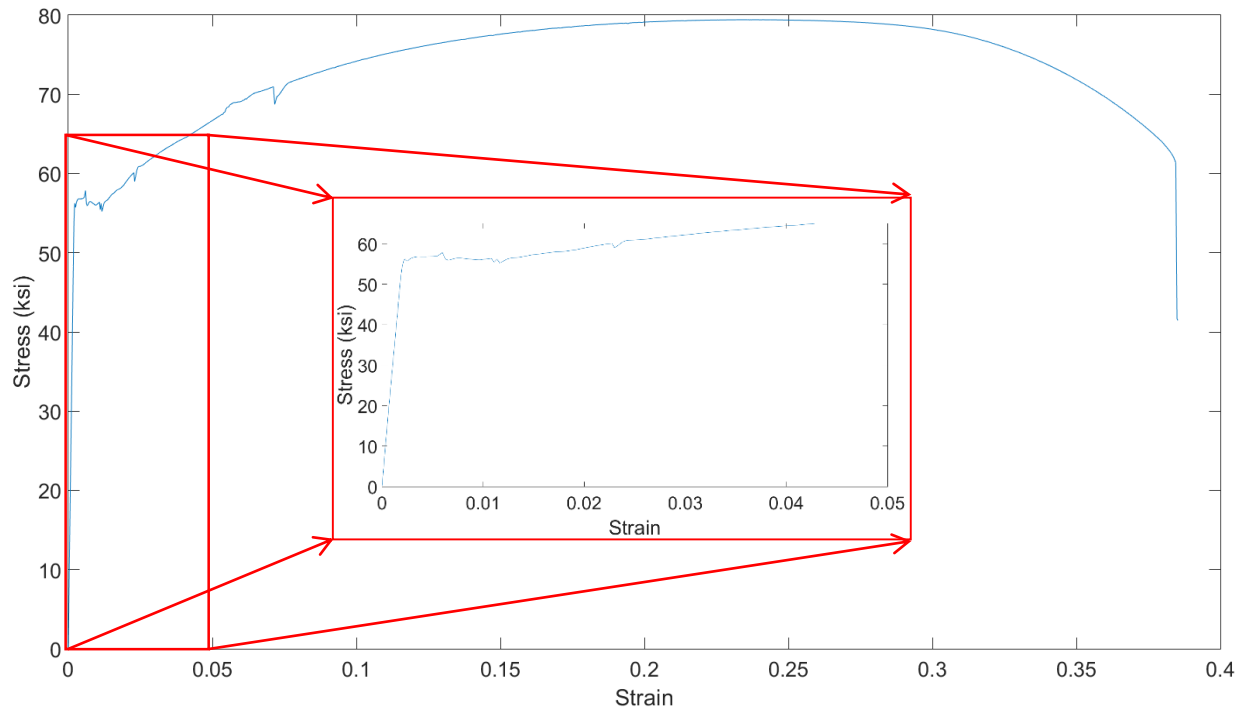


Figure 5.1 56 ksi stress vs. strain

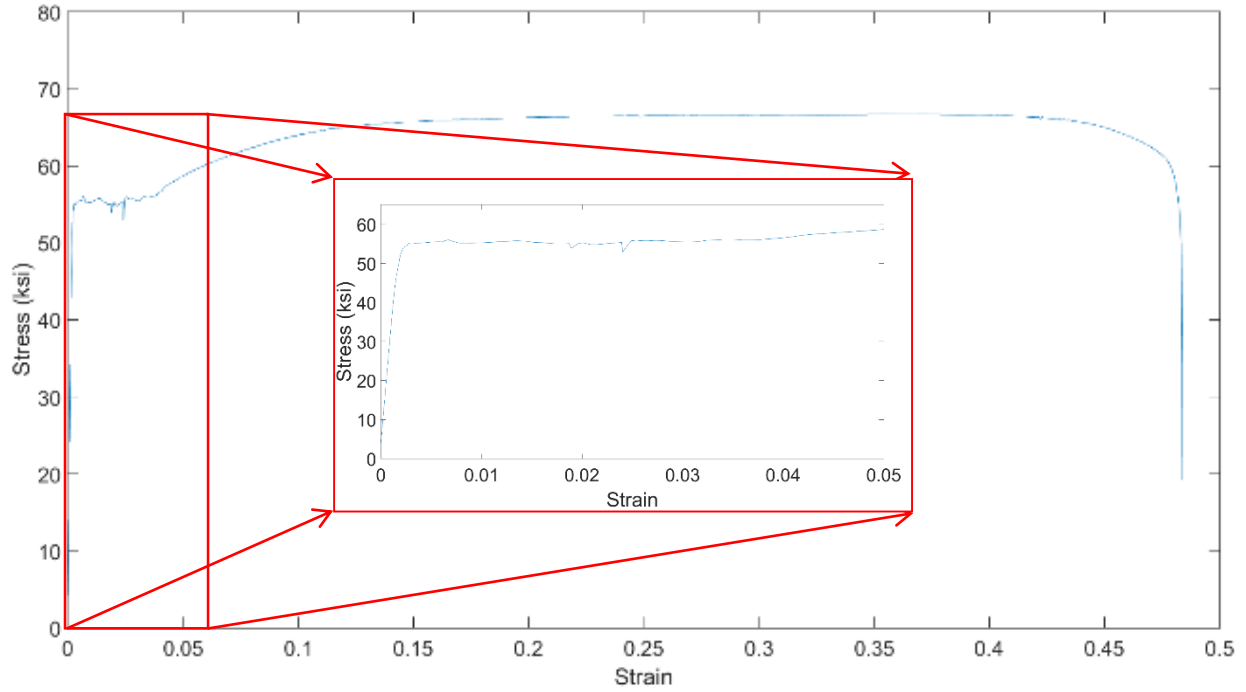


Figure 5.2 55 ksi stress vs. strain

Concrete cylinder samples were tested at 3, 7, 14, and 28 days. The samples met the specified compressive strength, f_c' , of 3,000 psi within three days and were more than double f_c' at 28 days. These results are presented in table 5.2 and figure 5.3.

Table 5.2 Concrete strength results

	Sample A	Sample B	Sample C	Average
3 Day Break	4,244	4,456	4,038	4,246
7 Day Break	5,116	5,014	5,036	5,055
14 Day Break	5,551	5,720	5,821	5,697
28 Day Break	6,157	6,648	6,530	6,445

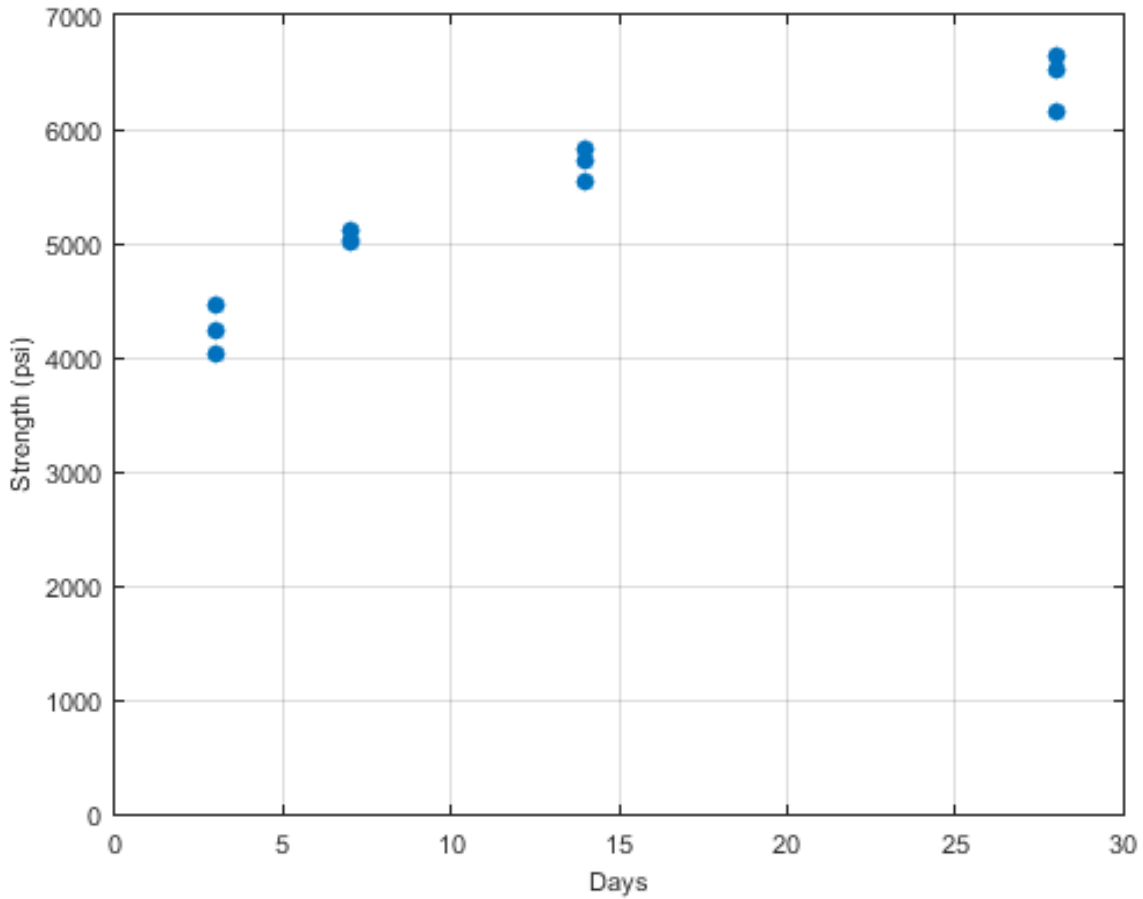


Figure 5.3 Concrete strength vs. days

5.2 Abutment Case: Non-Deteriorated

The non-deteriorated abutment test setup is shown in figure 5.4. Based on the calculations using AISC (2010) methodology, the pile was expected to experience compression flange local buckling in pure flexure and flange local buckling in pure compression. Since both the compression and flexure limits had similar failure cases, local buckling failure of the top flange near the base end of the pile was anticipated and was observed, as shown in figure 5.5. The pile performed as expected and provided a sound baseline against which to compare the remaining abutment tests.



Figure 5.4 Non-deteriorated abutment test



Figure 5.5 Buckling of base section top flange

Yielding and local buckling progressed slowly and gradually after the steel reached its combined P-M loading limit. The stockiness of the pile's cross section, coupled with its relatively short overall length, provided a great deal of stiffness and allowed the section to carry loads near the material's plastic limit, as illustrated in figure 5.6.

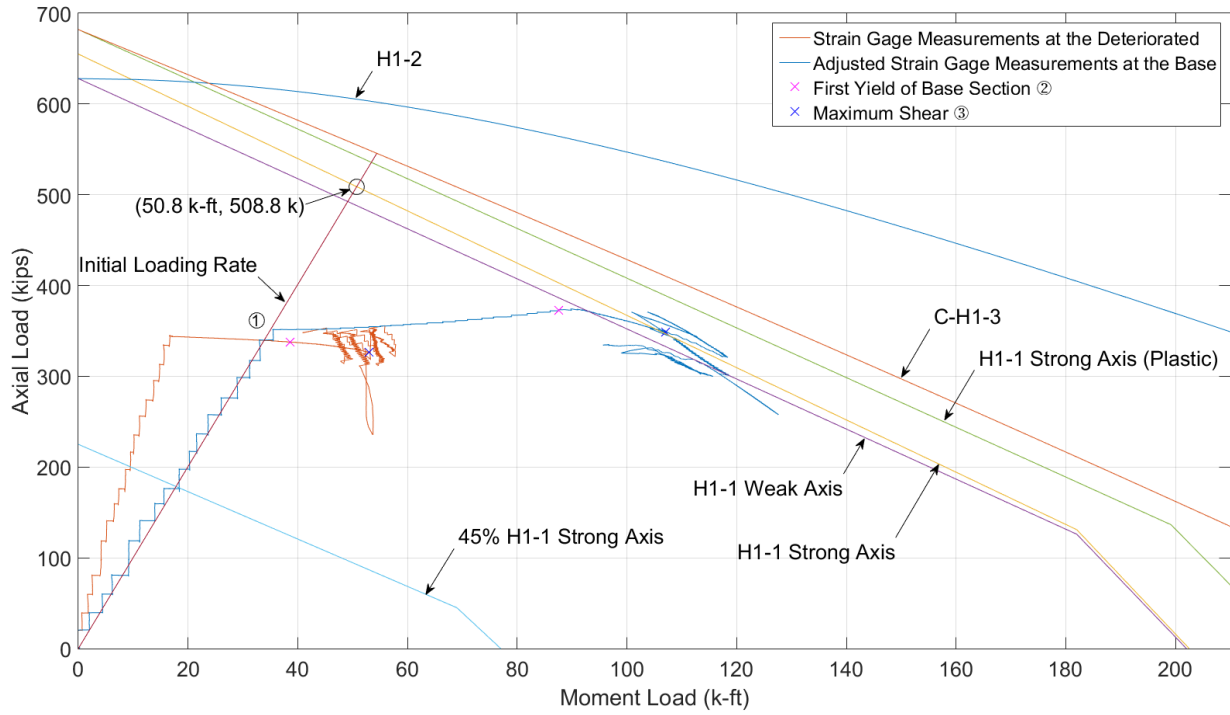


Figure 5.6 Non-deteriorated abutment case axial vs. moment

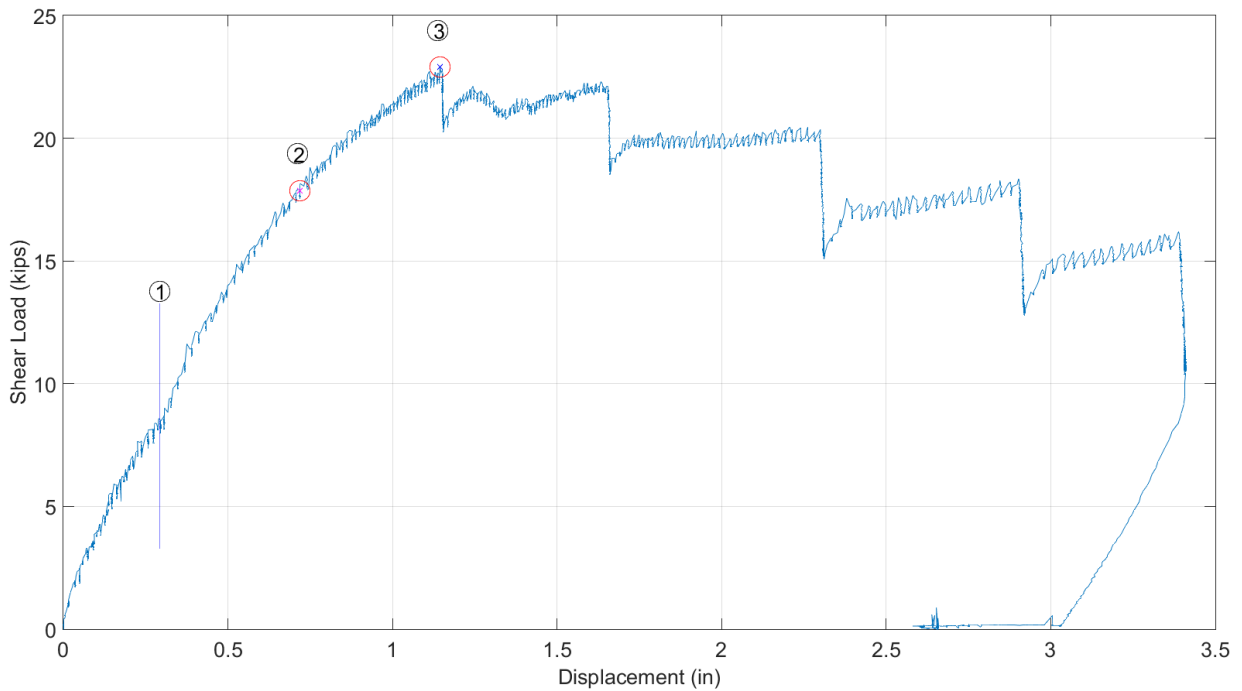


Figure 5.7 Non-deteriorated abutment shear vs. displacement

Once the pile began to trace along the P-M capacity envelope, increases in either axial or shear load resulted in decreases of the alternate load (increase in axial results in decrease of moment and therefore shear, and vice versa). This effect is observed in figure 5.7, where axial load corrections to maintain 350 kips corresponded to drops in shear at displacements of about 1.2, 1.65, 2.35, and 2.9 inches. This load shedding resulted from combined P-M plastic section load capacity and moment amplifications from second-order effects with increasing eccentricity of axial loading.

Second order effects can also be seen in the deteriorated section response in figure 5.6. The deteriorated section traces parallel P-M responses to the base section, but the interaction limit surfaces recede toward zero moment as the experiment progresses. Less shear-induced moment is required as second order effects contribute greater proportions of moment to the yielding base section. The reduced shear demand is reflected in the lower moments induced at the deteriorated section.

Strain response is shown in figure 5.8 and figure 5.9 for the base and deteriorated sections, respectively. Local buckling caused strains measured at BTFL to increase drastically, representative of both the compression developed at the top of the section due to flexure compounded by local buckling deformations. At the elastic deteriorated cross-section, all strains trend negatively (compression) up to the encircled 1 where 80/20 loading ended. The load was held constant for a short time, followed by application of additional shear causing broader divergence of relative tension (tending toward positive) and compression (tending toward negative) in flexure.

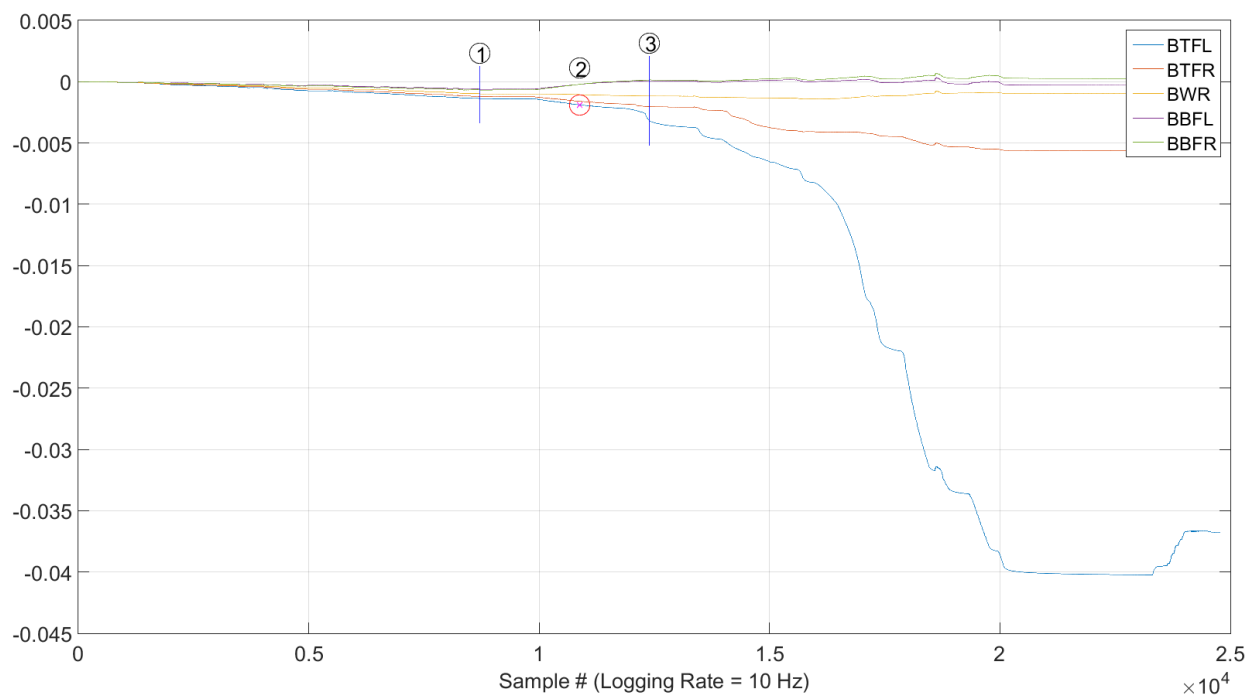


Figure 5.8 Non-deteriorated abutment base section strain vs. sample

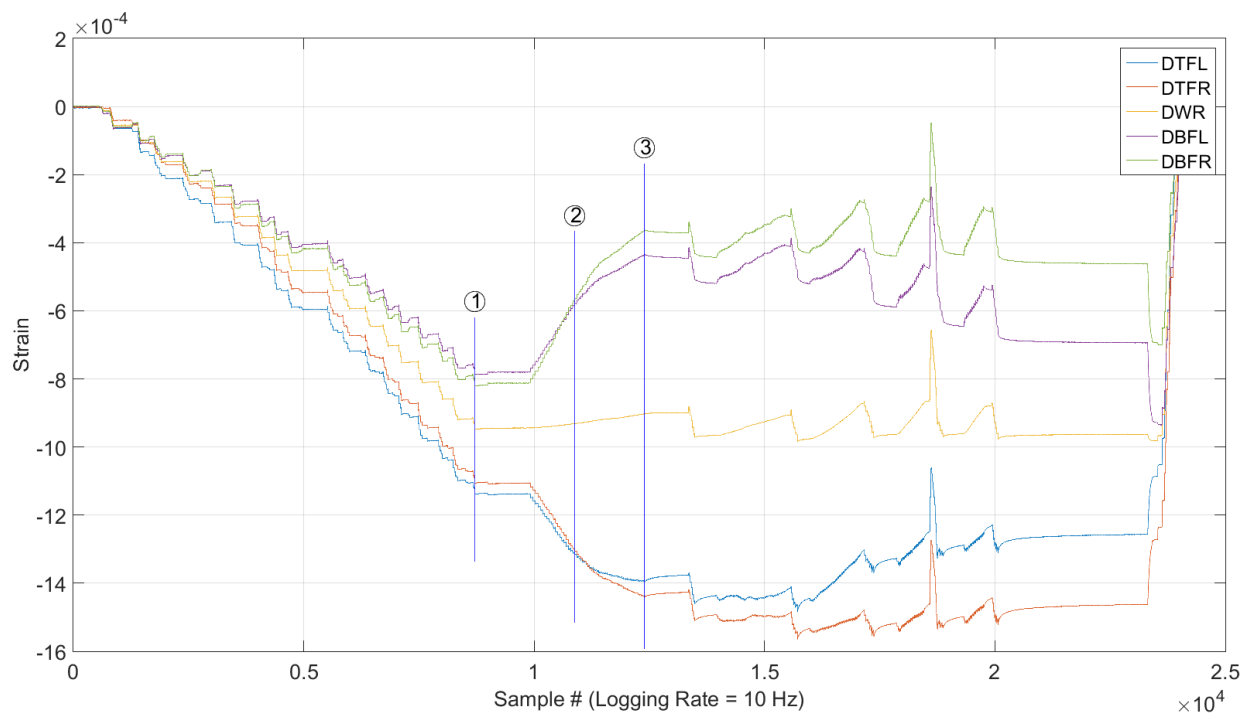


Figure 5.9 Non-deteriorated abutment deteriorated section strain vs. sample

5.3 Abutment Case: Deteriorated

The deteriorated abutment case test setup is shown in figure 5.10. Failure occurred by initial local buckling of the milled flange region. The deteriorated region initially resisted applied loading as a frame, but the top flange portion of the deteriorated section could not fully participate in resisting additional applied loads after local buckling occurred. Subsequently, the web region of the deteriorated section provided primary resistance to shear racking deformations. The web region developed plastic hinges at each end of the deteriorated region, as illustrated in figure 5.11 and figure 5.12, and instability of the specimen against combined loads. Local buckling effects and load redistribution effects are evident in figure 5.13. Strain measurements at the top flange and web deviate from the trend of the group near the 10,000 sample mark.



Figure 5.10 Deteriorated abutment test



Figure 5.11 Deteriorated abutment test: deteriorated section before and after

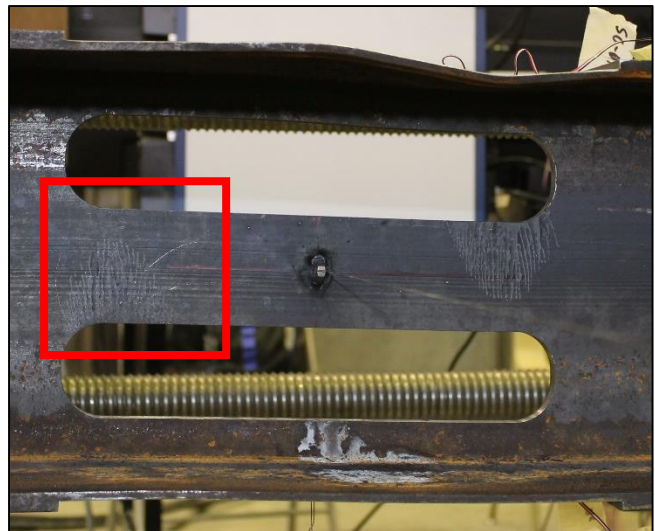
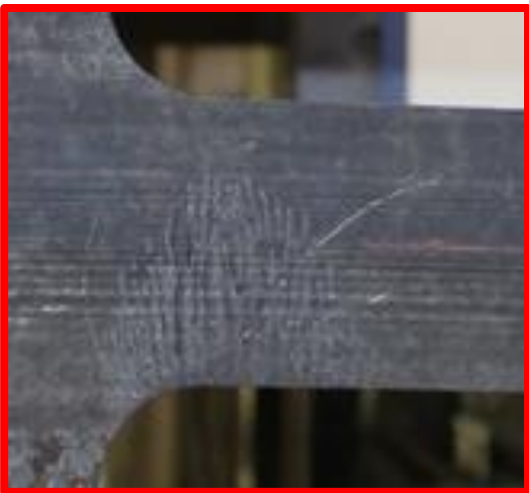


Figure 5.12 Deteriorated abutment shear failure at the deteriorated section

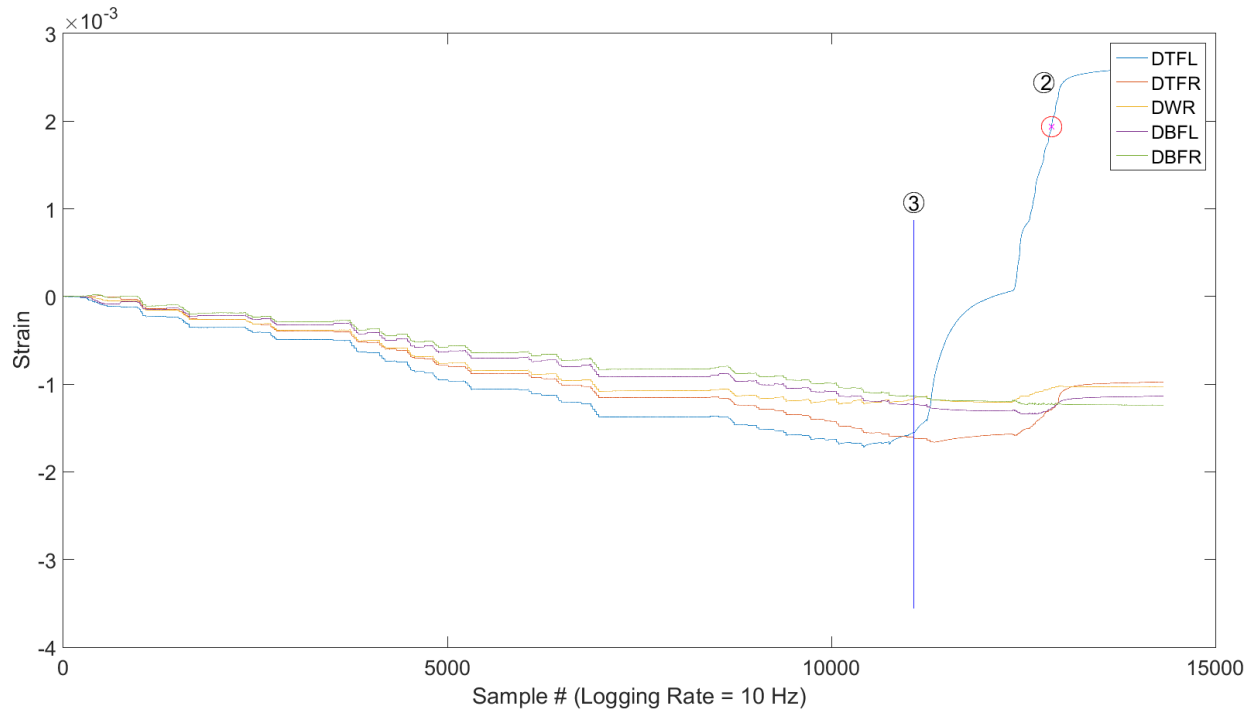


Figure 5.13 Deteriorated abutment deteriorated section strain vs. sample

Preliminary analyses estimating the capacity of the specimen neglected capacity beyond local buckling of the deteriorated flange, but the experiment displayed significant capacity in excess of that anticipated prior to instability. The anticipated pile capacity is plotted in figure 5.14 and shows that the pile axial capacity exceeded 250 kips in compression, more than 25% higher than the anticipated 200 kip limit for the deteriorated section. Figure 5.15 and figure 5.16 provide additional data for the shear load and the base section strains, respectively, for comparison with other abutment scenario cases. Strains at the base section remained well within the elastic range.

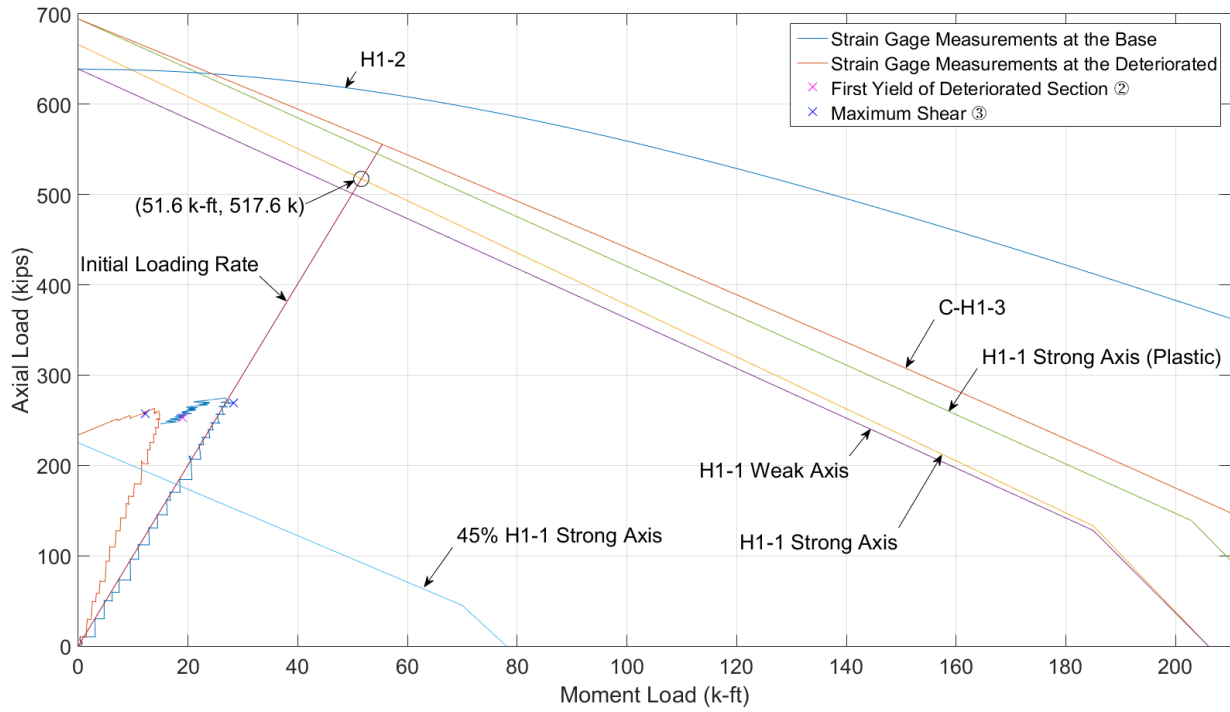


Figure 5.14 Deteriorated abutment axial vs. moment

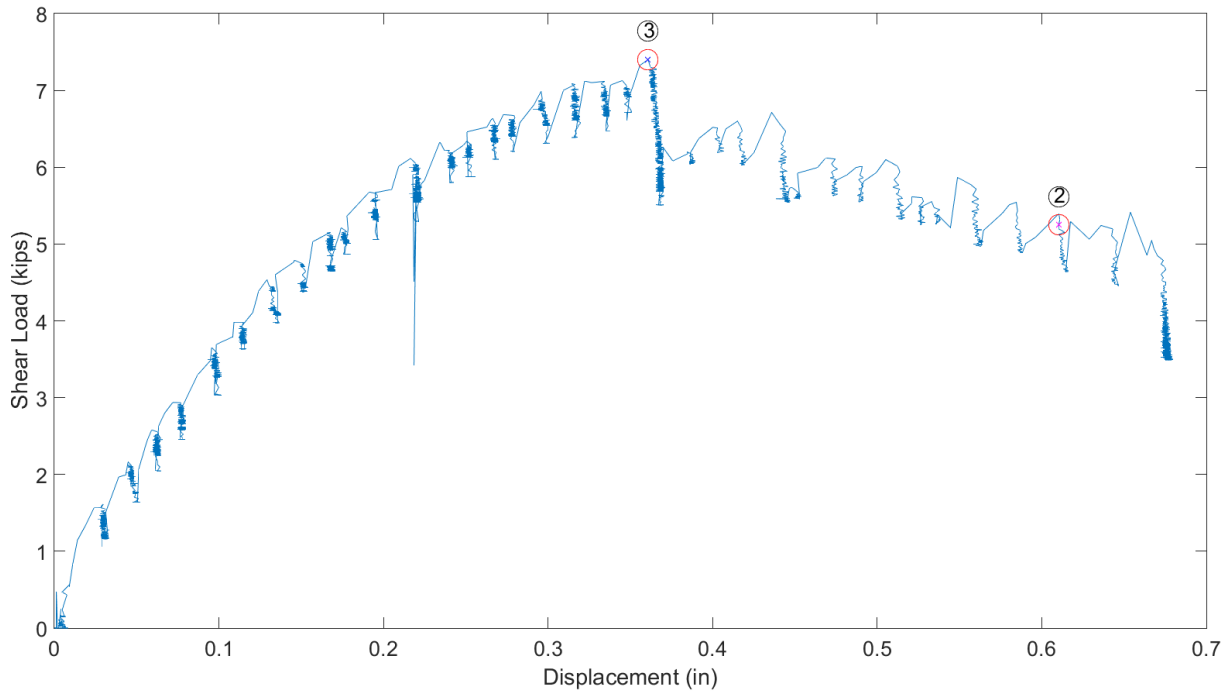


Figure 5.15 Deteriorated abutment shear vs. displacement

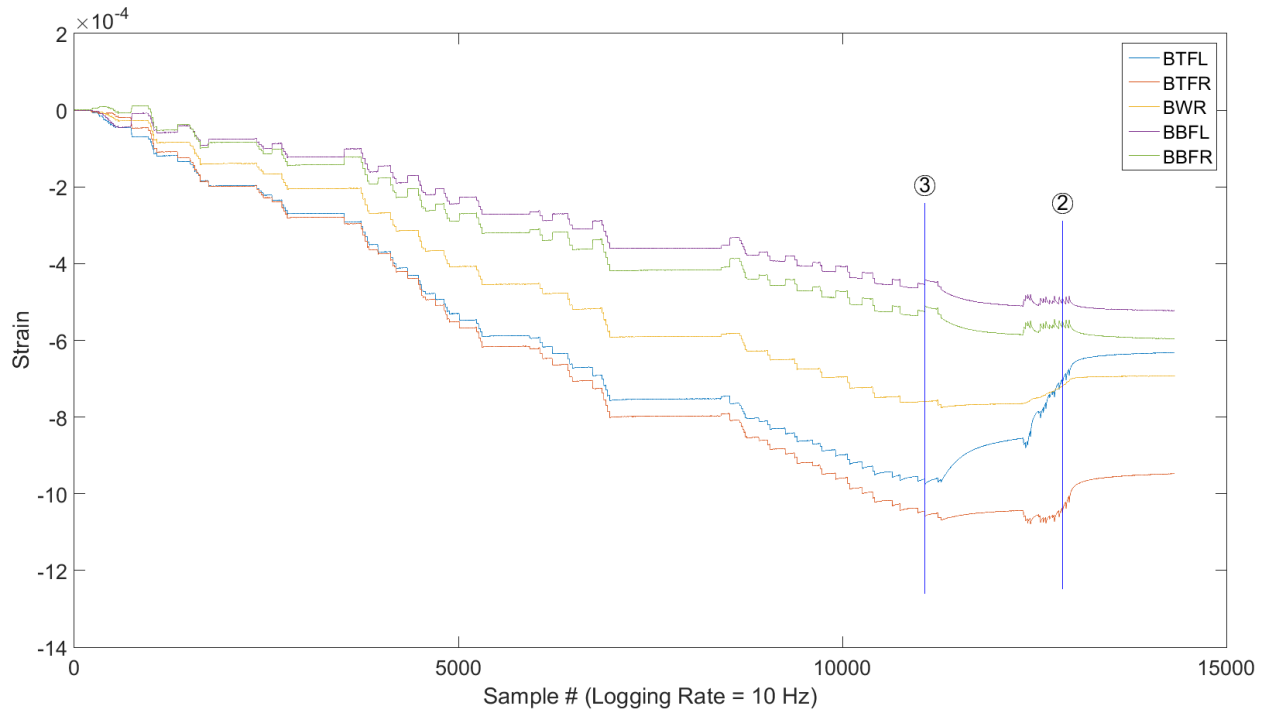


Figure 5.16 Deteriorated abutment base section strain vs. sample

5.4 Abutment Case: Retrofitted

The retrofitted abutment test setup, shown in figure 5.17 performed as intended by stabilizing the deteriorated section and restoring the pile to its original non-deteriorated strength. The pile was able to withstand the same loading as the non-deteriorated pile and even carried a slightly higher shear load. An increase in stiffness was an additional benefit and the buckling failure seen in the deteriorated test was eliminated.



Figure 5.17 Retrofitted abutment test

The pile failed in a similar manner to the non-deteriorated pile, with a local buckling failure at the base outside of the retrofitted section. The pile experienced local buckling at the top flange, as illustrated in figure 5.18. The retrofit provided bracing for the cross-section of the pile and held the all plate elements of the cross-section rigidly in place, causing the buckling zone to be shorter than in the non-deteriorated test.



Figure 5.18 Retrofitted abutment base section failure

Figure 5.19 shows that the deteriorated steel section supported less than 100 kips of axial load and only 10 k-ft of moment. The recorded strains at the deteriorated steel section are plotted in figure 5.20, showing that yield strains (approximately 19×10^{-4}) were not reached at any location. This data indicates that the concrete bond was substantial and the retrofit drew a considerable amount of load, despite the lack of mechanical connectors. The bond strength anticipated for this retrofit was 71 kips. From the strain gage data within the concrete jacket, the maximum axial load carried by the pile was 93 kips of the total 333 kips applied to the specimen at that time. The remaining 240 kips were carried by the jacket through the concrete/steel bond. This indicates a minimum bond of 203 psi, which is 3.38 times greater than the AISC (2010) recommended value.

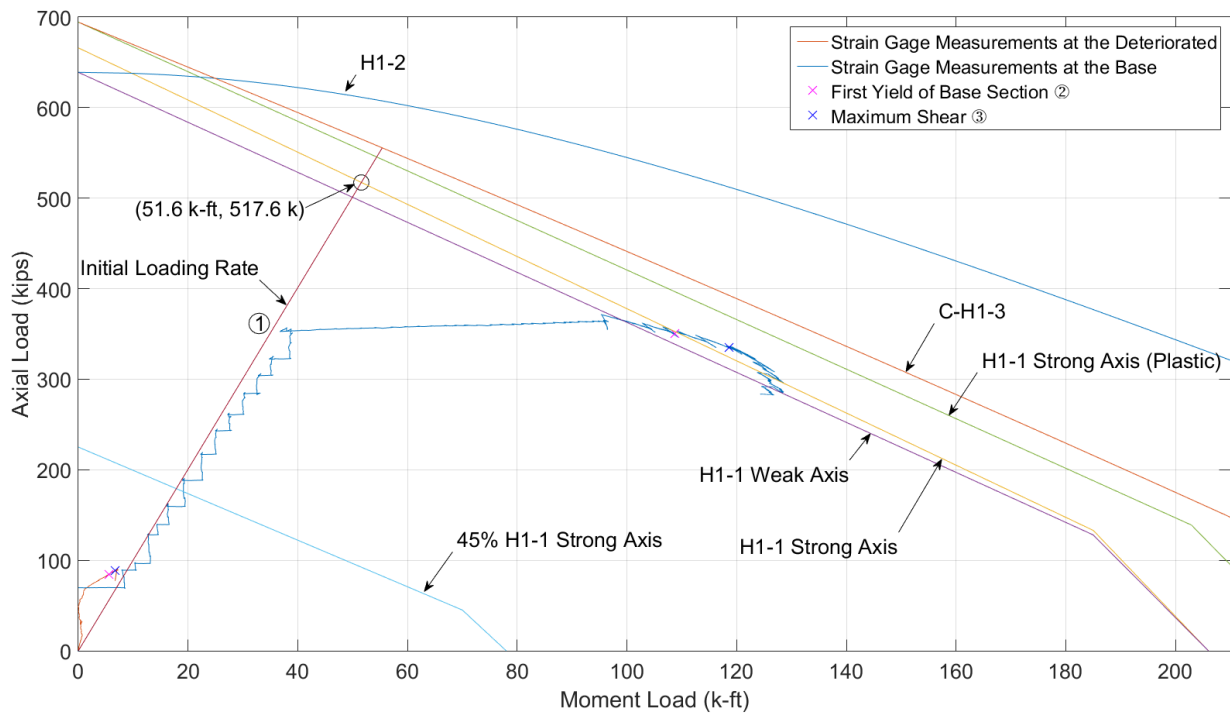


Figure 5.19 Retrofitted abutment axial vs. moment

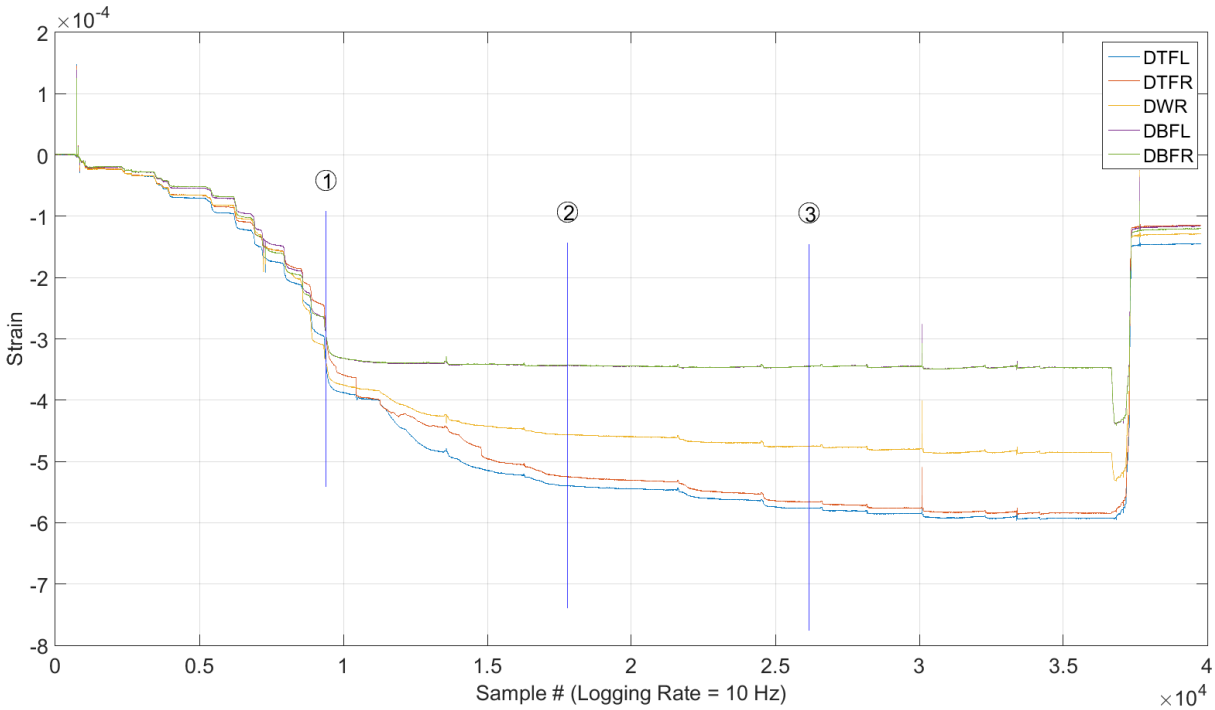


Figure 5.20 Retrofitted abutment deteriorated section strain vs sample

The pile experienced less displacement in comparison to the non-deteriorated case, as shown in figure 5.21. The added stiffness allowed the pile to carry greater load prior at instability in comparison to the non-deteriorated case because stiffening afforded by the retrofit reduced the influence of second order effects. The retrofitted specimen required an increase of 2 kips in shear to reach instability, an increase of 9% over the non-deteriorated case. Similar to the non-deteriorated test, instability resulted from yielding and local buckling at the top flange of the base section. Figure 5.22 shows the recorded strains at the base, confirming that strains exceeded the yield limit at the top flange.

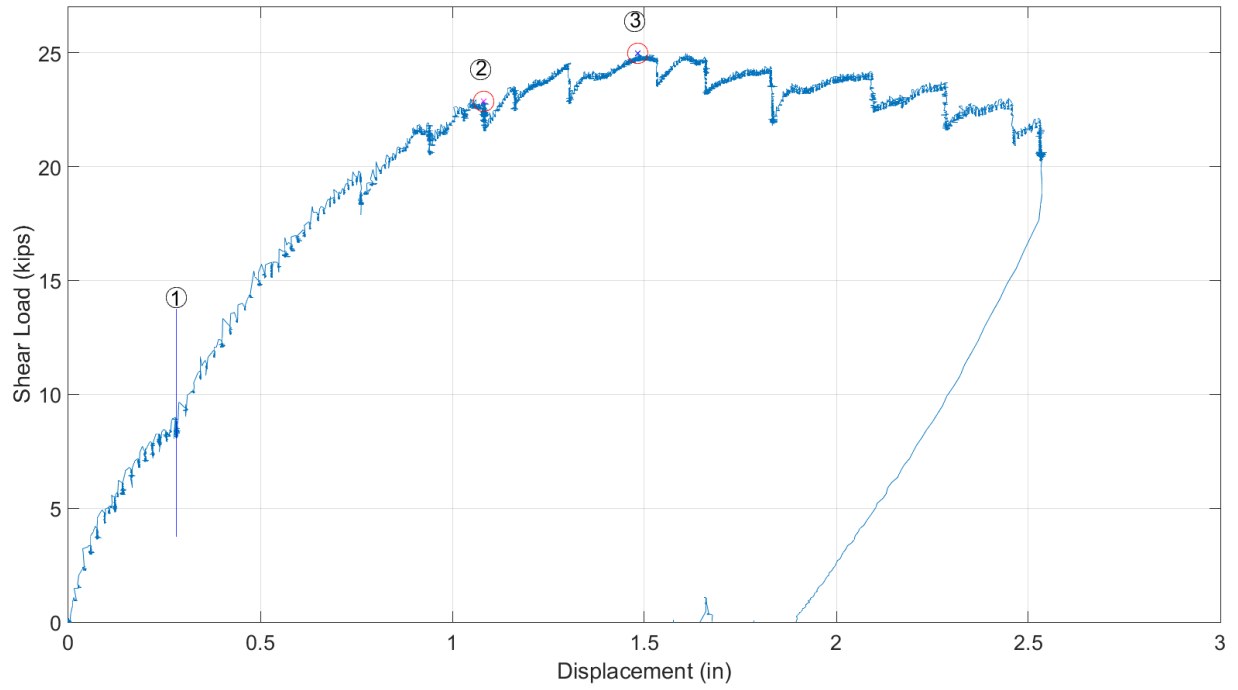


Figure 5.21 Retrofitted abutment shear vs. displacement

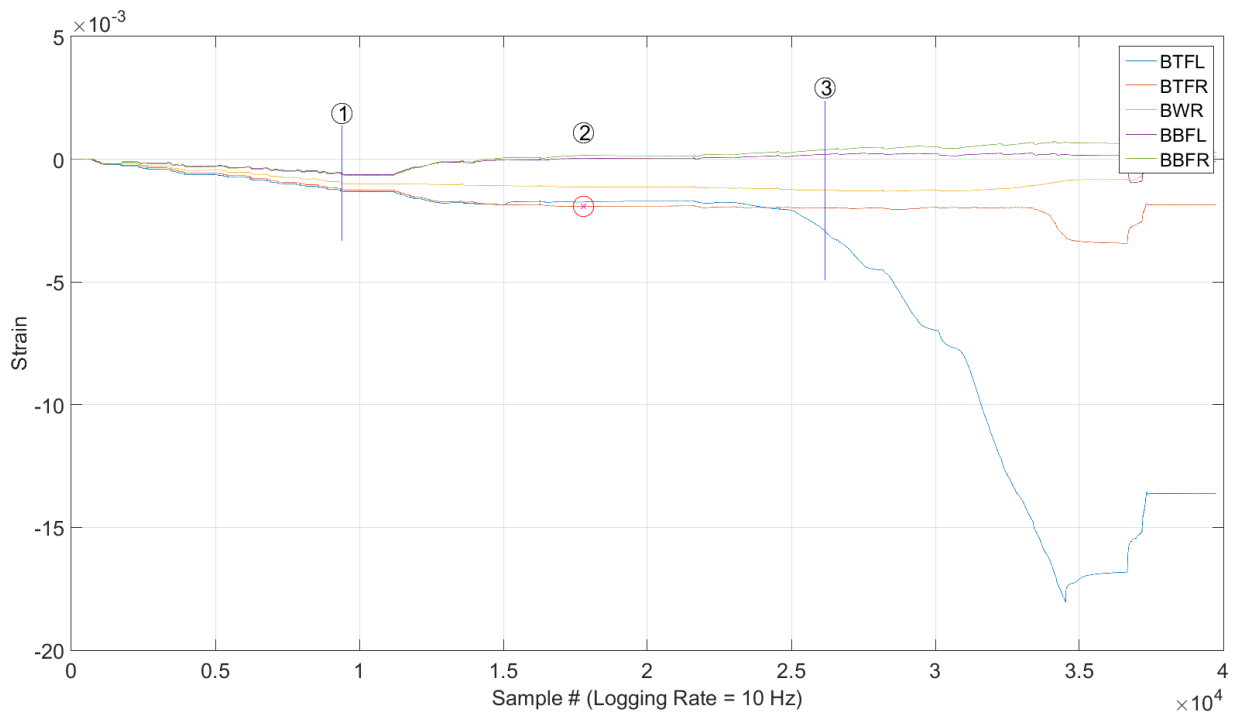


Figure 5.22 Retrofitted abutment base section strain vs. sample

5.5 Abutment Case: Overview

Combined loading results are provided for the base and deteriorated sections in figure 5.23 and figure 5.24, respectively. Each plot shows an overlay of abutment case results for non-deteriorated, deteriorated, and retrofitted specimens. The base section governed the non-deteriorated and retrofitted cases, with practically identical P-M interaction responses in figure 5.23 confirming the effectiveness of the retrofit. Demands developed at the base of the deteriorated specimen were limited by the performance of the milled location. The demands developed at the deteriorated steel section for the retrofitted specimen were far less than either of the other two specimens, although the base demands were identical to the non-deteriorated. The retrofit achieved far greater composite action with the steel than expected, reducing the demand imposed on the deteriorated steel section.

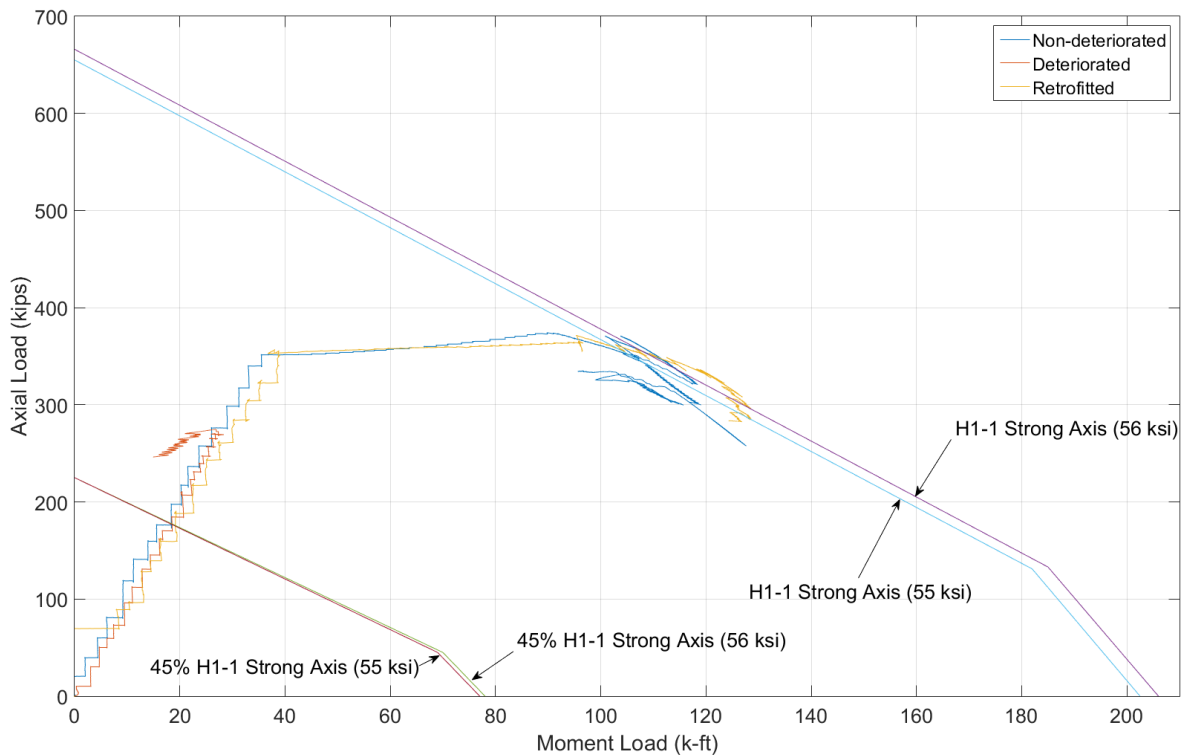


Figure 5.23 Abutment case base section axial vs. moment

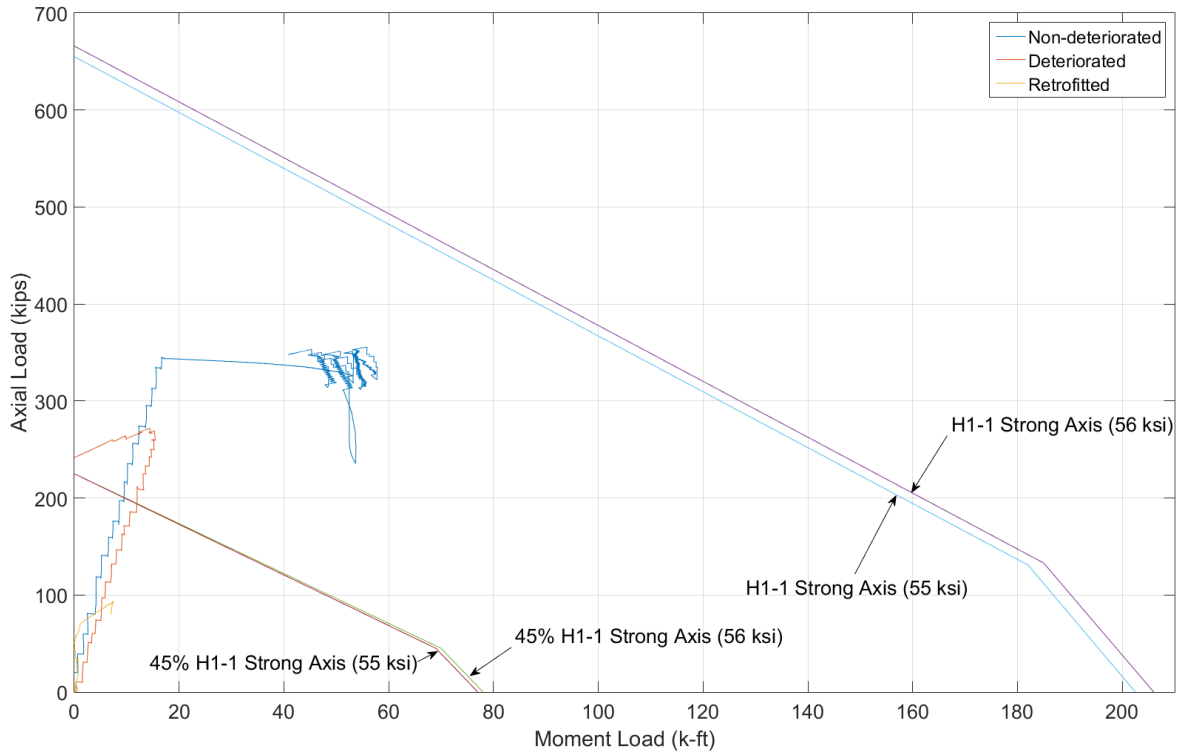


Figure 5.24 Abutment case deteriorated section axial vs. moment

5.6 Pile Bent Case: Non-Deteriorated

The non-deteriorated pile bent case is shown in figure 5.25. The first limit to occur for this specimen was yielding and local buckling at the base section top flange as shown in figure 5.26, similar to the abutment case. This test also experienced a backward tilting rotation of the tie down spreader beam at the base section, but the specimen capacity was not perceptibly affected by this phenomenon. The loss of boundary condition restraint associated with local buckling and plastification at the base section led to a lateral-torsional buckling (LTB) secondary mechanism, as shown in figure 5.27. This combination of limits constituted the ultimate state for the non-deteriorated bent specimen. The measured strains at the deteriorated section for other specimens are plotted in in figure 5.28. The primarily axial compression response, followed by divergence of strains with increasing shear-induced moment is similar to the data recorded for the abutment

case. However, strains on the left side of the flange show biased compression relative to strains on the right side of the flange for both top and bottom flange beginning around the region marked with encircled 3 and 4. This trend reflects strains developed as a result of lateral deformation during LTB.



Figure 5.25 Non-deteriorated pile bent test



Figure 5.26 Non-deteriorated pile bent local buckling of base section



Figure 5.27 Non-deteriorated pile bent LTB failure

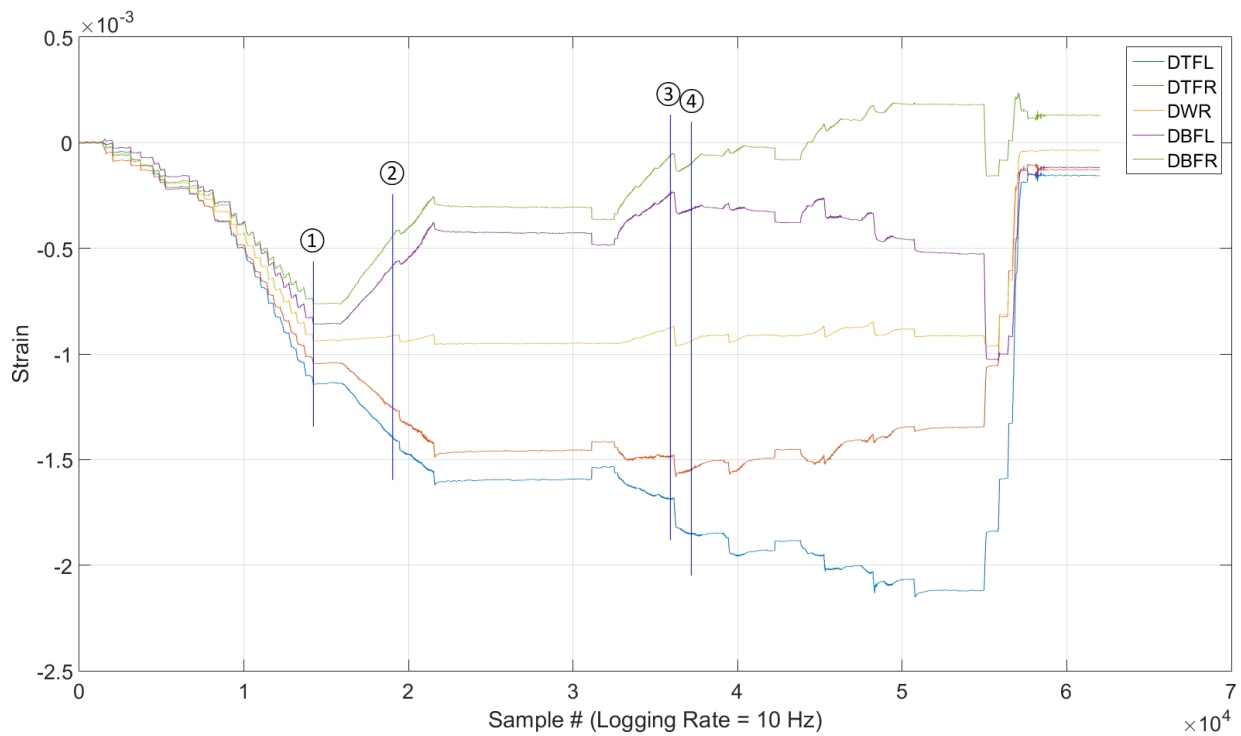


Figure 5.28 Non-deteriorated pile bent deteriorated section strain vs. sample

The non-deteriorated bent test experienced yield penetration to the web strain gage, indicated in figure 5.28 through figure 5.31 with an encircled number 4. The web yield is evident in the recorded strain data for the base section, as shown in figure 5.29. Similar to the non-

deteriorated abutment case, the pile exceeded the H1-1 Strong Axis envelope and failed prior to the H1-1 Strong Axis (Plastic) envelope, as shown in figure 5.30. These results are consistent with expected performance based on preliminary calculations. The H1-1 Strong Axis envelope is anchored by maximum axial and moment capacities limited by flange local buckling, and first yield was in fact observed when the P-M interaction reached this envelope. This envelope is accepted as a reasonable design basis, but the true ultimate strength is not achieved until greater plastification of the cross-section is achieved, as demonstrated by yield strains penetrating at least to mid-depth of the web.

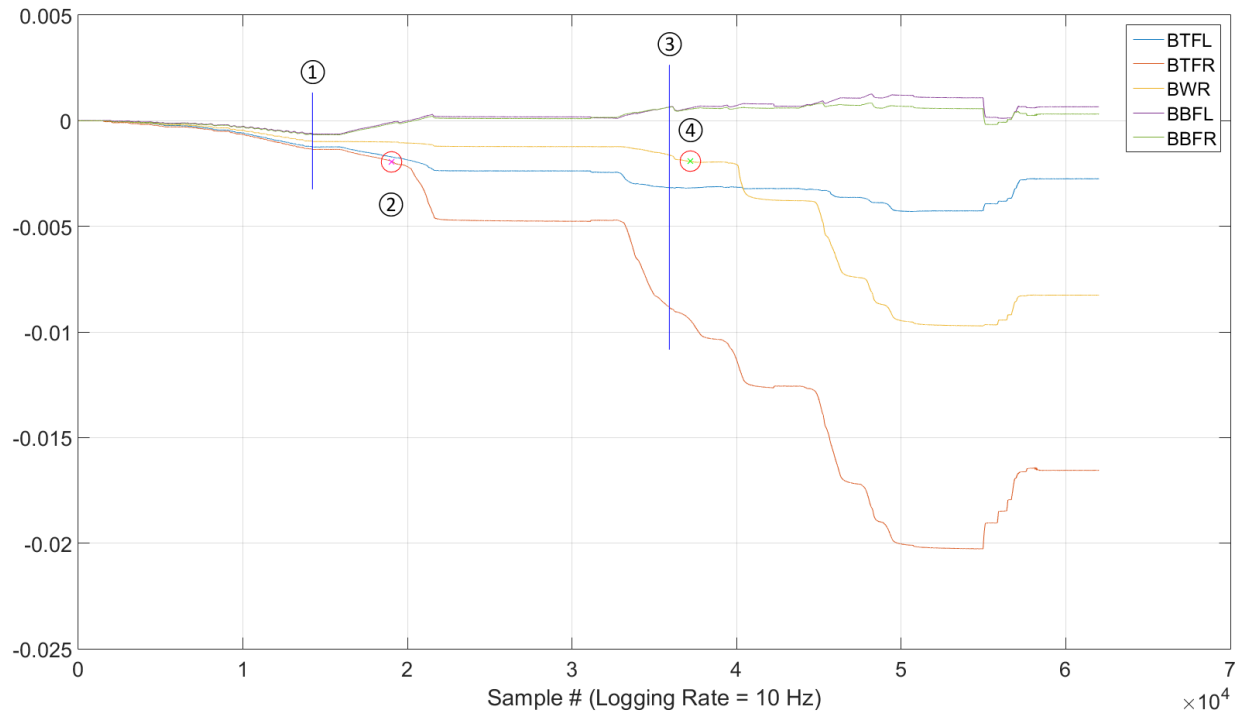


Figure 5.29 Non-deteriorated pile bent base section strain vs. sample

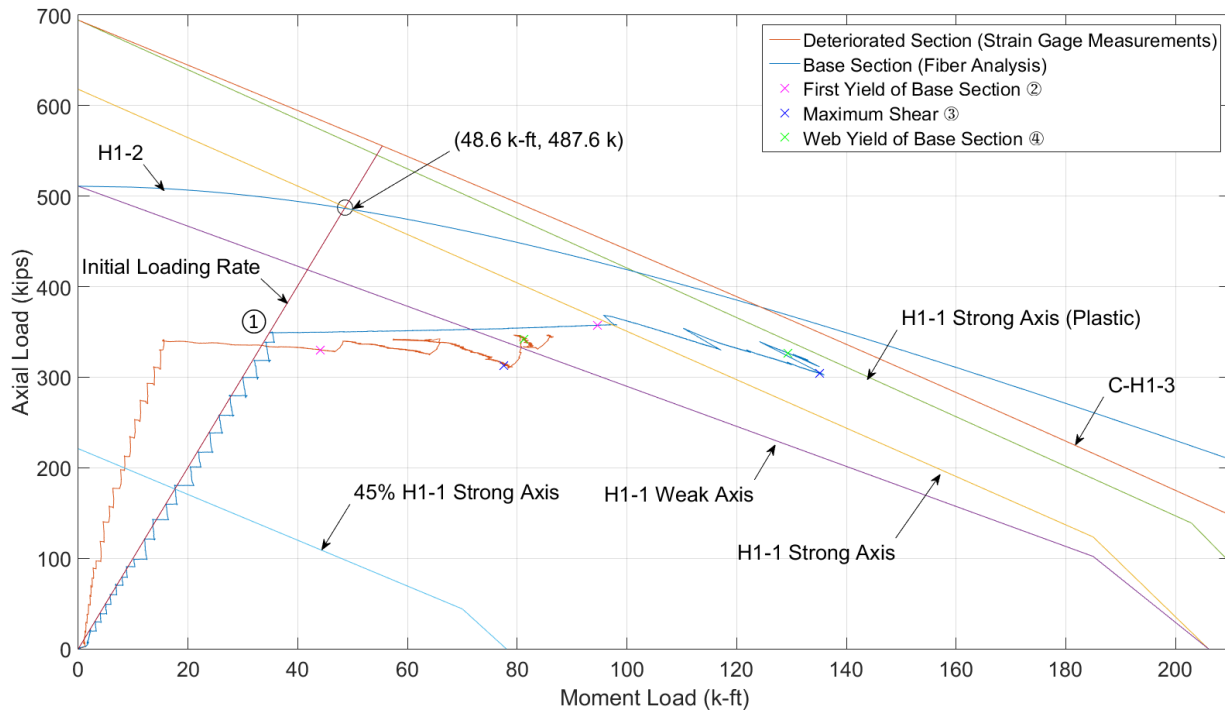


Figure 5.30 Non-deteriorated pile bent axial vs. moment

The moment capacity was similar between non-deteriorated abutment and bent cases, but the shear demand was expected to be lower because of the increased moment arm from shear application to base section, and deflections were expected to be greater because of the longer cantilever length. These expectations were borne out in the response shown in figure 5.31. The shear ram possessed a nominal maximum stroke of about 6 inches, but this displacement was unable to develop the unstable ultimate configuration for the specimen. On two occasions, noted with dashed lines in figure 5.31, the specimen was temporarily supported while the shear ram was retracted, provided with thick steel plate shims to offset a large proportion of the applied displacement, and reinstalled to continue shear loading and deformation.

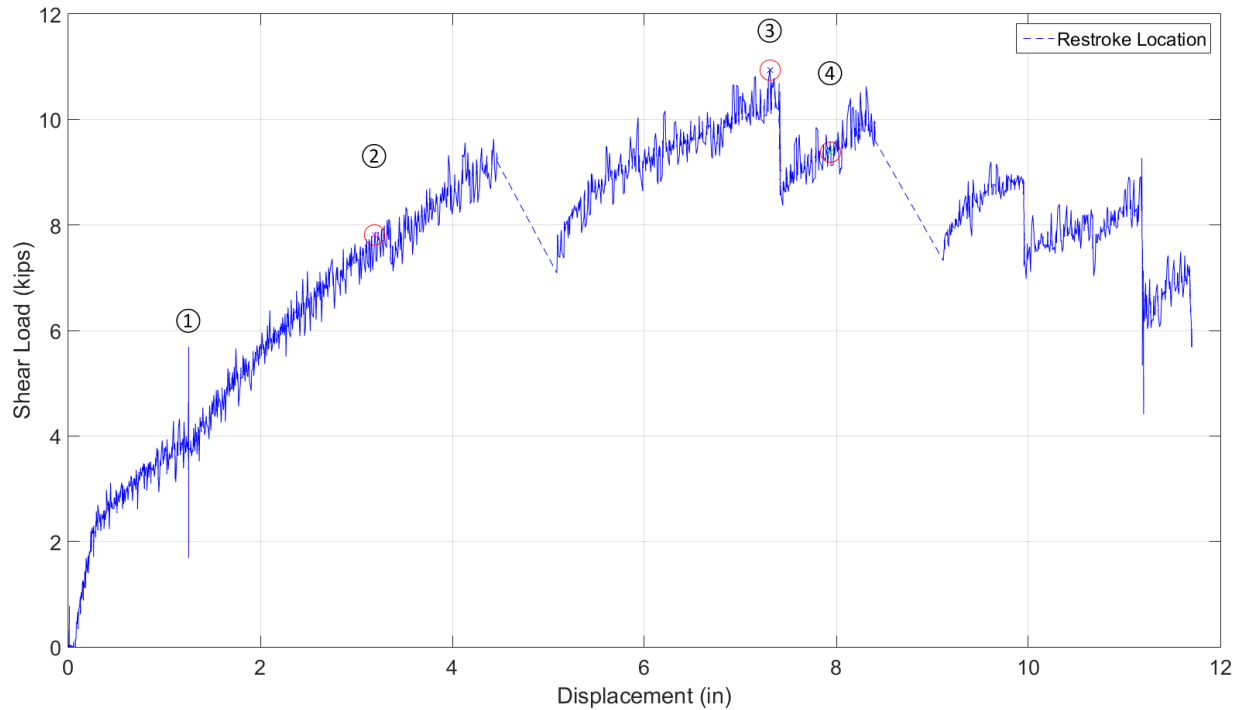


Figure 5.31 Non-deteriorated pile bent shear vs. displacement

5.7 Pile Bent Case: Deteriorated

The deteriorated pile bent test setup is shown in figure 5.32. This specimen demonstrated an abrupt global bifurcation mechanism. Local buckling in the web of the deteriorated section preceded a global buckling of the cross section at the deteriorated location, as shown in figure 5.33. The pile experienced weak axis buckling at the upper flange WT element and the web bar element, and shearing with plastic weak axis flexure at the ends of the bottom flange WT.



Figure 5.32 Deteriorated pile bent test



Figure 5.33 Deteriorated pile bent deteriorated section global section failure

The deteriorated section shortened by 0.5 inches in the top flange and the web buckled out approximately 0.875 inches. Overall, the pile displaced in the shear direction 5.5 inches, 4.4 inches of which occurred during the bifurcation failure, as shown in figure 5.34.

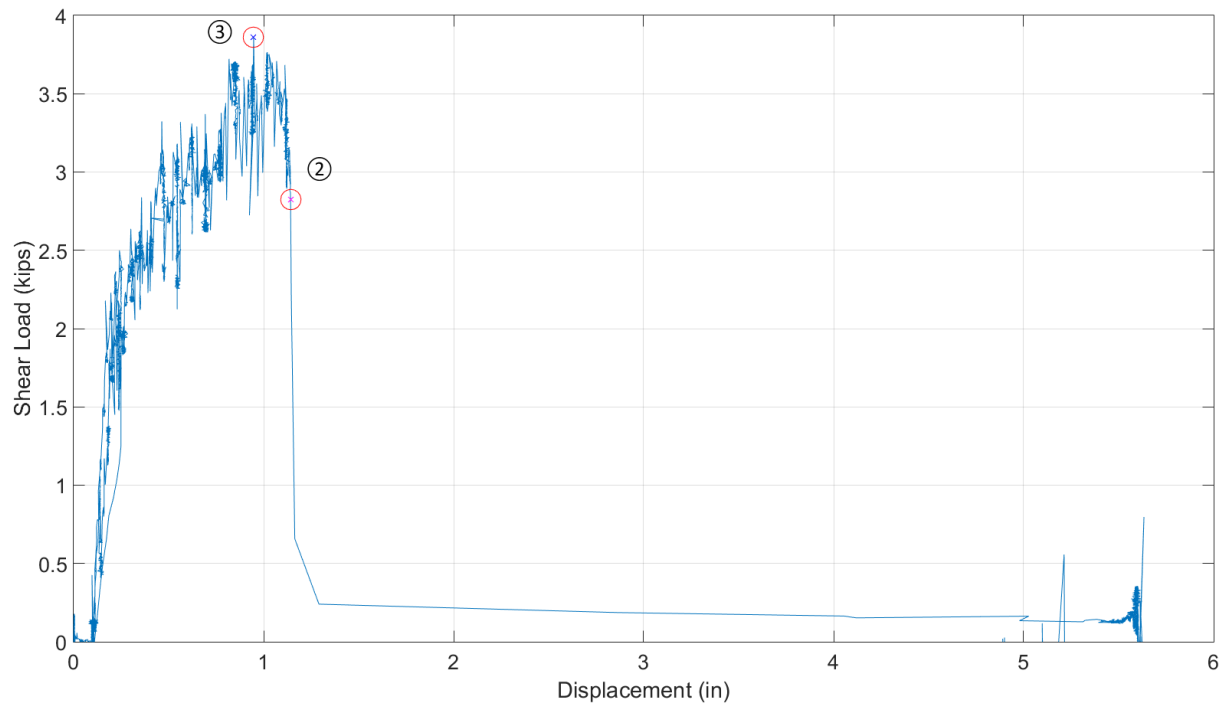


Figure 5.34 Deteriorated pile bent shear vs. displacement

Residual post-buckling strength was negligible, as shown by the reduced shear in figure 5.34 and the reduced combined axial and moment loads at the base section, reflected by the reduced strains in figure 5.35. Similar to the deteriorated abutment case, this specimen possessed greater strength than anticipated and exceeded the 45% H1-1 Strong Axis envelope of figure 5.36 by nearly 100 kips (approximately 50% greater than anticipated) in compression. Strains at the deteriorated section are shown for the entire test in figure 5.37, and in greater detail for the pre-buckling response in figure 5.38. Yielding did not occur until global buckling. The strains developed at the deteriorated section did not match preliminary analyses, which anticipated that greater strains would develop at flange element than the web element. The recorded data suggests that compression stresses were similar for the top flange and web elements.

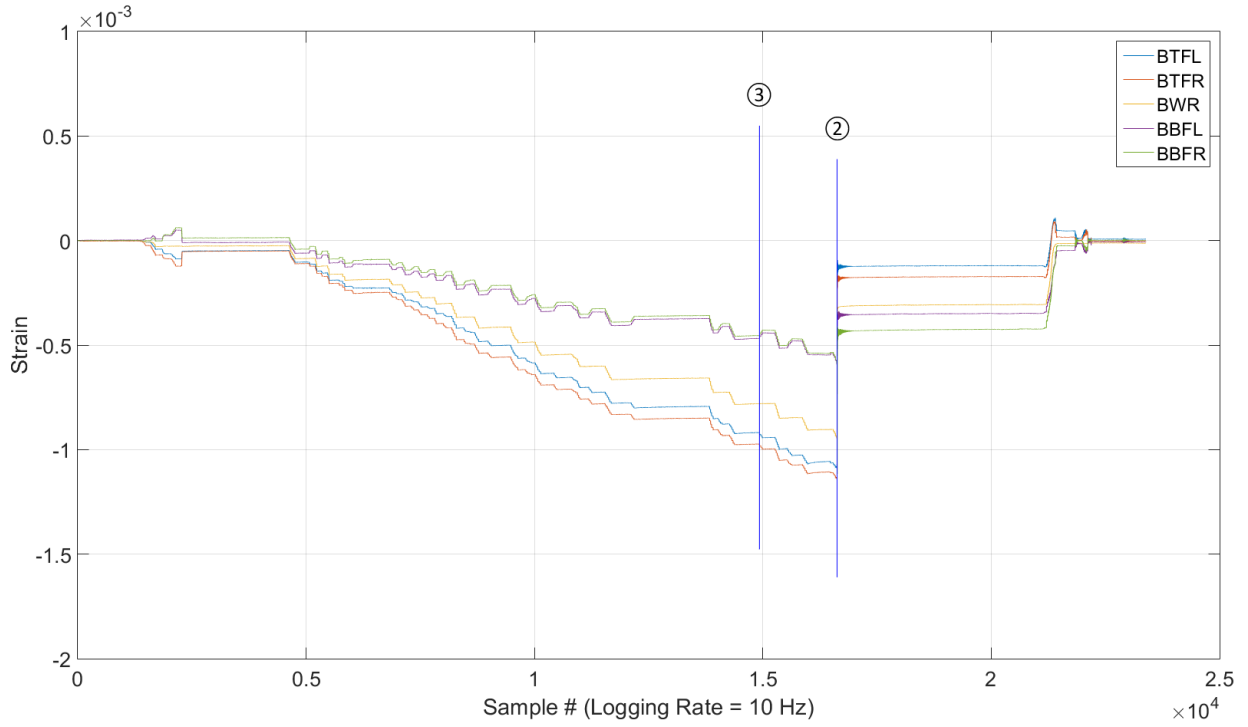


Figure 5.35 Deteriorated pile bent base section strain vs. sample

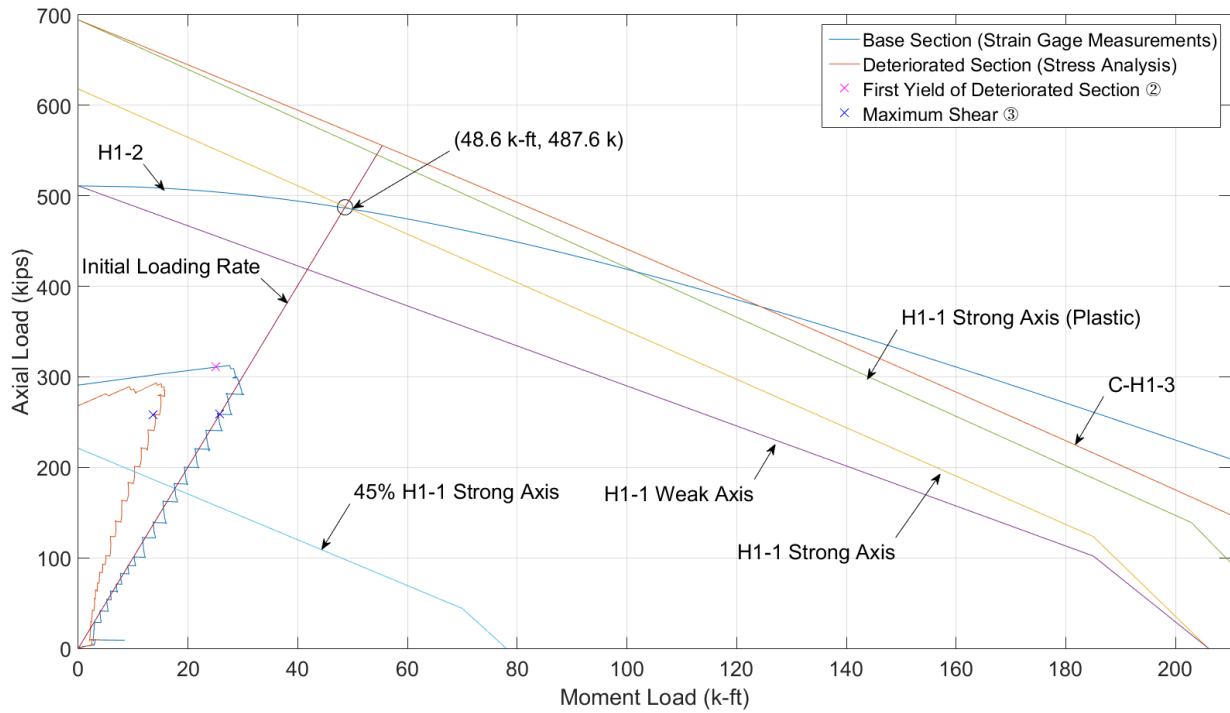


Figure 5.36 Deteriorated pile bent axial vs. moment

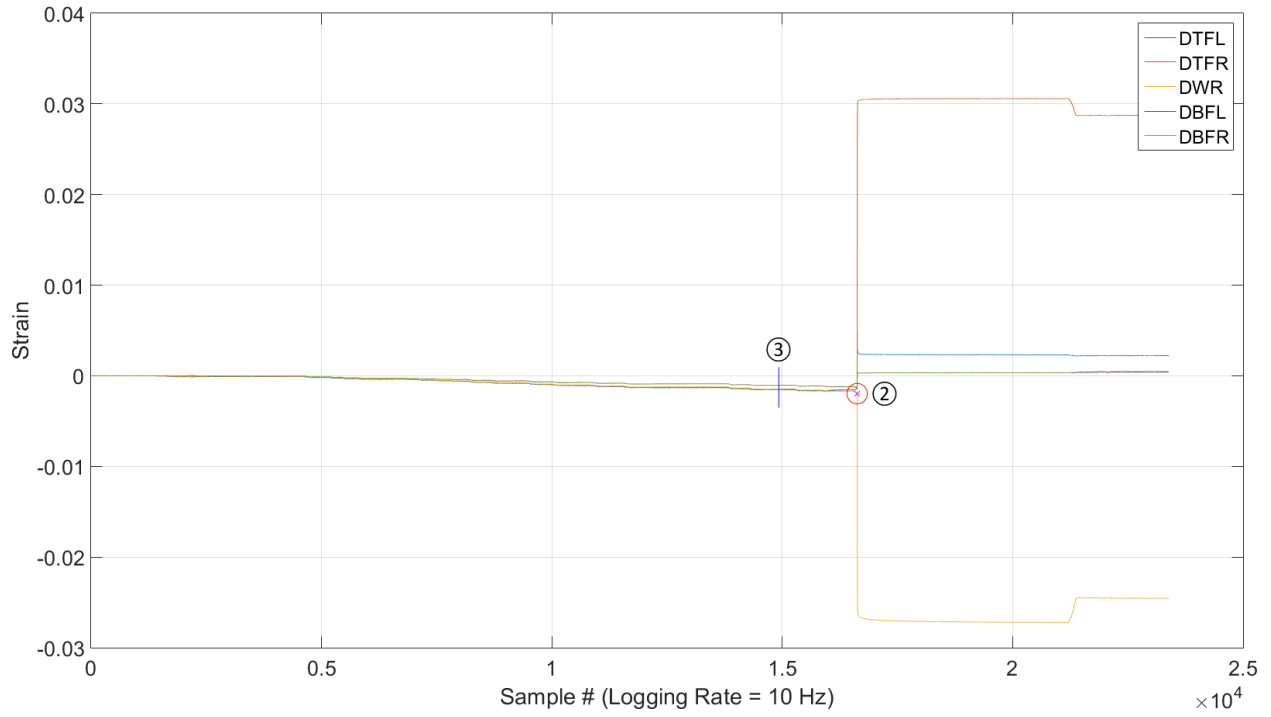


Figure 5.37 Deteriorated pile bent deteriorated section strain vs. sample

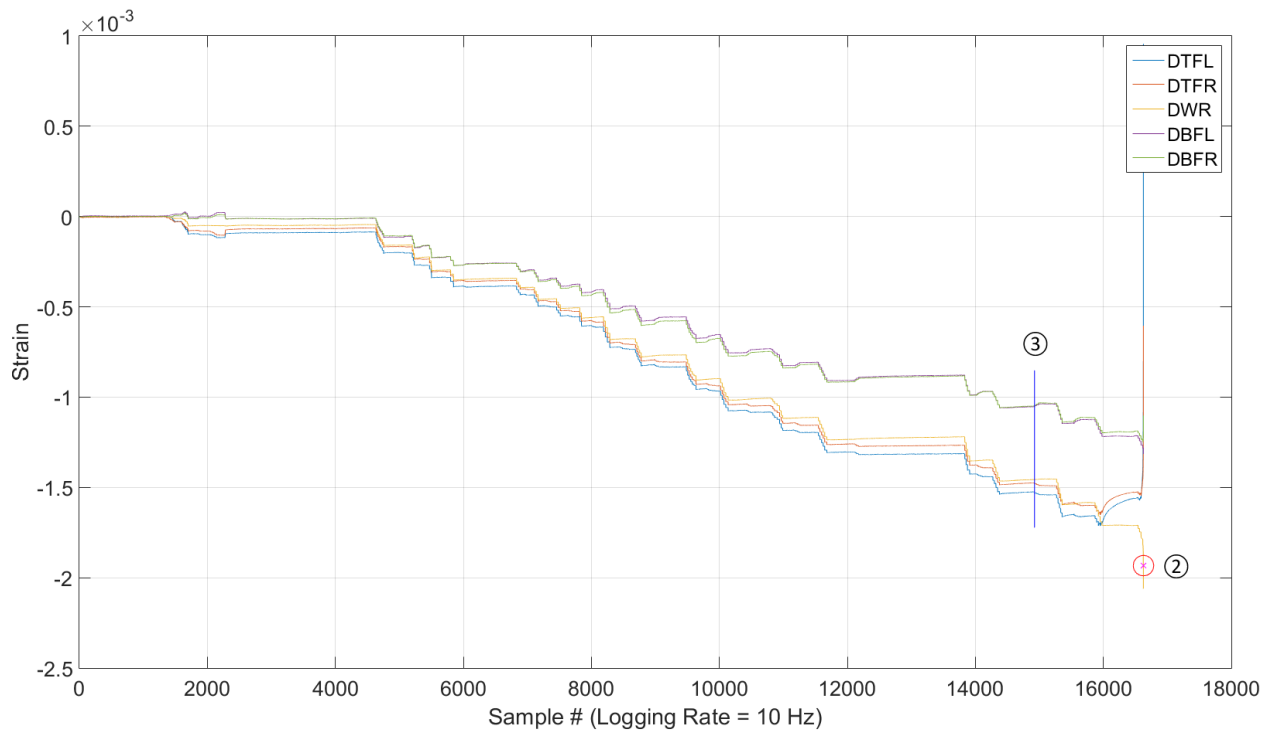


Figure 5.38 Deteriorated pile bent deteriorated section strain vs. sample zoomed in

5.8 Pile Bent Case: Retrofitted

The retrofitted bent specimen setup is shown in figure 5.39. Similar to the retrofitted abutment case, the pile reached a first limit with local buckling at the base. The stiffness of the abutment prevented the bifurcation mechanism observed for the deteriorated specimen. After the development of top flange local buckling, the pile transitioned to a secondary LTB mechanism similar to that observed for the non-deteriorated specimen. The LTB was influenced by the retrofit stiffness, which diminished the lateral buckling aspect while leaving the torsional buckling aspect largely unaffected. Consequently, the observed ultimate mechanism appeared to be primarily torsional with minimal lateral instability. The deformed pile specimen at ultimate is shown in figure 5.40.



Figure 5.39 Retrofitted pile bent test

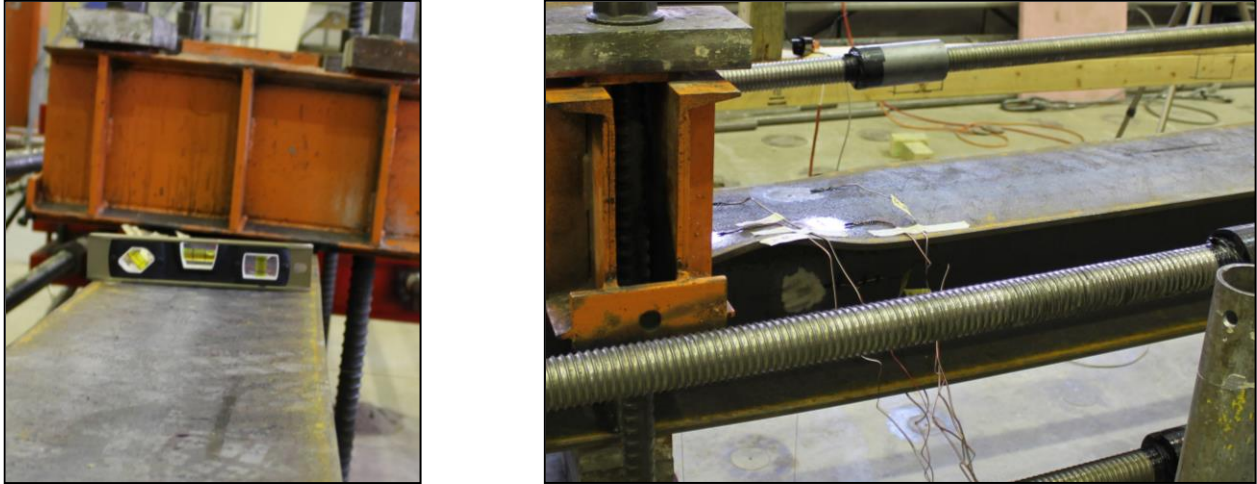


Figure 5.40 Retrofitted pile bent failure

The results from this test, similar to the abutment case, indicated that the concrete bond is substantial and the concrete drew a considerable amount of load at the retrofit location. Figure 5.41 shows that the deteriorated section carried just over 100 kips of axial force and around 10 k-ft of moment. Figure 5.42 confirms that the deteriorated section did not experience any strains near the yield limit, nor discrepancies from the sensor records outside the retrofit that would indicate buckling within the retrofit. The maximum axial load carried by the pile at the deteriorated section was 133 kips of the total 344 kips applied at that time, corresponding to a bond 3.25 times greater than the AISC (2010) recommended value. The additional stiffness due to the retrofit resulted in an inch less deflection at the maximum shear load than had been observed for the non-deteriorated specimen, as shown in figure 5.43. The maximum shear increased by 0.7 kips over the 10.9 kips carried by the non-deteriorated test. Restroking of the shear ram was required once, similarly to the non-deteriorated bent test. Yielding was recorded in the web for this test, as shown in figure 5.44, similar to the non-deteriorated bent specimen.

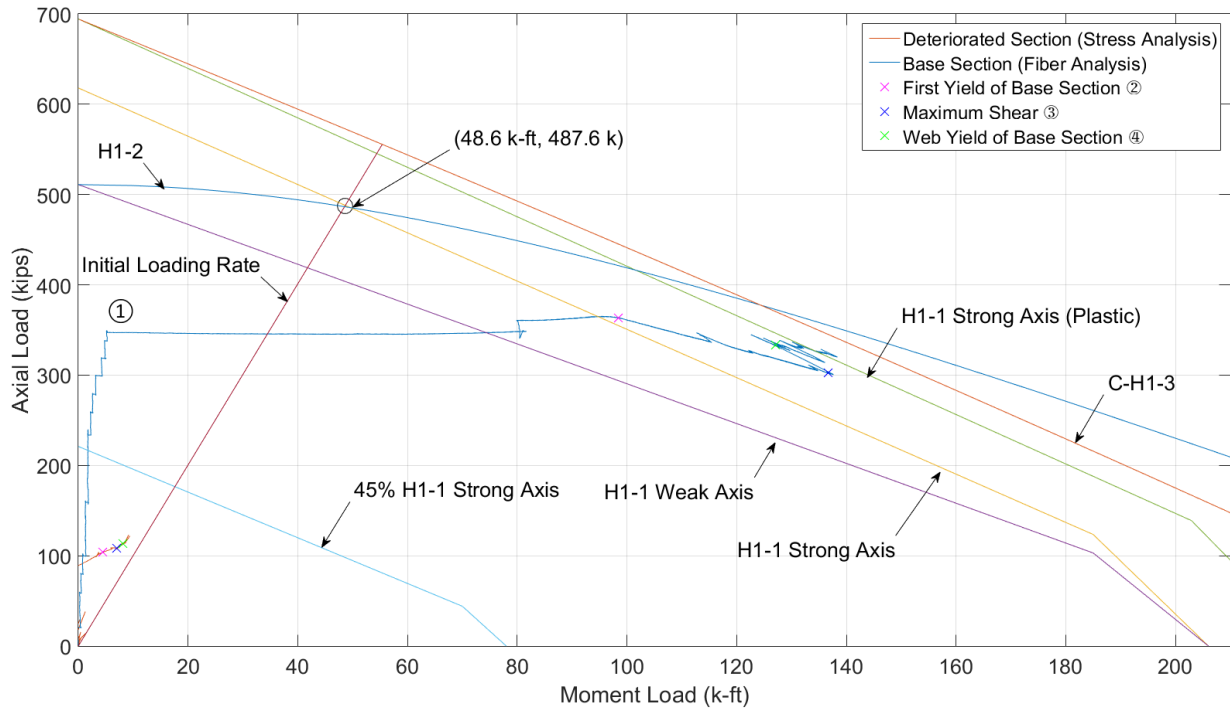


Figure 5.41 Retrofitted pile bent axial vs. moment

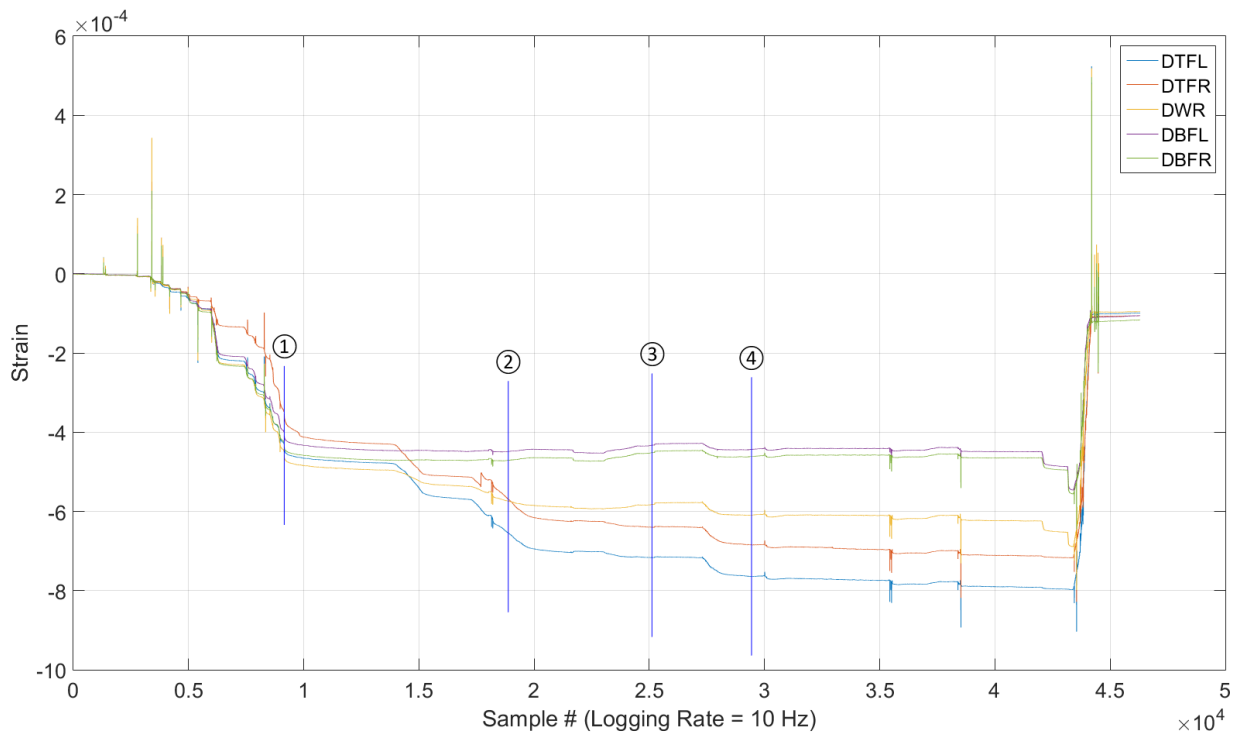


Figure 5.42 Retrofitted pile bent deteriorated section strain vs. sample

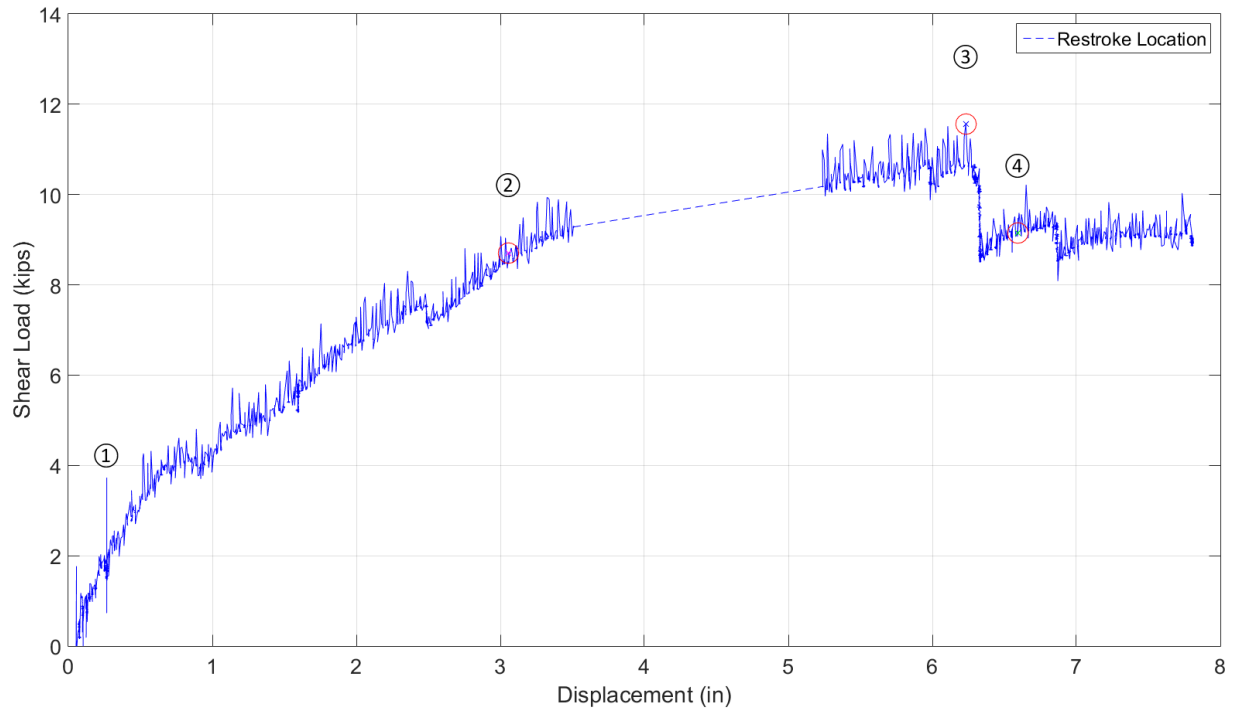


Figure 5.43 Retrofitted pile bent shear vs. displacement

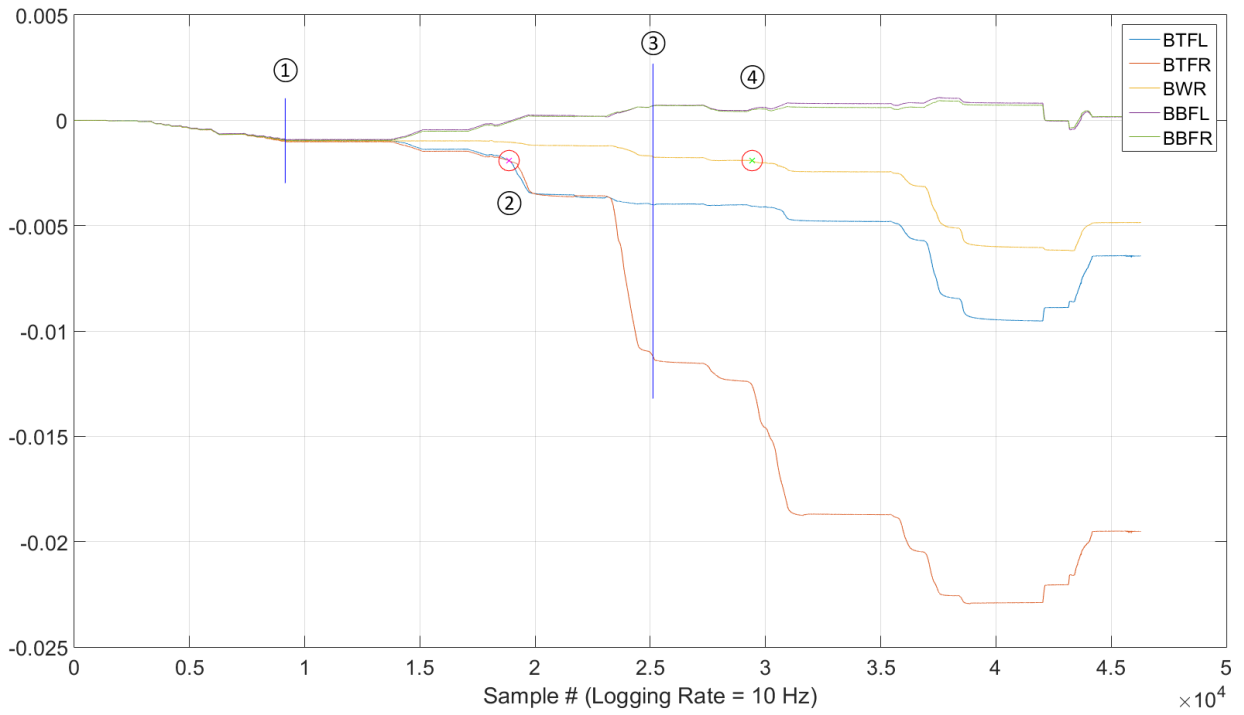


Figure 5.44 Retrofitted pile bent base section strain vs. sample

5.9 Pile Bent Case: Overview

At the base section, the results were similar for the non-deteriorated and the retrofitted tests. The initial portions of those two tests follow a different loading path (shown in fig. 5.45), but agree closely after the retrofitted case reaches combined loading state at the end of the 80/20 portion for the non-deteriorated specimen test. The discrepancy in load path was due to the concrete weight of the retrofitted pile and a loading protocol that matched the sequence of axial loads and shears (rather than base section moment) applied during the non-deteriorated specimen test. Similar to the abutment tests, the retrofitted bent specimen demands at the deteriorated section were far lower than had been observed for the non-deteriorated bent specimen at the same location, as shown in figure 5.46. This result demonstrated that composite behavior achieved through bond without mechanical connectors was far greater than anticipated based on available guidance from design specifications provided by AASHTO or AISC.

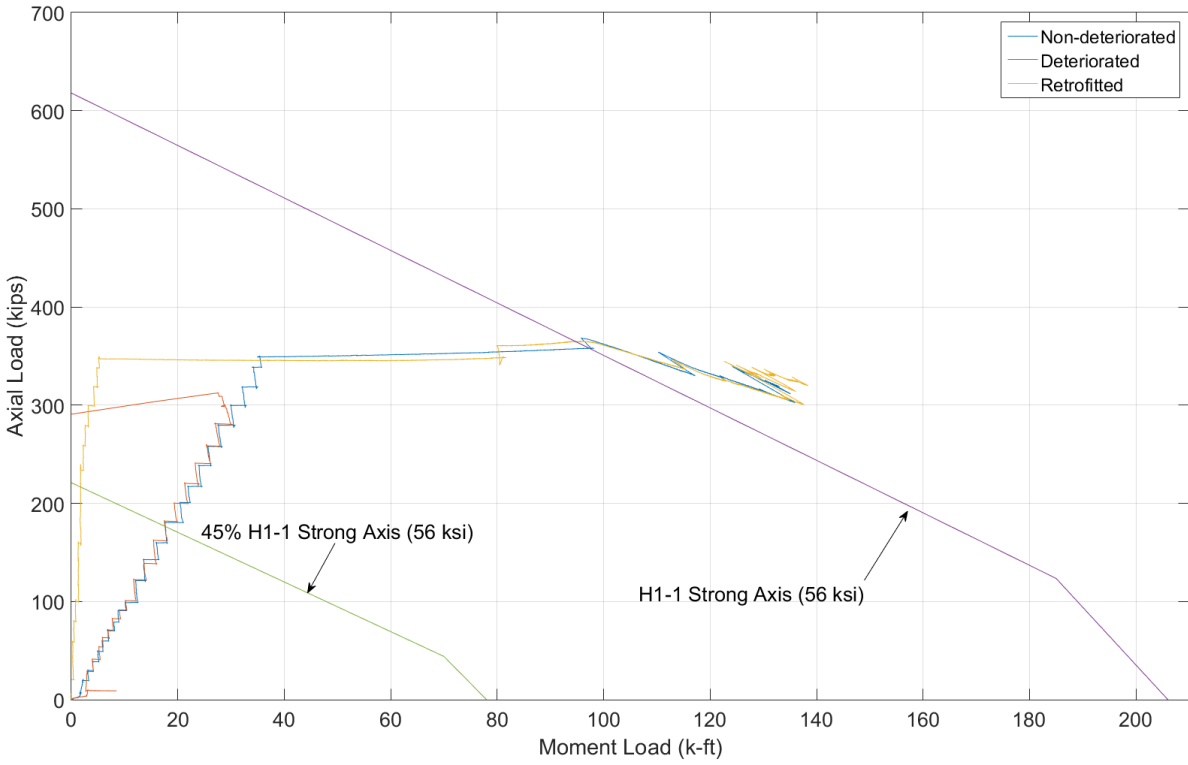


Figure 5.45 Pile bent case base section axial vs. moment

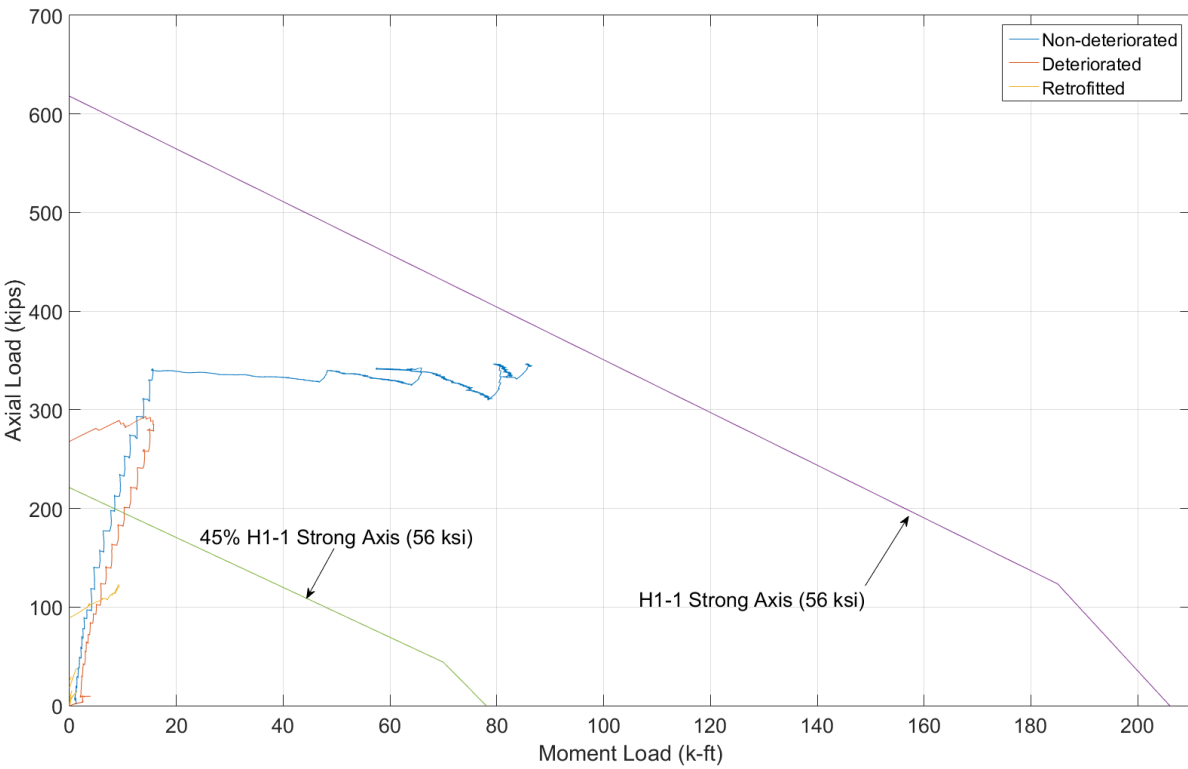


Figure 5.46 Pile bent case deteriorated section axial vs. moment

Chapter 6 Discussion and Conclusion

The experimental portion of this research demonstrated that the standard concrete encasement retrofit used by NDOR and others restores the pile to full capacity for common steel and concrete strengths, even with severe deterioration. The deterioration for this project was selected and fabricated to be a 45% loss of the steel cross-section. The retrofit restored the limiting mechanism to inelastic compression flange local buckling and significant plastification of the compression region under combined axial load and moment, localized near the “fixity” location for the experimental setup, for the abutment case. Similarly, inelasticity at the fixity location led to inelastic lateral-torsional buckling for the non-deteriorated bent case, but the retrofitted bent was significantly stiffened against the lateral component of the buckling mechanism by the retrofit, and the ultimate buckling limit for the bent case demonstrated predominantly torsional buckling. Regardless, significant plasticity was achieved by both the non-deteriorated and retrofitted bent specimens.

The retrofits clearly precluded the failure mechanisms that were observed during the deteriorated specimen tests. Additionally, a key finding from the tests is that the bond strength is far from negligible, as had been assumed during the experiment design phase based on guidance produced by AASHTO and AISC. An anecdotal discovery in NCHRP (1998) emerged after the experiments had been designed and carried out when a literature review was being performed for a separate project related to diagnostic bridge field testing. The NCHRP report recommended that a bond strength of 100 psi in shear could be assumed for steel girder flanges embedded in concrete. The report also states that this is intended to be a conservative estimate, and that bond strengths up to 145 psi have been observed. These statements are consistent with recorded data

from the experiments, which indicated that a remarkably small fraction (approximately 1/3) of the applied axial load was being carried in the steel at the deteriorated section.

The NDOR retrofit method investigated in this study demonstrated far greater capacity than required, easily restoring severely deteriorated piles to original capacity. The findings indicate that NDOR can continue implementing this method, which allows them to take advantage of the simplicity of installation, the availability and cost-effectiveness of materials, and the familiarity of work crews with concrete construction, all of which offer benefits unavailable with more recent methods like FRP wraps. The findings also suggest that there is potential for the retrofit dimensions to be significantly reduced and still achieve the required capacity restoration. Although bond is difficult to verify in-situ, minor adjustments to provide a slight degree of reliable composite action may justify simpler repairs in the future. Additional studies that may be beneficial to NDOR would address: the quantification and reliability of the concrete to steel bond accounting for the influence of environmental variation (temperature variation and cycles, moisture intrusion, and freeze/thaw); investigate force transfer from the doweled rebar and effect of drilled holes (if any); determine the effects of lower material strengths (particularly concrete); and compare costs, implementation, and effectiveness for a FRP wrap.

References

- Ainge, Steven W. (2012) "Repair and Strengthening of Bridge Substructures" Master's Theses (2009 -). Paper 173. http://epublications.marquette.edu/theses_open/173
- American Association of State Highway and Transportation Officials. (2012). *AASHTO LRFD Bridge Design Specifications, customary U.S. units.*
- American Institute of Steel Construction. (2010). *Manual of Steel Construction.*
- The Castle Group. (2014). CASTLE "Hydro-Brace" Steel H-Pile Repair System. Retrieved from <http://wjcastlegroup.com/hydro-brace/>.
- Construction Techniques, Inc. (2014). Fabriform Ballistic Pile Jackets. Retrieved from <http://www.fabriform1.com/pile-jackets.html>.
- Delaware Department of Transportation. (2012). *Bridge Manual.*
- Florida Department of Transportation, Office of Maintenance. (2011) *Bridge Maintenance and Repair Handbook.*
- Georgia Department of Transportation, Office of Bridge and Structural Design Bridge Maintenance Unit. (2012). *Bridge Structure Maintenance and Rehabilitation Repair Manual.*
- Liu, Xiangdong. (2003). Rehabilitation of steel bridge members with FRP composite materials.
- National Cooperative Highway Research Program, A.G.Lichtenstein and Associates. (1998). *Manual for bridge rating through load testing.* Washington, D.C.: Transportation Research Board, National Research Council.
- Nebraska Department of Roads, Bridge Division. (2014). *Bridge Office Policies and Procedures.*
- QuakeWrap Australia - Bridge Piles. (n.d.). Retrieved January 19, 2016, from <http://quakewrap.com.au/pilemedic/bridge-piles/>
- Shama, Ayman A. Multidisciplinary Center for Earthquake Engineering Research (U.S.). (2001). *Experimental investigation and retrofit of steel pile foundations and pile bents under cyclic lateral loading.* Buffalo, N.Y.: Multidisciplinary Center for Earthquake Engineering Research.
- Shi, C. (2014). Numerical investigation of H-shaped short steel piles with localized severe corrosion. *Engineering Structures*, 73, 114-124.
- United States, Department of the Army. (1991). *Pile construction.* Washington, DC: Headquarters, Dept. of the Army.

U.S. Department of Transportation, Federal Highway Administration. (2013). *National Bridge Inventory*.

Vijay, P.V., Clarkson, J. D., GangaRao, H. V., Soti, P. R., & Lampo, R. (2014). *FRP Composites for Rehabilitation of Hydraulic Structures*. Department of Civil and Environmental Engineering and Constructed Facilities Center, West Virginia University, and US Army Corps of Engineers.

Wan Baolin, Wisconsin Department of Transportation, Research Coordination Unit, Wisconsin Highway Research Program, Marquette University, Department of Civil, Construction and Environmental Engineering. (2013). *Procedures, cost and effectiveness for deteriorated bridge substructure repair*. Madison, WI: Wisconsin Highway Research Program.

Wipf, T. J., Iowa Highway Division, Iowa Highway Research Board, Iowa State University, Department of Civil & Construction Engineering. (2003). *Evaluation of appropriate maintenance, repair and rehabilitation methods for Iowa bridges*. Ames, Iowa: Dept. of Civil & Construction Engineering, Iowa State University.

Appendix A

A major component of the experimental design was determining the loading that the piles would be subjected to during the test. Bridges are unique, and the loading placed on them is dependent upon their geometry, material, and location. The determination of loading could (1) follow a set bridge, (2) be based on typical stresses, or (3) be a percentage of the cross section that is carrying one form of load while the rest is carrying another form. Through discussions with NDOR, the authors decided to use the third option and have 80% of the cross section carry the axial load and 20% of the section carry the moment. In the interest of being thorough, the remainder of this section will explain the other two loading scenarios that were developed in addition to the 80/20 loading rate.

One of the loading rates was based on the U.S. Department of Transportation, Federal Highway Administration's National Bridge Inventory (NBI, 2013) data for Nebraska. The NBI (2013) data was filtered to show bridges with a length less than 160 feet and greater than 20 feet. From discussions with senior faculty, most bridges of interest to this project were likely to be less than 160 feet long. Nebraska is known to have a large amount of box culverts, therefore, bridges less than 20 feet long were considered as such. After this range was extracted from the database other details of these bridges were examined. The number of spans, maximum span length, and bridge width were also compared. The worst case bridge scenario was determined by using the data based on these key points. As can be seen in table A.1, on average, majority of Nebraska's bridges are two lane bridges built around 1979.

Table A.1 Nebraska bridge data summary (NBI, 2013)

	Average	Maximum	Minimum	Std. Dev.
Width (ft)	14	70	10	6
Length (ft)	53	160	20	29
Spans	3	10	1	1
Max span (ft)	22	90	5	11
Year built	1979	2012	1914	20
Traffic Lanes	2	12	1	1

For the worst case bridge scenario, the maximum width, length, and span were used. The average number of spans was used to meet the length and maximum span selected. The remaining geometry of the bridge was determined by assuming typical bridge deck thickness and unit weight. With the geometry established, the dead load of the deck could be calculated. The NBI (2013) data for Nebraska shows that 92% of bridges are constructed with either steel or concrete girders, both of which were considered when calculating the total dead load. The remaining loads considered were thermal expansion/contraction and live load.

After all of the loads were determined, a generalized spreadsheet was developed to allow for variation in the number of girders and piles. Assumed girder sizes were used and pile spacing was limited to 10 feet. With a few iterations of these parameters, the expected loading was anywhere from 100 kips to 180 kips of dead load per pile. The largest thermal displacement was expected to be just over 0.5 inches and would likely cause about 15 k-ft in moment. The live load was applied subsequent to the thermal load. Based on AASHTO (2012) guidance, the live load (braking force included) was taken as a lower bound slope of 3.75 k-ft per kip. As another option, the live load was considered without the thermal load and braking forces. This resulted in a fairly large area, shown as the grey area in figure A.1, along the pile's interaction curve from which to choose the targeted loading.

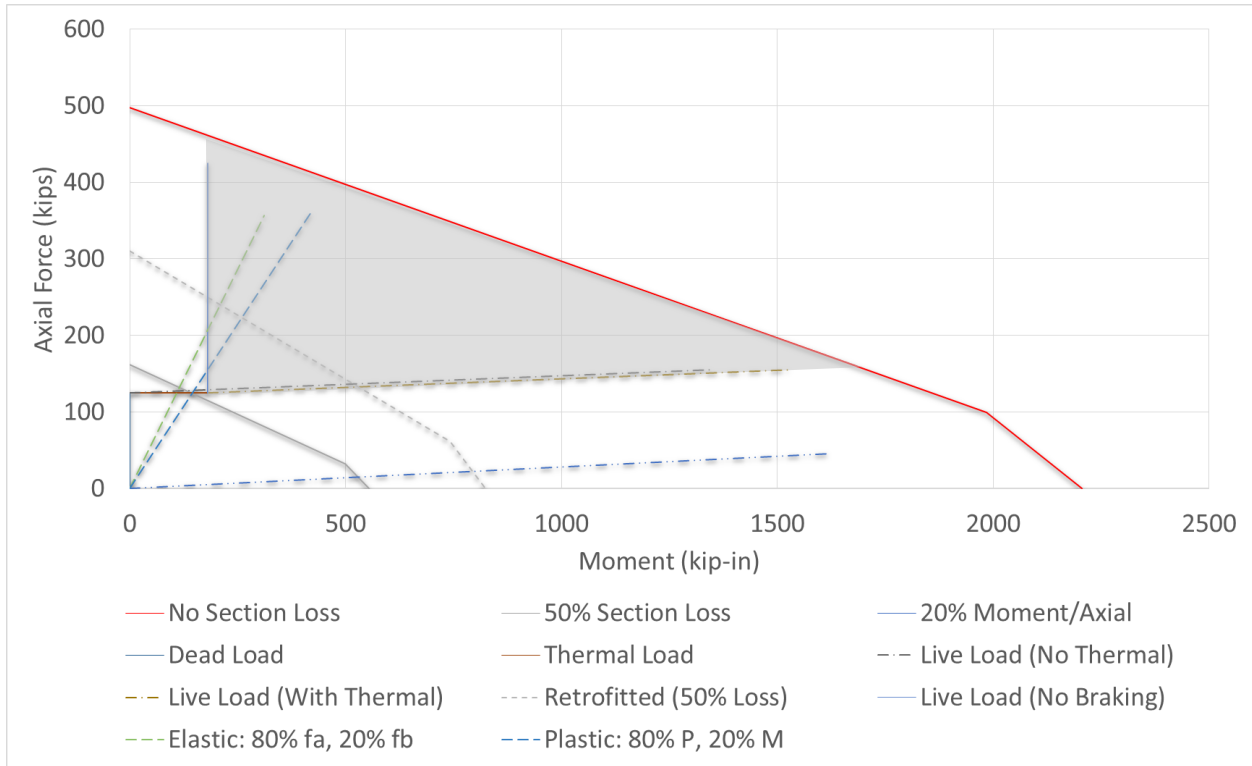


Figure A.1 Potential loading scenarios and ultimate combined load targets

The second loading scenario was based on the yield stress of the section being split 20% moment and 80% axial. This resulted in a moment that was slightly less than the 80/20 calculations based on area, but it yielded the same axial force. This becomes apparent when the axial force equation simplifies to the same equation for both cases

80/20 based on stress

$$Moment = 20\% * f_y * \frac{I_x}{d/2}$$

$$Axial Force = 80\% * f_y * A_g$$

80/20 based on area

$$\text{Moment} = f_y * t_m * b_f * (d - t_m)$$

$$t_m = \frac{A_g * 20\%}{b_f * 2}$$

$$\text{Axial Force} = f_y * (A_g - t_m * b_f * 2) = f_y * 80\% * A_g$$

As was previously stated, the loading was based on the area being divided to handle 80% axial force and 20% moment. This loading rate was within the range given by the NBI (2013) data and closer to a middle ground compared to the stress-based 80/20 loading scenario.